2018

Computational Study of Gas Separation Using Reverse Osmosis Membranes

Mohammed Faraj Alrehili
Lehigh University

Recommended Citation

Alrehili, Mohammed Faraj, "Computational Study of Gas Separation Using Reverse Osmosis Membranes" (2018). *Theses and Dissertations*. 2980.
https://preserve.lehigh.edu/etd/2980

Computational Study of Gas Separation Using Reverse Osmosis Membranes

by

Mohammed Alrehili

Presented to the Graduate and Research Committee
of Lehigh University
in Candidacy for the Degree of
Doctor of Philosophy

in

Mechanical Engineering

Lehigh University

January 2018

Approved and recommended for acceptance as a dissertation in partial fulfillment of the requirements for the degree of Doctor of Philosophy.

Date

Dr. Alparslan Oztekin
Committee Chair

Approved Date

Dr. Jacob Kazakia
Committee Member

Dr. Edmund Webb
Committee Member

Dr. Xuanhong Cheng
Committee Member

ACKNOWLEDGMENT

I would like to express my deep gratitude to my dissertation advisor, Professor Oztekin, for his advices and encouragement throughout my research. I would like to express my thanks to the committee members Dr. Edmund Webb, Dr. Jacob Kazakia and Dr. Xuanhong Cheng for serving in my PhD committee.

I would like to thank my colleague Mustafa Usta for his valuable information in this research field.

Also, I would like to express my sincere appreciation to my mother Aziza Alrehili for her emotional support, and I dedicate this dissertation to the loving memory of my father, Faraj Alrehili, who left us inspiring memories.

I would like to express my worm thanks and appreciation to my wife, Rana Alrehili, for her endless love and support and for helping me throughout my academic life, and for my beloved daughter, Joanna, who was always a source of unending joy.

I would like to thank my sponsor Tabuk University for providing the financial support to pursue my PhD degree.

CONTENTS

LIST OF TABLES

LIST OF FIGURE

Nomenclature

A_m	surface area [m^2]	Δp	pressure difference [Pa]
A	permeance [$mol/m^2 \cdot s \cdot Pa$]	Re	Reynolds number [-]
$\ddot{A}$	permeability [$mol/m \cdot s \cdot Pa$]	S	spacing [m]
C	concentration [mol/m^3]	Sc	Schmidt number [-]
C_0	inlet concentration [kg/m^3]	Sc_t	turbulent Schmidt number [-]
C_b	bulk concentration [kg/m^3]	Sh	Sherwood number [-]
C_p	production concentration [kg/m^3]	S	strain tensor *[1/s]*
C_w	membrane salt concentration [kg/m^3]	t	time [s]
C_D	drag coefficient	U_{inlet}	average velocity [m/s]
d	hydraulic diameter [m]	V_w	suction rate [m/s]
D	diffusion coefficient [m^2/s]	α	mass selectivity [-]
D_t	eddy diffusion coefficient [m^2/s]	Ω	rotation tensor [*1/s*]
fr	average friction factor	$\beta^*, \beta 1, \beta$	turbulent model parameters [-]
fr_i	friction factor in an inline geometry	γ	rate of strain tensor
fr_s	friction factor in a staggered geometry	θ	angle [$degree$]
F_1, F_2	blending functions	ω	specific dissipation rate [$1/s$]
h	height [m]	μ	dynamic viscosity [$kg/m \cdot s$]
h_m	mass transfer coefficient [m/s]	μ_t	eddy viscosity [$kg/m \cdot s$]
J	molar flux [mol/m^2]	ν	kinematic viscosity [m^2/s]
K	turbulent kinetic energy [J/kg]	ν_t	eddy kinematic viscosity [m^2/s]
l	membrane thickness [m]	ρ	density [kg/m^3]
L	computational domain length [m]	σ, λ	turbulent model parameters [-]
m	mass flux [$kg/m^2 \cdot s$]	τ	shear stress [Pa]
M	molecular weight [g/mol]	$\Delta\pi$	osmotic pressure [Pa]
$\dot{m}$	mass flow rate [kg/$m^2 \cdot s$]	κ	osmotic coefficient [kPa m^3/kg]
N	mole fraction [-]	f_x	drag force [N]
N_m	bulk mole fraction [-]	v_w	water flux [m/s]
p	pressure [Pa]	COP	coefficient of performance

Δp_L	pressure drop $[Pa]$

Subscripts and Superscripts

a and b	species: CO_2 or CH_4	w	properties at the membrane surface
i and j	index notation	t	eddy properties
CH_4	properties of CH_4	CO_2	properties of CO_2
tot	total properties	a/b	ratio of properties of a to properties of b

Abstract

Hollow fiber (HFM) and spiral wound membrane modules are among the most common separation devices employed in reverse osmosis gas separation and desalination applications. Three-dimensional steady state computational fluid dynamics (CFD) simulations are carried out to study flow past hollow fiber membrane banks (HFMB). This work focuses on enhancing the membrane performance by improving the momentum mixing in the feed channel by placing hollow fiber membranes in different arrangements and spacings. The current study investigates the effects of flow behavior on membrane performance during binary mixture separations. Carbon dioxide ($\mathrm{CO_2}$) removal from methane ($\mathrm{CH_4}$) is examined in the staggered and inline arrangement of HFMs. The most common HFM module arrangement in industrial applications is the axial flow configuration. However, this work focuses on the radial crossflow configuration. Membrane surface is treated as a functional boundary where the suction rate and concentration of each species are coupled and are functions of the local partial pressures, the permeability, and the selectivity of the membrane. The CFD simulations employed the turbulent k-ω Shear Stress Transport (k-ω SST) model to study membrane performance for a wide range of the Reynolds number. The efficiency of the inline and staggered arrangements in the separation module is evaluated by the coefficient of performance and the rate of mass flow per unit area of CO_2 passing across the membrane surface. This work demonstrates that the module with staggered arrangements outperforms the module with inline arrangements.

This study also considers a three-dimensional hybrid separation module consisting of two parallel spiral wound membranes bounding the feed channel that contains hollow

fiber membranes with various arrangements. The results of numerical simulations indicate that the hybrid membrane system with a net hollow fiber membrane provides profoundly improved membrane flux performances for both spiral wound membranes and HFMs. The removal of CO_2 from CH_4 is enhanced by the presence of net hollow fiber membranes in the feed channel.

This work also numerically characterizes flux performance of the membrane, concentration polarization, and potential fouling sites in the reverse osmosis desalination module, which contains hollow fiber membranes arranged in an inline and a staggered configuration. An accurate membrane flux model, the solution-diffusion model, is employed. Hollow fiber membrane surface is treated as a functional boundary where the rate of water permeation is coupled with local concentration along the membrane surface. The rate of water permeation increases and concentration polarization decreases as the feed flow rate is increased. Hollow fiber membranes in the staggered geometry perform better than those in the inline geometry.

It is proven by the present study that gas separation and desalination modules containing hollow fiber membranes should be designed and optimized by careful consideration of their configurations.

Chapter 1: INTRODUCTION

In the last decade, the demand for energy has significantly increased and dramatically escalated the world's fuel consumption, which inevitably raises the total cost of energy production. Natural gas is a hydrocarbon gas mixture widely used as an energy source for electricity generation. Separation membranes are crucial in the purification and processing of natural gas by facilitating removal of impurities such as water, ethane, propane, butanes, pentanes, and other gasses that prevent crude natural gas from meeting market specifications. Additionally, many of the deleterious gas impurities present in crude natural gas cause pipe corrosion and ultimately infrastructure failure [1]. In order to economize the purification and handling of natural gas, separation membrane efficiency and performance must be improved. Selection of membrane configuration and the resultant flow structures are essential for optimizing species separation and system reliability. Three membrane arrangements may be examined: countercurrent flow, concurrent flow, and radial crossflow [2]. The most common HFM module arrangement is the axial flow configuration, in which the flow and the axial direction of the HFM banks are parallel. The performance characteristics of the axial flow modules have been studied by our research group. However, this work focuses on the radial crossflow configuration, in which the flow is normal to the HFM axial direction, and investigates the effectiveness of this arrangement on the membrane performance.

Spiral wound membrane modules are considered one of the most common commercially available membrane modules used in desalination and gas separation processes. Several researchers considered flow past impermeable membrane surfaces in differing arrangements in spiral wound membrane modules for desalination processes.

Saeed et al. [3] studied three-dimensional laminar flows in a narrow channel with ladder spacers . In that study, the shear stress and the mass transfer coefficient were determined for various filament spacing. Mojab et al. [4] combined numerical and experimental techniques to examine unsteady laminar and turbulent flows in a spacer-filled channel. This work utilized CFD simulations, and identified four distinct flow regimes in a spacer-filled channel for values of Reynolds number between 100 and 1000. Karode and Kumar [5] studied steady three-dimensional laminar flow in a rectangular channel containing cylindrical spacers. In that work, bounding surfaces were considered impermeable, and the effectiveness of the spacers was determined in terms of the pressure drop through the channel and the average shear exerted on the top and bottom membranes. Koutsou et al. [6] introduced a novel approach for minimizing the contact area between novel 3D net-type structure spacers and the membrane surface. The aim of that work was to promote a high mass transfer rate along the membrane surface and mitigate concentration polarization on the membrane surface. Shakaib et al. [7] conducted three-dimensional flow simulations for desalination processes and proved that membrane performance is affected by momentum mixing. The authors showed that there is a significant influence of spacer geometry on wall shear stress rates and mass transfer coefficients.

Other investigators considered membrane surfaces to be permeable in desalination processes. Subramani et al. [8] used a finite element model of crossflow membrane filtration systems to study momentum and mass transport. Pressure losses, fluid flow structures, and concentration polarization phenomena were simulated in open and spacer-filled channels in two dimensions. Kaya et al. [9] utilized a CFD $k-\varepsilon$ turbulence model to investigate the effects of shear stress distribution and pressure loss on various HFM modules. Anqi et al. [10–12] studied the effect of the flow characteristics on membrane efficiency, concentration polarization, and possible fouling along the membranes in desalination processes. They studied two- and three- dimensional steady flows in a channel containing circular spacers in various configurations, and the pressure, concentration, and velocity fields were modeled using k-ω SST turbulence model. Recently, Usta et al. [13] studied desalination process in a module containing corrugated membranes and demonstrated that corrugated membranes improve membrane flux performance, and help mitigating the concentration polarization and the membrane fouling.

Several investigators, including present author, [10,12,14–18] have studied velocity and concentration field in the feed channel to characterize membrane performance in spiral wound membrane modules. Shakaib et al. [16] conducted three-dimensional flow simulations in a feed channel that contains spacers. They reported that the membrane performance is influenced by momentum mixing in the feed channel bounded by the impermeable walls. Geraldes et al. [17] have numerically studied velocity and concentration field in a feed channel of a reverse osmosis (RO) desalination module. The water flux through the membrane was determined by implementing pre-determined permeate velocity along the membrane surface. Geraldes et al. proved that the placement of spacers closer to the membrane surface enhances membrane performance. Ma and Song [18] employed a membrane flux model that couples salt concentration and water permeate along the membrane surface in a spiral wound membrane module. Ma and Song demonstrated that membrane flux performance is influenced by the arrangement of spacers.

Experimental and numerical characterization of hollow fiber membranes has been documented [19–29]. Recently, Alrehili et al. [19] characterized membrane performance in a gas separation module containing an array of hollow fiber membranes. Velocity and concentration profiles over a bank of hollow fiber membrane are calculated for various flow rates. Alrehili et al. [19] showed that the arrangement of the hollow fiber membranes in a gas separation module has profound influence on the membrane performance. Alkhamis et al. [20] studied the process of separating carbon dioxide from methane in a membrane module containing porous medium and selective membranes. Marcovecchio et al. [21] characterized concentration polarization in a hollow fiber membrane module for reverse osmosis desalination process by conducting computational fluid dynamics simulations. Marcovecchio et al. concluded that the performance of the desalination using hollow fiber membranes is strongly dependent on the concentration and pressure distribution in the feed channel. Ghidossi et al. [22] examined the pressure drop and membrane characteristics for various operating conditions in a hollow fiber membrane module. High performance hollow fiber membranes similar to those considered in the present study have been fabricated and tested in laboratories. Sukitpaneenit and Chung [23] fabricated high performance thin-film composite forward osmosis hollow fiber membranes. They reported that the water flux increases with an increase in draw solution concentration since a larger effective osmotic pressure difference provides a greater driving force. Chou et al. [24] designed and fabricated pressure retarded osmosis hollow fiber membrane. Chou and his co-workers have built thin-film composite hollow fiber membrane with high permeability and high rejection rate.

Experimental and computational studies were conducted for modules containing a bank of hollow fiber membranes for humidification and dehumidification processes [25,26,29,30]. Huang and his co-workers [25,26] reported that the membrane performance is improved by the proposed elliptical hollow fiber membrane. Zhang et al. [29] conducted experiments to study heat and mass transfer in a module containing a bundle of hollow fiber membranes with different arrangements. They concluded that the flow inside the hollow fiber bank is turbulent and that heat and mass transfer performance of module containing hollow fibers in a staggered arrangement is better than that containing inline arrangements of fibers. An experimental study by Huang et al. [28] revealed that the staggered configurations with high packing fraction perform better heat and mass transfer. Teoh et al. [30] have conducted experimental study to investigate the effect of various hollow fiber membrane geometries on the performance of the distillation process. Teoh et al. documented that the module with twisted and braided hollow fibers design provides permeate flux that is 35% greater compared to other designs considered.

Recently, Alkhamis et al. [14,31] considered membrane surfaces to be permeable in gas separation processes. These investigators introduced a new model to determine the membrane flux conditions for a binary mixture of CO_2 and CH_4 that captured the mass transports through the membrane. Baseline Reynolds stress (k-ω BSL) and large eddy simulation (LES) turbulence models were used to simulate the flow for $Re \leq 1000$. The membrane wall was treated as functional surface, and the mass fluxes of species were calculated based on local partial pressure, selectivity, and membrane permeability. The results revealed that membrane performance improved due to momentum mixing induced by the presence of spacers in the feed channel.

Hollow fiber membrane modules are among the most common commercially available membrane modules utilized in desalination and gas separation applications. Several researchers considered flow past permeable membrane surfaces in differing arrangements in hollow fiber membrane modules for gas separation processes [2,14,19,32]. Katoh et al. [32] developed a new simulation model to predict the dynamic performance of HFM modules for gas separation processes using the relaxation method. The relaxation method is a technique used to solve the governing equations for transport across the membrane, mass balance, and pressure distributions in an HFM module. They examined flow patterns by changing various operating conditions and showed fluid mixing in the feed channel increased the performance more than mixing on the permeate side of the membrane. Alkhamis et al [20] employed Baseline Reynolds Stress (BSL Reynolds Stress) turbulence model and the Brinkman–Forchheimer equations to investigate spatial structure of the flow inside the lumen and the porous layer. The results showed that the hollow fiber membrane performance is improved due to the influence of the momentum mixing induced by the presence of orifices. Thundyil et al. [2] came up with a mathematical model of gas separation to examine which design optimizes the performance of the three flow patterns: radial crossflow, countercurrent, and concurrent HFM modules. That work showed that the radial crossflow arrangement was more effective than the concurrent and countercurrent arrangements due to the higher feed concentration distribution and notable thermal impacts influencing permeation rates.

Recently, the current author and Anqi et al., [19,33] have studied velocity and concentration field in the feed channel to characterize membrane performance in hollow fiber membrane modules. Alrehili et al. considered steady state and transient two-dimensional radial crossflows past HFMBs for varying arrangements. In that work, the membrane surface was considered permeable and the mass flux and concentration were determined as a function of the local partial pressures, the permeability, and the selectivity of the membrane. Anqi et al. [33] studied two-dimensional steady-state and transient flows in a channel containing HFMs in various configurations for desalination processes. The pressure, concentration, and velocity fields were modeled using the k-ω SST turbulence model. The results from both works elucidate that staggered geometries for HFMBs enable greater performance than inline geometries in gas separation and desalination processes.

Several researchers developed a mathematical model to investigate the effects of concentration polarization in gas separation hollow fiber modules [34,35]. Concentration polarization phenomena occur when the membrane enables only CO_2 molecules to pass through while CH_4 molecules are rejected. The rejection of CH_4 from membrane causes an accumulation of CH_4 near the membrane surface. Such phenomena are referred as concentration polarization occurring at the surface or near the surface of the membrane. Mourgues and Sanchez [34] studied the influence of concentration polarization in gas separation processes for co- and counter-current configurations. The impacts of concentration polarization were analyzed based on the permeation flux, selectivity, pressure of operation, and feed velocity. That work demonstrated the necessity of considering concentration polarization effects in a binary gaseous mixture separation for process analysis and apparatus design. Behling et al. [35] studied the effects of concentration polarization in gas separation both theoretically and experimentally and also concluded concentration polarization effects must be considered to accurately assess membrane performance. The authors showed that higher flow rates in the feed channel decrease the concentration polarization.

The present work considers three-dimensional HFM modules that facilitate gas separation to probe the effects of physically relevant three-dimensional geometries on membrane performance. In this study, we investigate the spatial characteristics of radial crossflows around HFM modules to show that membrane performance is enhanced due to momentum mixing in the flow domain. CFD simulations utilizing the k-ω SST turbulence model for steady state three-dimensional flows are performed for a binary mixture containing CO_2 and CH_4 to characterize the velocity and concentration fields. Membrane performance is determined for varying Reynolds number from 200 to 1000, and for varying arrangements of hollow fibers as a staggered or an inline and for varying spacing of periodically placed hollow fibers in the feed channel.

The present study is the first to consider a hybrid module of spiral wound and HFM membranes. Steady state flow simulations are conducted in a three-dimensional channel that is bounded by two parallel spiral wound membranes and that contains hollow fiber membranes. Different arrangement and spacing of HFMs in the hybrid module are simulated for different flow rates. The primary flow is parallel to the spiral wound membranes and perpendicular to the hollow fiber membrane axes. Membrane performance is determined for modules containing the hollow fiber array with the inline, staggered, and net arrangements.

In addition, the present work examines the velocity and concentration fields to evaluate the membrane flux performance, concentration polarization characteristics of the membrane and potential fouling sites in a hollow fiber membrane desalination module for a wide range of flow rates. The solution-diffusion model is employed to determine the water permeate through membranes. The salt concentration and the permeate water flux along the membrane surface are coupled.

Chapter 2: GOVERNING EQUATION

Steady-state three-dimensional simulations for HFMBs comprised of circular cross-sectioned HFMs are conducted for the Reynolds number $(Re) \leq 1000$ for both inline and staggered geometries. The binary mixture of $\mathrm{CH_4}$ and $\mathrm{CO_2}$ is considered to be isothermal and incompressible. The fluid is assumed to have constant physical properties such as, density, ρ, dynamic viscosity, μ, and the mass diffusion coefficient, D. The velocity and concentration fields in the flow domain are given by the conservation of mass, conservation of momentum, and mass transport equations of any species "a", respectively:

$$\frac{\partial u_j}{\partial x_j} = 0 \tag{1}$$

$$\frac{\partial u_i}{\partial t} + u_j \frac{\partial u_i}{\partial x_j} = -\frac{1}{\rho}\frac{\partial p}{\partial x_i} + \frac{1}{\rho}\frac{\partial}{\partial x_j}\left(\mu \frac{\partial u_i}{\partial x_j}\right) \tag{2}$$

$$\frac{\partial N_a}{\partial t} + u_j \frac{\partial N_a}{\partial x_j} = \frac{\partial}{\partial x_j}\left(D \frac{\partial N_a}{\partial x_j}\right) \tag{3}$$

The subscript i = 1, 2, and 3, and u_1, u_2 and u_3 are the stream-wise, span-wise, and cross-flow components of velocity, respectively. x_1, x_2, and x_3 are the spatial coordinates in the stream-wise, span-wise and cross-flow directions, respectively. j is the summation index, t is time, ν is the kinematic viscosity ($\nu = \mu/\rho$), and p is the pressure. $C = C_a + C_b$ is the concentration of the binary mixture where C_a and C_b are the concentrations of species "a" and "b", respectively. $N_a = C_a/C$ is the mole fraction of any species "a".

The Shear Stress Transport (SST) k-ω turbulence model proposed by Menter [36] can be employed to characterize turbulent flow structures. The present author and other investigators [10,19,33] successfully employed the k-ω Shear Stress Transport (k-ω SST) turbulence model to characterize flows in the feed channel of a spiral wound membrane module containing spacers and HFMB for desalination and gas separation applications. It is well known that the SST k-ω turbulence model can predict turbulent flow, capture turbulent flow structures near boundaries, and elucidate flow behavior for separating flows and flows driven by pressure gradients [23,24]. The SST k-ω turbulence model is used to characterize the steady three-dimensional turbulent flow structures in the feed channel. The eddy viscosity is defined as

$$\mu_t = \rho \frac{a_1 k}{\max(a_1 \omega; \Omega F_2)} \tag{4}$$

The turbulent SST k-ω momentum transport equation may be written as:

$$\frac{\partial u_i}{\partial t} + u_j \frac{\partial u_i}{\partial x_j} = -\frac{1}{\rho}\frac{\partial p}{\partial x_i} + \frac{1}{\rho}\frac{\partial}{\partial x_j}\left((\mu + \mu_t)\frac{\partial u_i}{\partial x_j}\right) \tag{5}$$

The equations governing the turbulent kinetic energy, k, and the specific dissipation rate, ω, are:

$$\frac{\partial(\rho k)}{\partial t} + u_j \frac{\partial(\rho k)}{\partial x_j} = \tau_{ij}\frac{\partial u_i}{\partial x_j} - \beta^* \rho \omega k + \frac{\partial}{\partial x_j}\left[\left(\mu + \sigma_{k_1}\mu_t\right)\frac{\partial k}{\partial x_j}\right] \tag{6}$$

$$\frac{\partial(\rho\omega)}{\partial t} + u_j \frac{\partial(\rho\omega)}{\partial x_j} = \frac{\gamma}{\nu_t}\tau_{ij}\frac{\partial u_i}{\partial x_j} - \beta\rho\omega^2 + \frac{\partial}{\partial x_j}\left[(\mu + \sigma_\omega \mu_t)\frac{\partial \omega}{\partial x_j}\right] +$$

$$2\rho(1 - F_1)\sigma_{\omega_2}\frac{1}{\omega}\frac{\partial k}{\partial x_j}\frac{\partial \omega}{\partial x_j} \tag{7}$$

The equation governing mass transport of species "a" for turbulent flow is:

$$\frac{\partial N_a}{\partial t} + u_j \frac{\partial N_a}{\partial x_j} = \frac{\partial}{\partial x_j}\left((D + \sigma D_t)\frac{\partial N_a}{\partial x_j}\right) \tag{8}$$

where Ω is the magnitude of the vorticity, a_1, β, β^*, σ_{k_1}, σ_ω, σ_{ω_2} are closure coefficients and F_1, F_2 are blending functions. Detailed description of the turbulence parameters is provided in Ref [36]. D_t is the eddy diffusion coefficient, the turbulent Schmidt number, Sc_T, is defined as

$$Sc_t = \nu_t / D_t \tag{9}$$

where Sc_{T} and β are selected to be 0.85 and 0.09, respectively

2.1. MEMBRANE MODELING AND BOUNDARY CONDITIONS

2.1.1. GAS SEPARATION

Following the membrane flux model introduced by Alkhamis et al. and Alrehili et al. [14,19,20,31], the boundary conditions applied on the velocity and the concentration field along the surface of the HFMs are determined from first principles. The molar flux of the species "a" across the membrane per unit area extracted from the inlet flow is determined as

$$J_a = \frac{\ddot{A}_a \Delta p_a}{l} \tag{10}$$

where l is the thickness of the HFM, $\ddot{A}_a$is the molar permeability of species "a", and the partial pressure difference of species "a" through the HFM at a locations 1 and 2 not on the same side of the membrane can defined by

$$\Delta p_a = \left(p_a^{(1)} - p_a^{(2)}\right) \tag{11}$$

The total molar flux, J, per unit area across the HFM can be expressed as

$$J = J_a + J_b = A_b \Delta p_{tot} [\alpha + (1 - \alpha) N_b] \tag{12}$$

Here J_a and J_b are the molar fluxes of species of "a" and "b", respectively. $\Delta p_{tot} = \Delta p_a + \Delta p_b$ is the total pressure difference across the HFM. The HFM selectivity is defined as $\alpha = \ddot{A}_a / \ddot{A}_b = A_a / A_b$, where $A_a = \frac{\ddot{A}_a}{l}$ and $A_b = \frac{\ddot{A}_b}{l}$ are the permeability of species "a" and "b", respectively. The relationship between the total pressure and the partial pressure of a species "a", $\Delta p_a = N_a \Delta p_{tot}$. The suction rate is determined from local pressure and mole fraction. V_w may be written as:

$V_w = J/C = \frac{A_b \Delta p_{tot}}{C}[\alpha + (1-\alpha)N_b]$ (13)

The suction rate along the HFM surfaces is a function of the selectivity of the membrane, the permeability of the membrane, the total pressure drop across the membrane, and the local mass fractions of the species. At the surface of the HFM, the no slip and suction boundary conditions are applied on the velocity field. The boundary conditions at the surface of the membrane applied on the concentration field are obtained from the conservation of mass for a species "a,

$J_a = -D\frac{\partial C_a}{\partial r}$ (14)

The mass flux through membrane surface is modeled in term of the rejection rate:

$-D\frac{\partial C_a}{\partial r} = RV_w C_a$ (15)

The rejection rate can be expressed as the ability of membrane to separate the species of a binary mixture; it can be determined in term of selectivity as

$R = \alpha/(\alpha + (1-\alpha)N_b)$ (16)

The detailed derivation of the suction rate and the flux condition applied at the surface of the HFM is provided by [19,20].

The velocity and mole fraction profiles are assumed to be uniform at the inlet, and constant pressure and constant gradient boundary conditions are imposed at the outlet. Periodic boundary conditions are imposed on the longest side faces of the computational domain to model an infinitely wide HFMB region.

The module is operating at a pressure 5 MPa. The physical properties of the fluid are assumed to be constant, but are adjusted to the module pressure: the density $\rho = 50.3$ kg/m^3, the dynamic viscosity $\mu = 12.09^{-6}$ $Pa.s$, and the binary diffusion coefficient of the mixture is $3.57\text{x}10^{-7}$ m^2/s. The Schmidt number is calculated to be $Sc = \nu/D = 0.67$. The permeance of the HFM is chosen as $A_{CO_2} = 3.06\text{x}10^{-8}\ \ kg/m^2 \cdot s \cdot Pa$ and a total pressure difference across the membrane is chosen as $\Delta p_{tot} = 5\ MPa$. Spacing parameter S/d and the membrane selectivity also influences membrane performance. The membrane mass selectivity is $\alpha = A_{CH_4}/A_{CO_2} = 0.01415$ and the mole fraction of CH_4 at the inlet is selected to be 0.7.

2.1.2. DESALINATION

Several membrane flux models have been developed and used by researchers to study separation processes in membrane modules. An extensive review of these membrane flux model is reported by Malaeb and Ayoub [39]. Flux models for the reverse osmosis process are categorized into three distinct groups: irreversible thermodynamics models, porous models, and homogeneous membrane models. Irreversible thermodynamics model is one of the early membrane transport models which defines the transport with mechanical and osmotic pressure gradients. This model assumes that the membrane operates near equilibrium [40]. Phenomenological thermodynamic relationships are used to derive solution and solute flux equations [41]. A key membrane transport model was introduced by Kedem-Karchalsky [42] based on the irreversible thermodynamics principles. They proposed that the flux is a function of the trans-membrane pressure gradient as a driving force [42]. Kargol et al. used this model and mechanistic transport equations to estimate RO membrane performance successfully [43]. They have demonstrated that the irreversible thermodynamic model proposed by Kedem-Karchalsky and the mechanistic transport models are mutually equivalent. Many variations of this model have been introduced by other investigators. Models based on the porous models assume that transport through the membrane pores is carried out by the contribution of both diffusion and convection. It assumes that membrane contains straight cylindrical pores with the thickness of the membrane and a specific radius. Recently developed modified pore-flow models factoring in the contribution of Knudsen flow to vapor transport exhibit an accurate estimation of mass transport through the membrane [44]. Nonporous or homogeneous membrane models assume that solute and solvent transport occurs between the interstitial space of the polymer chains or modules, typically by diffusion [39]. This model also includes size exclusion and charge or dielectric exclusion principles in order to describe the solute separation [45]. There are several proposed approaches based on the nonporous membrane models that deal with electro-migration forces [46]. This includes the interaction between the rejection of co-ions and fixed electric charges attached to the membrane matrix. The combined model that takes into account solute diffusive and convective fluxes and fluxes induced by electric charges may provide a better estimation of the membrane flux.

The solution-diffusion flux model employed by the present study is derived from irreversible thermodynamic principles. Wijmans and Baker [47] have shown that the solution-diffusion model can capture the rate of permeation through membrane reasonably well and can be used to predict the membrane performance in a reversible osmosis process. The present study considers the Solution-Diffusion model and treats membrane as a semi-permeable functional surface where the water permeation rate and salt concentration are coupled. The boundary conditions at the membrane surface are as follows:

The local water flux through the membrane can be written as:

$$v_w = A[\Delta p - \Delta\pi] \tag{17}$$

where A is the water permeability through the membrane, Δp is the transmembrane pressure difference, and $\Delta\pi$ is the osmotic pressure.

The salt concentration gradient at the membrane surface can be determined as:

$$D\frac{\partial C}{\partial y} = v_w(C_w - C_p) \tag{18}$$

where C_w is the local salt concentration at the membrane surface, and C_p is the salt concentration in the production side. It is important to note that the membrane is assumed to be a semipermeable surface where only water permeates.

At the inlet, velocity and concentration profiles are assumed to be uniform. At the outlet, constant pressure and constant velocity gradient boundary conditions are applied. Symmetric boundary conditions are imposed on both velocity and the concentration fields at the side boundaries of the computational domain. The salt concentration at the inlet, C_0, is selected to be 4000 ppm.

The physical properties of the fluid are assumed to be constant: the density $\rho = 1000$ kg/m^3, the dynamic viscosity $\mu = 10^{-3}$ Pa s., and the diffusion coefficient of the water-salt solution $D = 1.5\times10^{-9}$ m^2/s. The Schmidt number is calculated to be $Sc = \nu/D = 667$. The transverse pressure difference across the hollow fiber membranes is $\Delta p = 1.25$ MPa and the osmotic pressure coefficient is set to $\boldsymbol{\kappa} = 75$ kPa m^3/kg. The membrane permeability is $A = 2.3\times10^{-11}$ m/(s Pa), and production side salt concentration $C_p = 0$.

2.1.3. DIMENSIONLESS PARAMETERS

The performance of the HFM module is determined in terms of several dimensionless quantities. The local Sherwood number, Sh is defined as:

$$Sh = \frac{h_m d}{D} \tag{19}$$

Where d is the hydraulic dimeter, D is the binary diffusion coefficient of the mixture, and h_m is the mass transfer coefficient and can be defined as:

$$h_m = \frac{-D\frac{\partial N_a}{\partial r}}{(N_m - N_w)} \tag{20}$$

Here N_m is the bulk mole fraction of the species “a”, N_w is the mole fraction of species “a” at the membrane surface.

The average friction factor across the hollow fiber bank is given by:

$$fr = \frac{2d}{\rho U_{inlet}{}^2} \frac{\Delta p_L}{L} \tag{21}$$

where Δp_L is the pressure drop across the hollow fiber bank, L is the length of the computational domain and U_{inlet} is the average inlet fluid velocity.

The Reynolds number is defined as:

$$Re = U_{inlet} d/\nu \tag{22}$$

In this study, for all geometries considered, only Re is varied and the rest of the dimensionless parameters are fixed.

CHAPTER 3: THREE DIMENSIONAL FLOWS CROSS FLOW ARRANGEMENT - GAS SEPARATION

3.1. GEOMETRY

Two three-dimensional HFM module flow geometries are examined – staggered and inline arrangements. The corresponding HFM bank (tow or group of individual fibers) schematics exhibiting inline and staggered arrangements of the HFMs are illustrated in Fig. 1a and Fig. 1b, respectively. The rectangular cuboid illustrated in Fig. 1 represents the computational flow domain where the flow inlet and outlet are indicated. The HFMB is comprised of the individual HFMs, whose cross-sections are indicated by the circles on the longest face of the cuboid. The HFMB is oriented so that the individual HFMs are oriented perpendicular to the flow direction thereby facilitating the crossflow regime. The dimensions of the cuboid are given in terms of the HFM hydraulic diameter, *d*, and are shown in Fig. 1. The length of the computational domain is indicated by *L*, and *S* illustrates the spacing between adjacent HFMs measured center-to-center. The stream-wise direction is measured by the x-axis, the y-axis measures the span-wise direction, and the cross flow direction is measured by the z-axis that coincides with the axis of the HFMs. Lastly, both HFMB arrangements are comprised of nine HFM columns and four HFM rows.

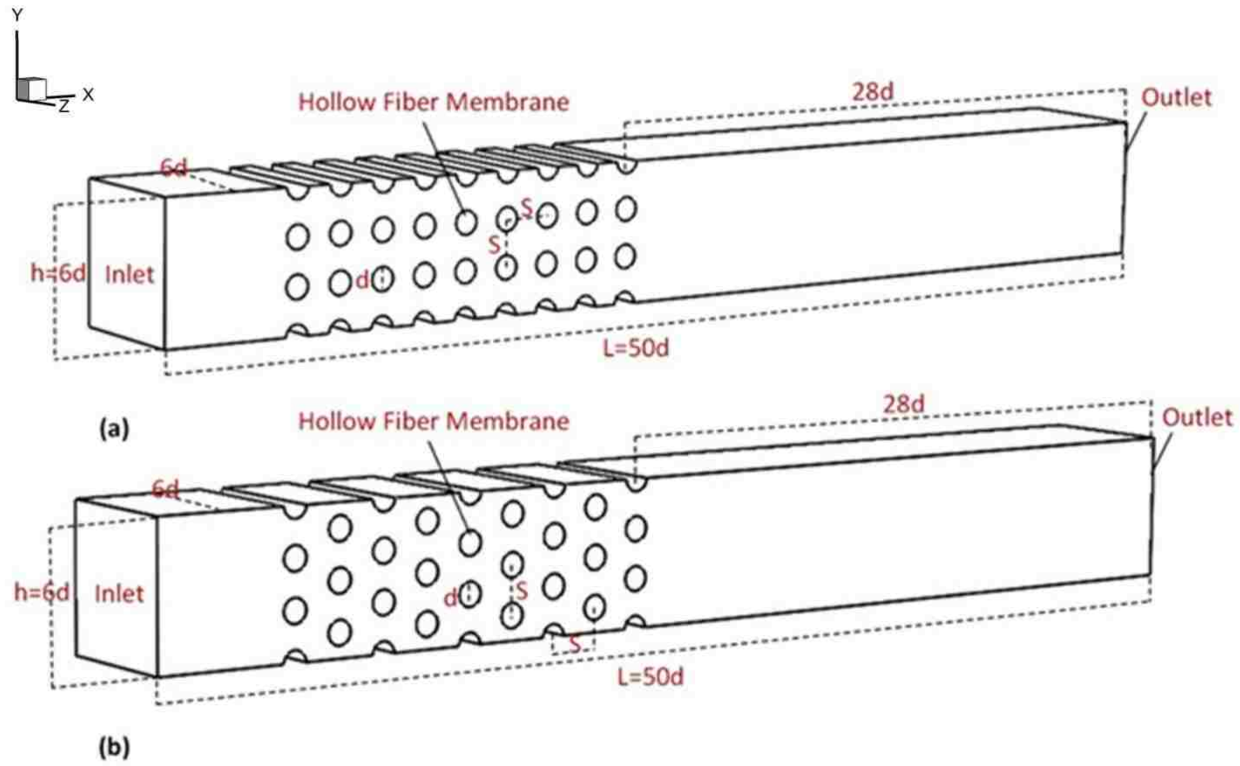

Fig. 1. Schematic of computational flow domain of *S/d=2* for (a) inline geometry and (b) staggered geometry. Dimensions of the flow domain and HFMB are illustrated.

Quantities in this work are made dimensionless by scaling with the appropriate fundamental values. HFMBs in both staggered and inline arrangements are considered for the values S/d=2 and S/d=3 with corresponding flow domain lengths of $L = 50d$ and $L = 58d$, respectively. For both considered values of S/d, the distance from the inlet to the center of the first HFM column as well as the breadth of the HFMB is $6d$. The height, h, of the HFMB is $6d$ and $9d$ for S/d=2 and S/d=3, respectively. The distance from the center of the last HFM column to the outlet is $28d$ for both values of S/d.

3.2. MESH STUDY

In order to assess the spectral convergence of the HFM simulations, a mesh optimization study is performed utilizing three mesh densities for the aforementioned computational flow domain: 24, 35, and 52 million (M) mesh elements. Molar fraction of

CH4 and normalized suction rate profiles along HFM cross-sections are plotted in Fig. 2a and Fig. 2b, respectively, where the profiles are obtained at the $x = 16d$ plane for $Re = 1000$ in the staggered geometry with $S/d = 2$ for the three mesh densities. Fig. 2c illustrates the normalized stream-wise velocity component profiles, where velocity is normalized by the inlet velocity, and the profiles are obtained at the $x = 17d$ plane for $Re = 1000$ in the staggered geometry with $S/d = 2$ for the three mesh densities. The $x = 16d$ plane corresponds to the HFMB cross-section intersecting the sixth HFM column, and $x = 17d$ plane is situated in the space in between the sixth and seventh HFM column. Molar fraction of CH4, suction rate, and velocity profiles utilizing 35M and 52M mesh elements are nearly identical as shown, however the profiles obtained for simulations utilizing 24M mesh elements deviate slightly. Discrepancies between data obtained for 35M and 52M mesh elements are sufficiently small that spectral convergence is achieved for 35M mesh elements. All results presented in the current work utilize 35M mesh elements for the steady SST simulations. Fig. 3 illustrates the mesh discretization near a HFM surface. The mesh rendering is finer for the boundary layer region in order to better characterize flow and concentration phenomena. The mesh discretization structure illustrated for the regions outside of the HFM boundary layer is employed in this study; the number of mesh elements for the computational flow domain totals to 35 million.

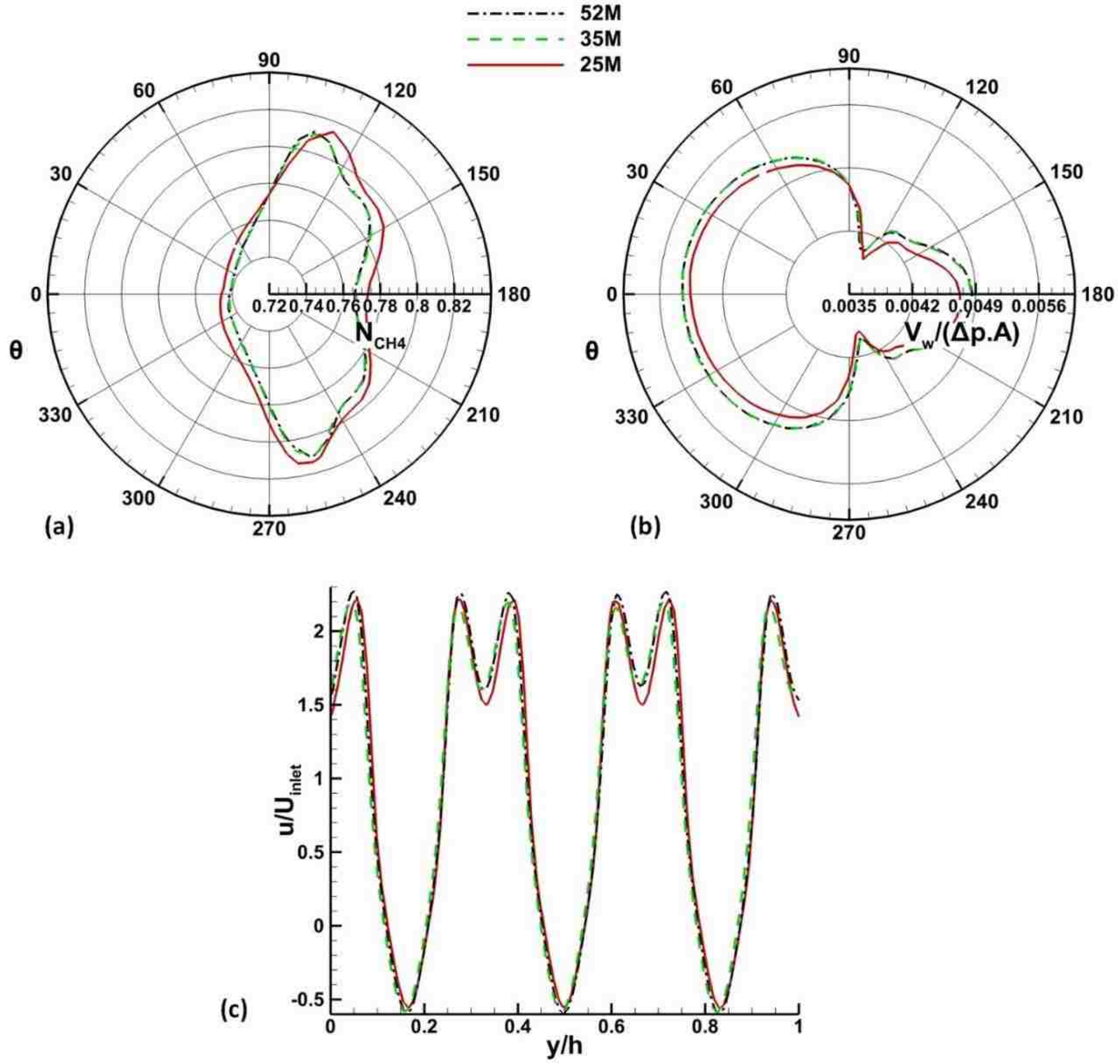

Fig. 2. HFM cross-section profiles at the *x=16d* plane for varying mesh densities in the staggered geometry with *S/d*=2 at *Re*=1000 for (a) molar fraction concentration and (b) suction rate. Profiles are calculated for the HFM located in the 6th column at the *z=3d* plane. (c) Normalized stream-wise velocity component profiles of the HFMB at the *x=17d* plane for varying mesh densities in the staggered geometry with *S/d=2* at *Re*=1000, where velocity is normalized by the inlet velocity.

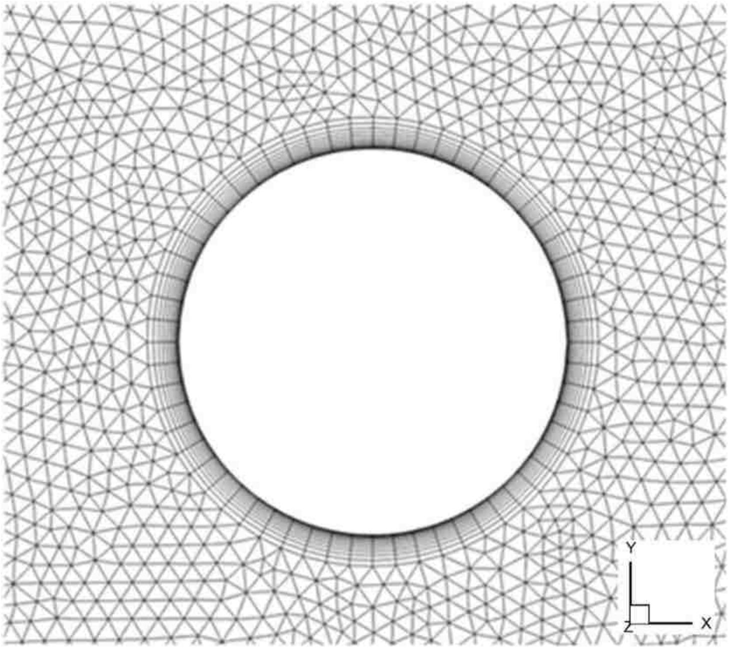

Fig. 3. Mesh discretization structure for any given HFM, where the mesh elements total to 35M for the entire domain.

3.3. RESULTS

To better understand steady state mass transport phenomena associated with the separation of $\mathrm{CO_2}$ from $\mathrm{CH_4}$, CFD simulations of $\mathrm{CO_2}$ diffusion through permeable HFMs are conducted. The Navier-Stokes and mass transport equations are solved to determine the flow and concentration fields in the three-dimensional feed channel containing HFMs arranged in either an inline or staggered geometry for two values of S/d and $200 \le Re \le 1000$. The $\mathrm{CO_2}$ permeation rate through the membrane varies with the local concentration.

Fig. 4 illustrates iso-surfaces of the stream-wise velocity component at Re=1000 and S/d=2 for the inline and staggered geometry, respectively. The velocity field becomes repeated behind each column of HFM in the stream-wise direction almost immediately after the flow has passed the second HFM column in both configurations.

The inline arrangement flow structure exhibits two distinct characteristics – a jet flow region in the stream-wise direction occupying the open channels in between HFM rows, indicated by the orange iso-surfaces, and a circulating wake flow region occupying any given HFM row that spans the space behind a HFM and the immediately adjacent downstream HFM, indicated by the blue iso-surfaces. In the inline geometry, the high-speed jet flow region exists because the flow is free to traverse the HFMB uninterruptedly in the open channels created by the HFM columns, thereby enabling the full development of the velocity boundary layer and permitting the flow to attain moderately high speeds. The inline arrangement of HFMs facilitates minimal interaction between the wake and jet flow regions, which abets the development of isolated longitudinal "strips" that alternate between regions of wake flow and jet flow indicated in Fig. 4a by the blue and orange strips, respectively. Interestingly, Fig. 4a illustrates three-dimensional flow structures existing behind HFMs that unexpectedly vary in the *z*-direction and resemble a sort of "velocity bump" in the iso-surfaces. It has not been illustrated here but is worth noting that the size of these structures increases with flow rate – the flow illustrated in Fig. 4a is at *Re*=1000. These three-dimensional structures enhance the performance of the separation module for the inline geometry, especially for high flow rates.

The velocity field in the HFMB arranged in the staggered geometry, seen in Fig. 4b, is more complex, and lacks the characteristically long jet flow regions in the stream-wise direction observed previously for the inline arrangement – rather two smaller jet flow regions higher in velocity engulf the leading edge of the HFMs, and are referred to as the double jet flow region indicated in Fig. 4b by the orange and red iso-surfaces. The flow in the staggered arrangement is constantly impeded by subsequent HFMs, and is forced to accelerate significantly as it diverges around the HFM leading edges (near the locations of flow separation) during the downstream journey thereby creating numerous dispersed regions of high and low shear near the forward and backward stagnation points, respectively. The staggered HFMB geometry effectively acts to scatter the fluid with each passing HFM column and can be thought of as a means to increase the momentum mixing within the fluid. The increased momentum mixing subsequently disrupts HFM boundary layer development as well as decreases the size of wake flow regions, which we will later show acts to increase separation module efficiency. Interestingly, the regions of circulating wake flow decrease in size from the inline to the staggered geometry, however, the staggered geometry introduces a small region of recirculating back flow, indicated in Fig. 4b by the dark blue regions that did not exist for the flow in the inline geometry.

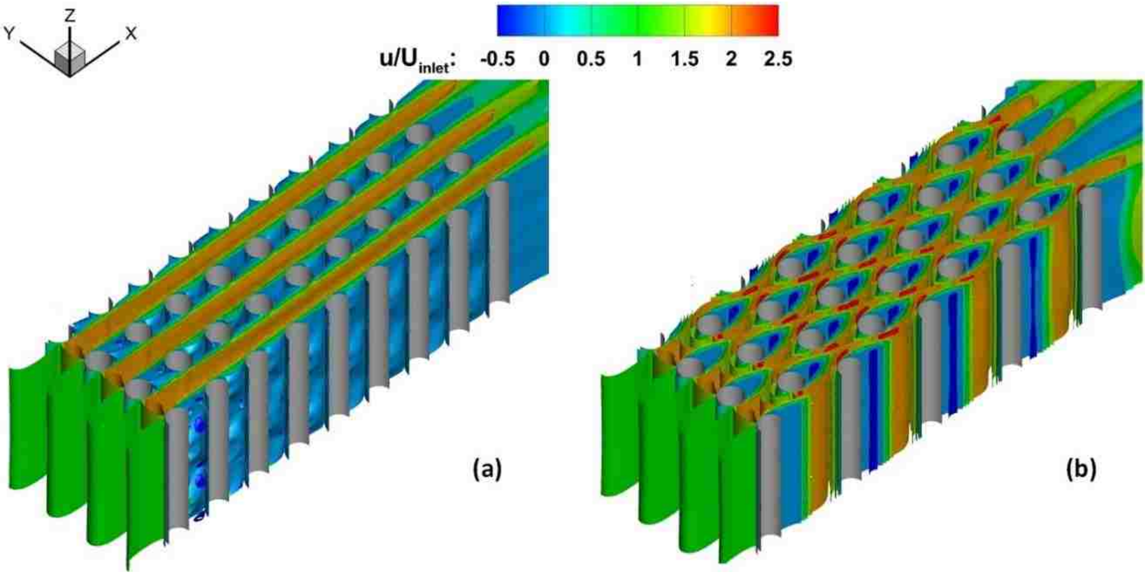

Fig. 4. Normalized stream-wise velocity component for *Re*= 1000 at *S/d*=2 for (a) inline geometry and (b) staggered geometry. Velocity was normalized by the inlet velocity.

Fig. 5 illustrates normalized vorticity component iso-surfaces for *Re*=1000 at *S/d*=2 for inline and staggered geometries, where the vorticity is normalized by the HFM hydraulic diameter divided by the inlet velocity, d/U_{inlet}. All three spatial vorticity components exhibit periodic behavior in the flow direction. For both the x- and y-components of vorticity, the vortical structures observed for the inline geometry are considerably larger than the vortical structures in the staggered geometry. The flow in the staggered geometry is unable to develop the larger vortical structures in the HFMB because the flow is repeatedly forced to scatter and navigate around the obstacle-like HFMs, thereby inhibiting the flows ability to develop large vortical structures. The resulting vortical structures for the staggered geometry are numerous, small vorticity pockets in the flow. The presence of the smaller vortical structures in the staggered geometry indicates that momentum mixing occurs most readily in the staggered geometry – this mixing enhances separation module performance. Lastly, it is clear that the z-component of vorticity is dominating the flow structures for both inline and staggered geometries, illustrated in Fig. 5e and Fig. 5f. The vorticity field in both geometry clearly illustrates the presence of strong three dimensional effects at higher flow rates.

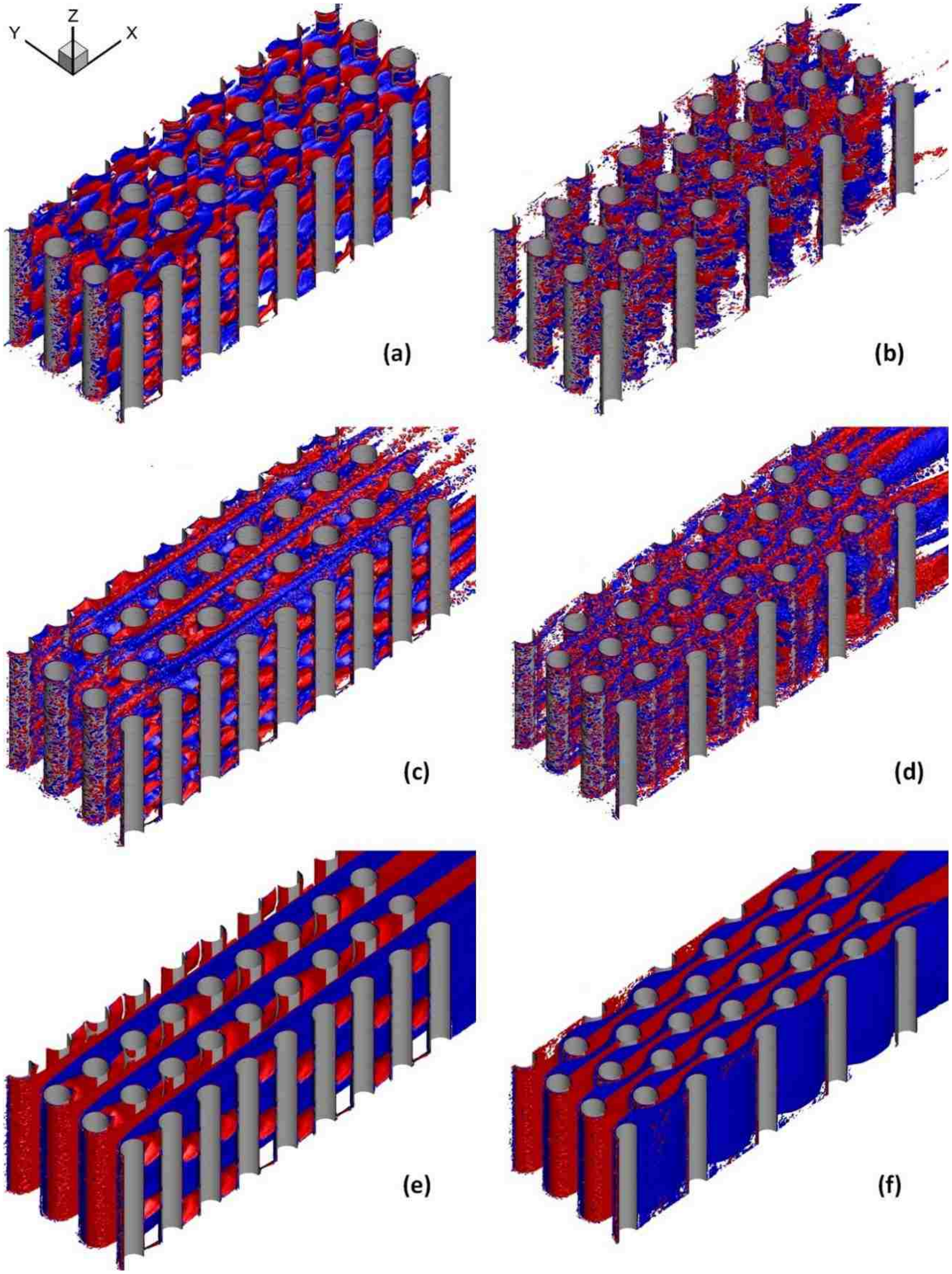

Fig. 5. Illustrations of the normalized vorticity components for *Re*=1000 at *S/d*=2 in the inline geometry: (a) $x-$ (c) $y-$ and (e) $z-$ component of vorticity in the staggered geometry: (b) $x-$ (d) $y-$, and (f) $z-$ component of vorticity. Vorticity is normalized by the HFM hydraulic diameter divided by the inlet velocity, d/U_{inlet}. The vorticity level -0.21 is indicated in blue, and 0.21 is indicated in red.

The Q-criterion is employed in order to characterize the vortex structures in the flow field. The Q-criterion is defined as

$$Q = \frac{1}{2}(\|S\|^2 - \|\Omega\|^2) \tag{23}$$

where S is the strain tensor and Ω is the rotation tensor. Fig. 5 and Fig. 6 indicate that the z-component of the normalized vorticity and the Q-criterion are strongly correlated for both inline and staggered geometries. There is also a strong correlation between iso-surfaces of the concentration and the Q-criterion, as shown in Fig. 6 and Fig. 7. They do display the similar structures. One significant difference is that iso-surfaces of the Q-criterion clearly shows that the momentum layer quickly settles and becomes repeated passing each row of HFM in both geometry, on the other hand, concentration layer develop slower becomes repeated after 6-th row in the inline geometry and after 7-th row in the staggered geometry. For the inline geometry, the jet flow region at each side the HFM along each row improves membrane performance. However, there is significant concentration polarization near the forward and backward stagnation regions for the inline geometry; additionally, there is vortex shedding in the area where the boundary layer detaches from HFM surface. In the staggered geometry, there is a strong vortex shedding around HFM surface. These large vortex shedding activities indicate that the staggered geometry perform better compared to the inline geometry. This clearly illustrates the importance of studying the vorticity field to indicate concentration behavior and separation regions along the HFM surface.

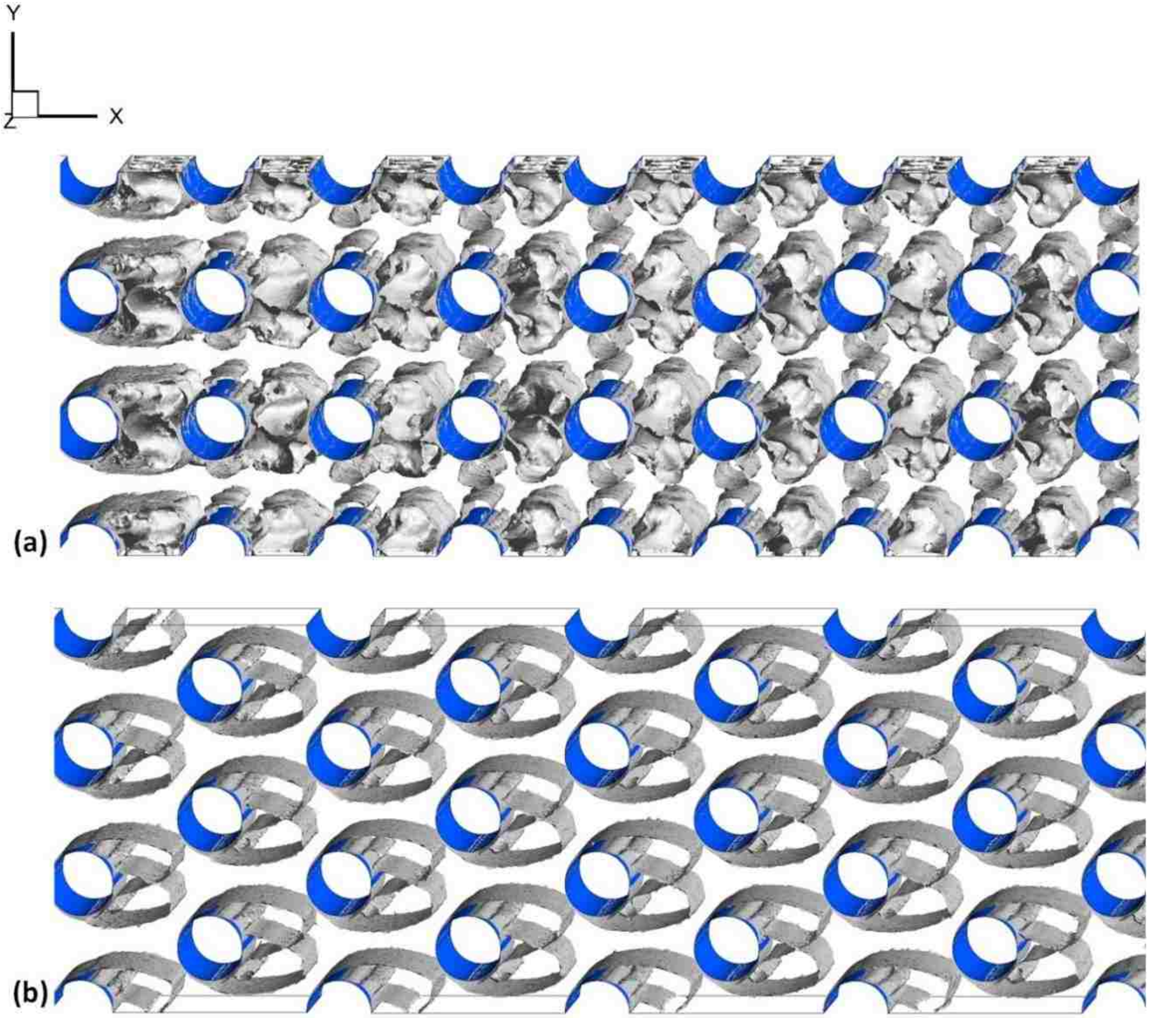

Fig. 6. The *Q*-criterion for *Re*= 1000 at *S/d*=2 (*Q*=0.01) for (a) inline and (b) staggered geometries.

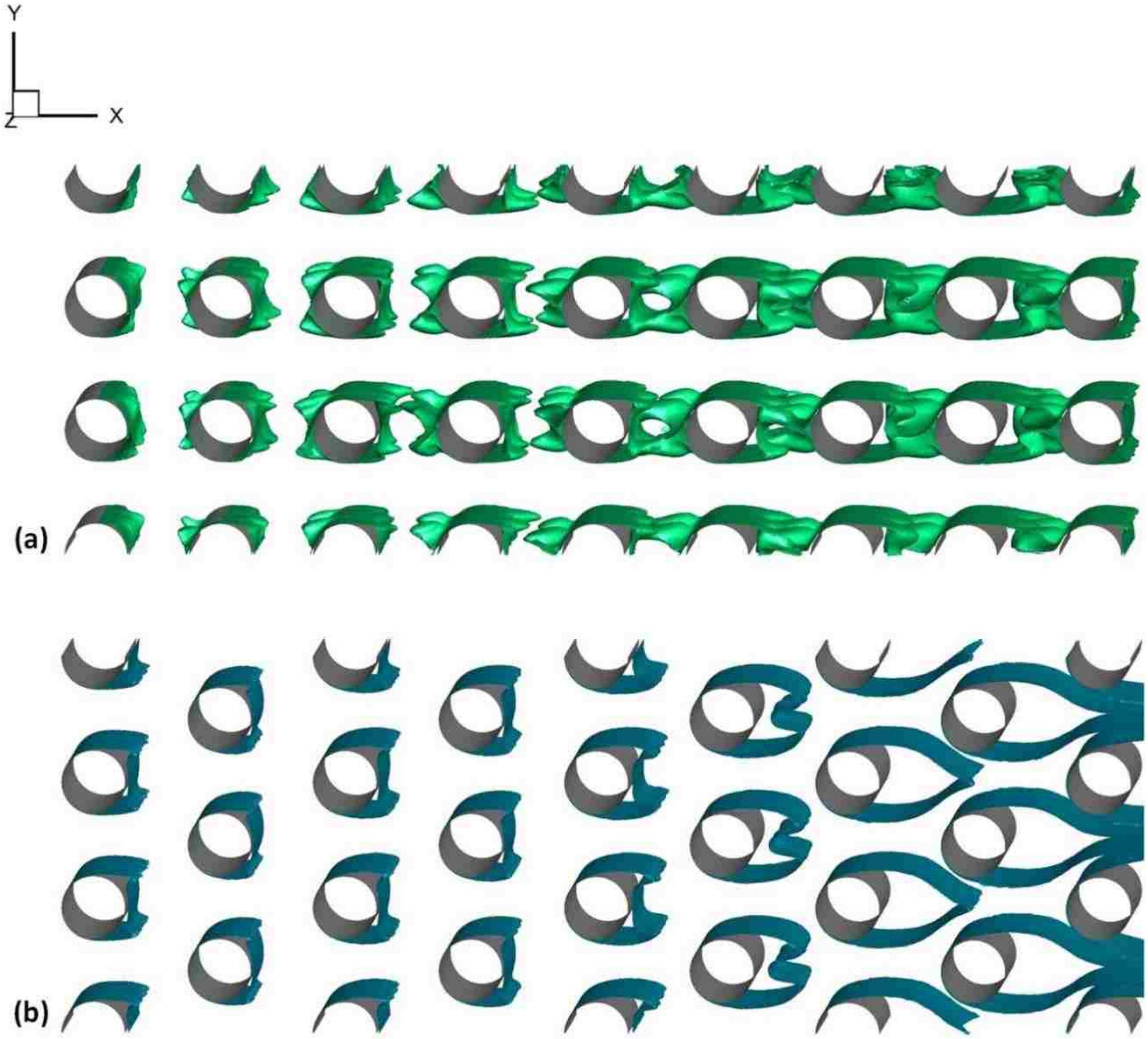

Fig. 7. Mole fraction concentration iso-surfaces for *Re*= 1000 at *S/d*=2 for (a) inline (N_{CH4}=0.76) and (b) staggered geometries (N_{CH4}=0.74).

Fig. 8 illustrates steady state three-dimensional CH_4 mole fraction contours for various Re at $S/d = 2$ for inline and staggered geometries. Fig. 8 illustrates an uniformly low $\mathrm{CH_4}$ concentration in the jet flow region, and a slightly higher concentration in the vicinity of the backward stagnation point for the inline case at all values of Re. The flow for the inline HFM arrangements is free to traverse the HFMB uninterruptedly in the jet flow region, thus fluid mixing is minimal at these locations and abets significant concentration polarization along HFM surfaces. HFM surfaces near to the jet flow regions are subjected to high shearing and suction that result in low $\mathrm{CH_4}$ concentrations at these surface locations for inline geometries. Conversely, the HFM surfaces near the forward and backward stagnation points are subjected to low shearing and suction that result in high $\mathrm{CH_4}$ concentrations at these surface locations for inline geometries. The differences in shearing, suction rate, and vorticity cause concentration polarization along HFM surfaces. As flow rate increases from $Re = 400$ to $Re = 1000$, the degree of concentration polarization is lessened, but is present nonetheless. There is a higher level of concentration polarization near the region where the boundary layer detaches from the surface of the HFMs. The staggered arrangement exhibits significantly less concentration polarization in the region near the forward stagnation point and near to where the flow separates from the HFM surface. This demonstrates that concentration boundary layer disruption by the presence of HFMs in the staggered geometry effectively reduces concentration polarization by retarding the full development of the concentration boundary layer.

In both geometries, the concentration is higher in the downstream region behind the HFMs, and the concentration polarization is reduced as the flow rate is increased to $Re = 1000$, which agrees with results from [35]. Momentum mixing induced by the presence of HFMs in the feed channel is the main factor contributing to concentration polarization reduction at higher feed flow rates, especially for staggered geometries as compared to inline geometries. The degree of momentum mixing in the staggered configuration is higher than that in the inline configuration. As the mixture flows further downstream in the HFMB, it becomes gradually $\mathrm{CH_4}$ rich as $\mathrm{CO_2}$ diffuses into the membranes.

The concentration near the backward stagnation point for all HFMs remains elevated throughout the entire HFMB as compared to the forward stagnation point region.

Increased mixing in the HFMB for staggered geometries diminishes the concentration polarization, which is expected to improve the membrane performance.

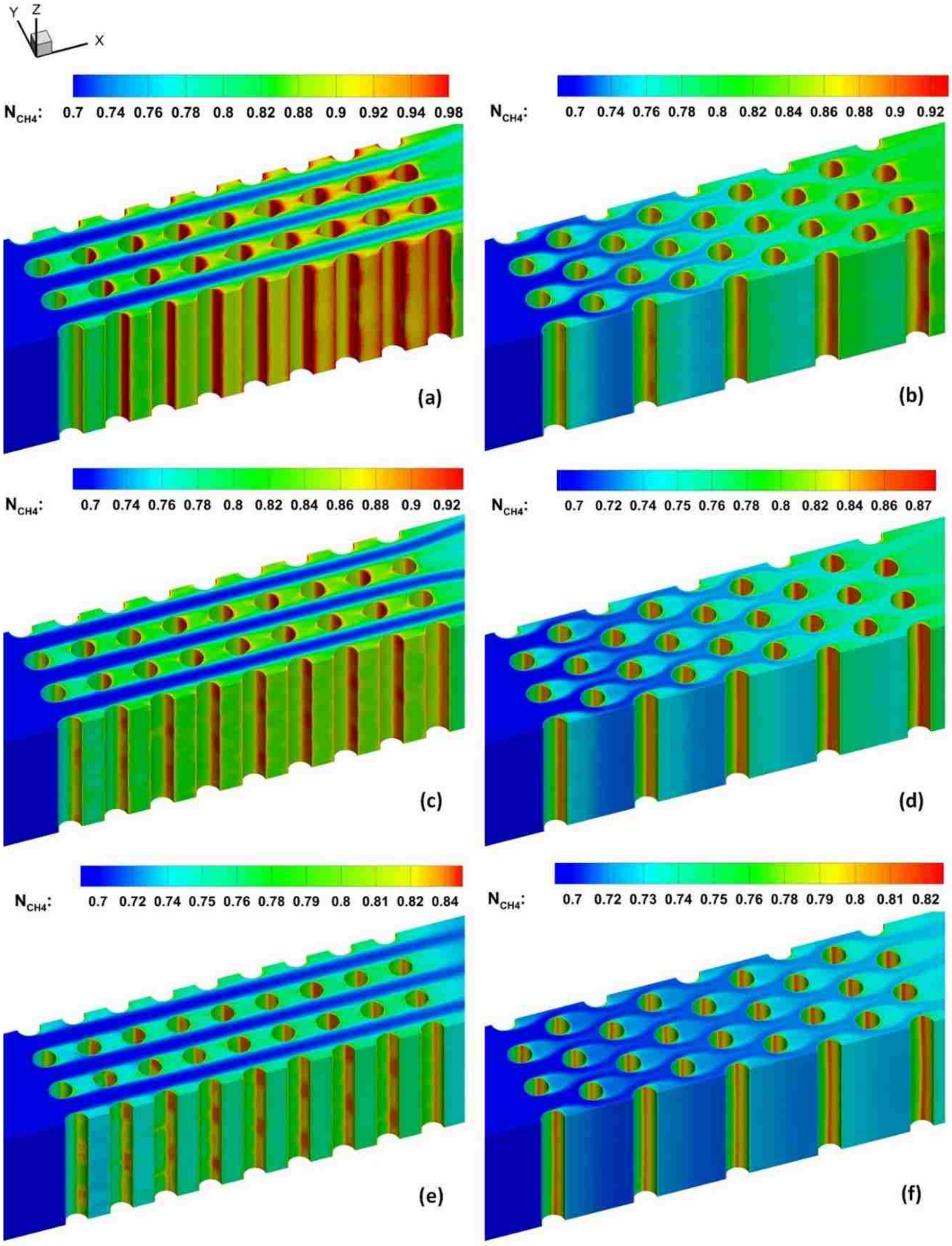

Fig. 8. CH$_4$ mole fraction concentration contours at *S/d*=2 for: *Re*=200 in the (a) inline geometry, and (b) staggered geometry, *Re*=400 in the (c) inline geometry and, (d) staggered geometry, and *Re*=1000 in the (e) inline geometry, and (f) staggered geometry.

Fig. 9 illustrates the normalized suction rate along the surface of HFM at *S/d*=2 for various *Re* in inline and staggered geometries, where the suction rate is normalized by the pressure difference across the membrane times the permeability, $\Delta p.A$. Suction rate in both geometries increases with *Re*. For all flow rates, HFMs arranged in staggered geometries exhibit significantly higher suction rates as compared to those in inline geometries. In both geometries, the suction rate is lowest where the boundary layer detaches from the HFM surface. Flow separation characteristics differ significantly between geometries and the locations where boundary layers detach vary with the feed flow rate – especially for inline geometries. For the inline geometry at *Re*=200, the suction rate drastically decreases after the first two columns then exhibit a lower uniform value until the last column. At *Re*=400, a similar suction phenomenon is observed but with larger suction rates. As the flow rate is increased to *Re=1000*, the suction rate becomes higher at locations where flow separation occurs. As illustrated in Fig. 9, the suction rate assumes the lowest value in the region most near to the backward stagnation point in both geometries. Interestingly, as the flow propagates through the HFMB the suction rate gradually decreases for the staggered geometry but significantly decreases for the inline geometry. Fig. 9 illustrates that the suction rates are significantly higher for HFMB arranged in staggered geometries as compared to inline geometries for all flow rates.

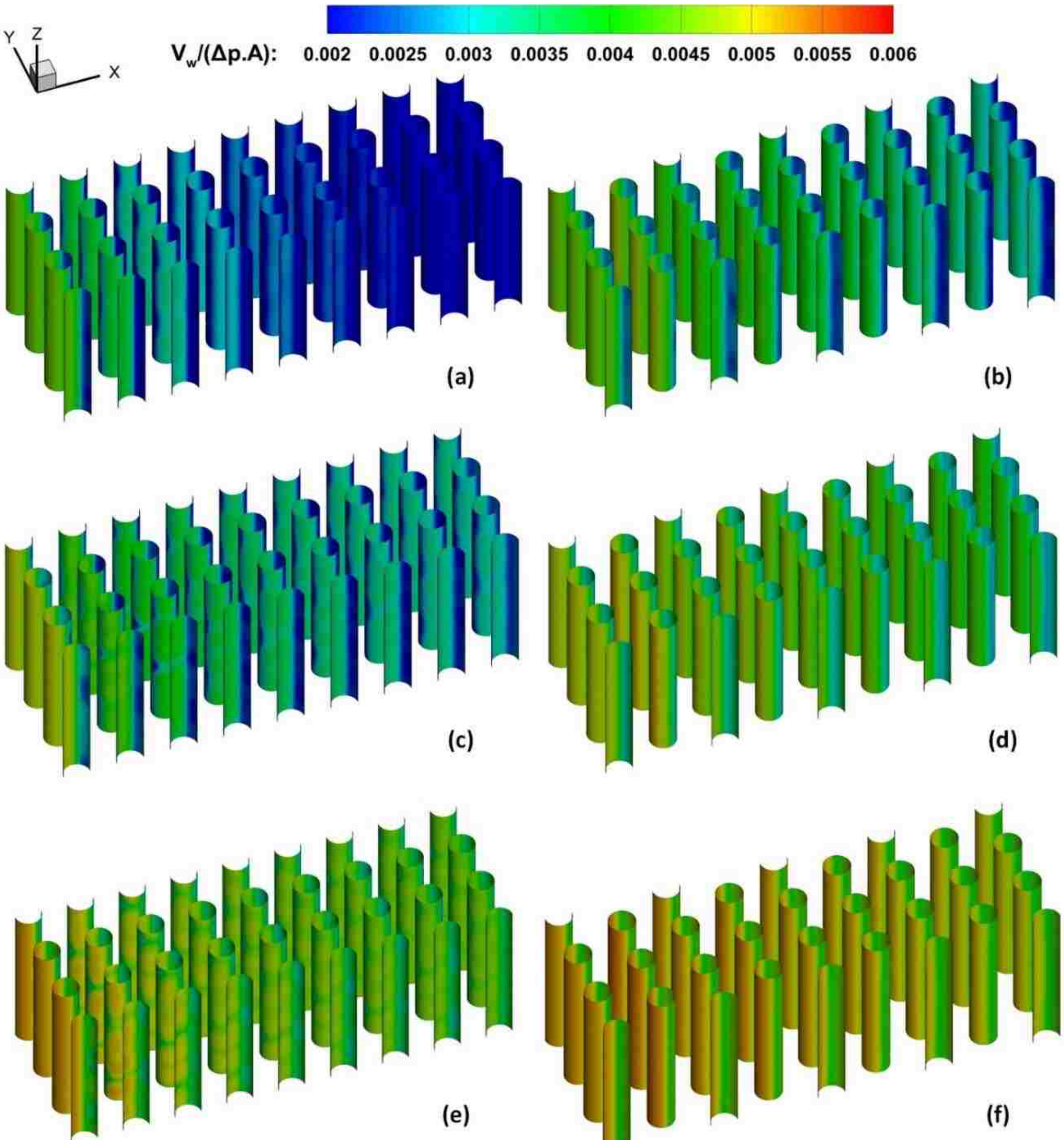

Fig. 9. Normalized suction rate at *S/d=2* for: *Re=200* in the (a) inline and (b) staggered geometries, *Re=400* in the (c) inline and (d) staggered geometries, and *Re=1000* in the (e) inline and (f) staggered geometries. The suction rate is normalized by the pressure difference across the membrane times the permeability, *Δp.A*.

Fig. 10 illustrates CH_4 mole fraction, suction rate, vorticity magnitude, and wall shear stress profiles along the surface of the HFM in the seventh column and third row down from the top for inline and staggered geometries for $Re = 200$ at *S/d*=2. HFM surface regions exhibiting high vorticity also exhibit low CH_4 mole fraction, high suction rate, and high shearing for both geometries. Low shear regions occur near to where boundary layers detach from the HFM surface. Throughout the HFMB for both geometries, wall shear is largest in regions where a surface is near to a high-speed, or jet flow, region – such as the jet flow and double jet flow regions in the inline and staggered arrangements illustrated in Fig. 4a and Fig. 4b, respectively.

Fig. 10e and Fig. 10f illustrates the streamtraces for the aforementioned HFM for the inline and staggered geometry. The flow structures near the forward stagnation region differ between geometries; the streamtraces indicate two small slowly circulating wake flow regions just upstream of the HFM leading edge in the inline arrangement, and a strongly impinging flow that is forced to diverge around the HFM leading edge with high speeds in the staggered arrangement. Fig. 10 illustrates the interdependence of the flow characteristics on the membrane performance – the regions where the flow velocity is large, indicated by the streamtraces in Fig. 10e and Fig. 10f, correspond to regions of low $\mathrm{CH_4}$ mole fraction, high suction, and high vorticity, which indicate the HFM surfaces interfacing these regions have high performance. That is it say, HFMs perform most efficiently when the neighboring flow exhibits significant momentum mixing within the fluid. Both geometries exhibit unfavorable flow structures in the circulating wake flow regions near the backward stagnation point, however, favorable flow structures are recovered quickly in the staggered geometry because the downstream peripheral HFMs act to diverge the flow into the circulating wake flow region, illustrated in Fig. 10f. The feed channel flow rate and resulting flow structures near the HFM surfaces for a given HFM arrangement are of crucial importance for achieving high separation module performance.

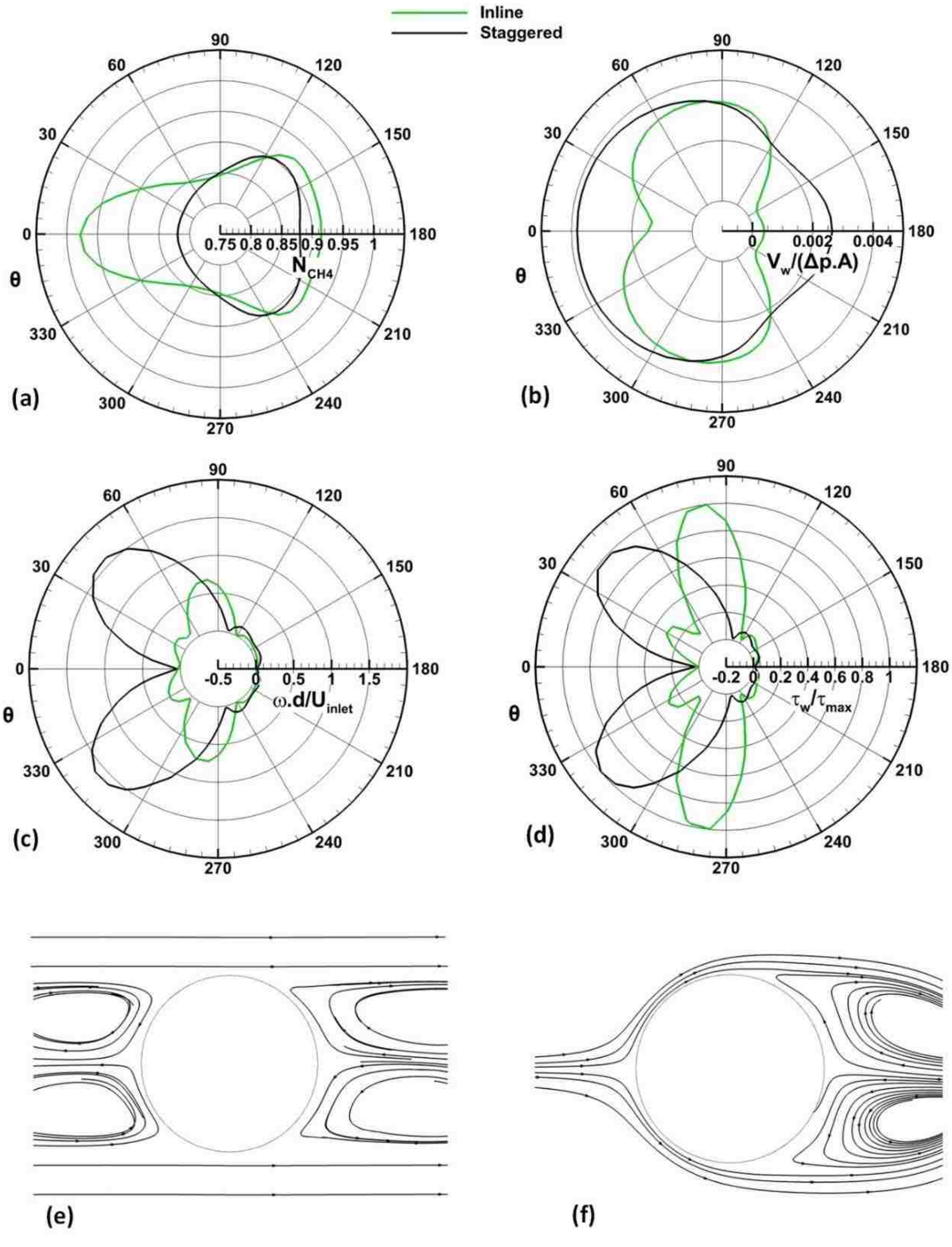

Fig. 10. (a) CH_4 mole fraction, (b) suction rate, (c) vorticity magnitude, and (d) wall shear stress profiles along the HFM surface for inline and staggered geometries as well as streamtraces for (e) inline and (f) staggered geometries of the HFM in the seventh column and third row down from the top for *Re=200* at *S/d=2* in the *z=3d* plane.

Sherwood number, *Sh*, represents the ratio of convective mass transfer to the rate of diffusive mass transfer and is presented in this work to assess the overall CO_2 diffusion into HFM surfaces. Fig. 11 illustrates *Sh* profiles along the surface of the HFM in the seventh column and the third row down from the top at the $z=3d$ plane for inline and staggered geometries at various values of *Re* and *S/d*. Fig. 11 indicates that *Sh* is consistently larger for the staggered geometry, and increases with the feed flow rate for both geometries. The HFM spacing ratio $S/d=2$ facilitated the greatest difference in *Sh* profiles between staggered and inline geometries. The *Sh* profiles strongly resemble the suction rate profiles shown previously in Fig. 10, which suggests that regions with greater suction rate exhibit greater momentum mixing thereby enabling greater mass transfer through the HFMs. For the staggered geometry, *Sh* is largest at the HFM leading edge where CH_4 mole fraction concentration, suction rate, and vorticity magnitude are also large. However, for the inline arrangement, *Sh* assumes the largest value slightly further along the HFM surface near to where suction rate is large and boundary layer separation occurs. *Sh* is small at the localized forward stagnation points for the inline geometry. On the other hand, *Sh* is large at the localized forward stagnation point in the staggered geometry. The *Sh* value in both geometries increases with *Re* near the backward stagnation point.

The entire backside of the HFM surface is exposed to the wake flow region and exhibits a smaller *Sh* as compared to the leading edge HFM surface for both spacings because the suction rate and vorticity are generally higher in the leading edge region for both geometries as illustrated in Fig. 10. Sherwood number and separation module performance are higher in regions where high-speed flows are observed – such as the jet flow region in the inline geometry and the double jet flow region in the staggered geometry (see Fig. 11). The staggered geometry allowed for the HFM surface in the leading edge region to achieve considerably higher *Sh*, and therefore perform significantly better compared to the inline geometry. Interestingly, the HFM surface in the trailing wake flow region exhibited very similar *Sh* profiles for all values of *Re* and *S/d*.

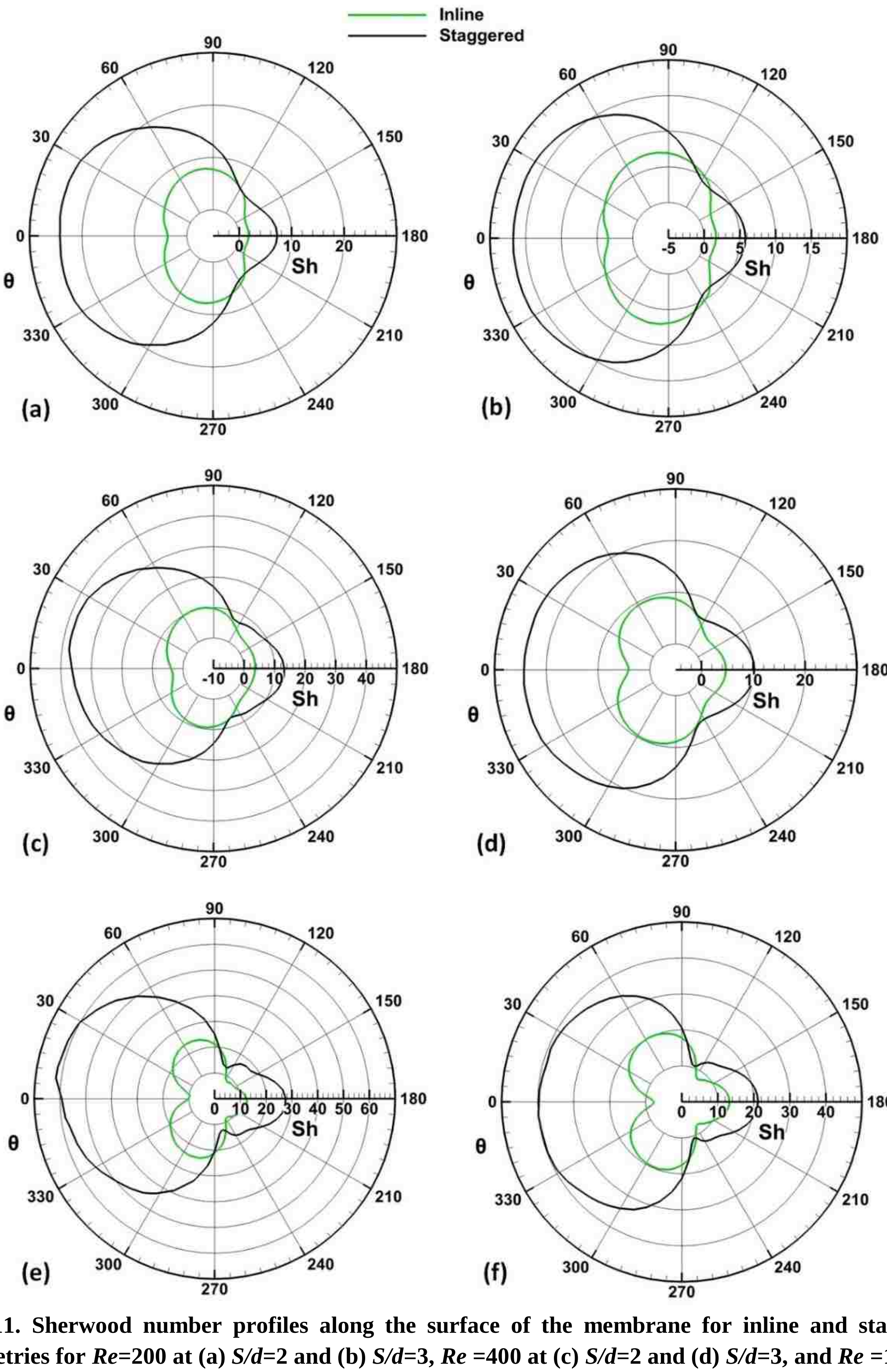

Fig. 11. Sherwood number profiles along the surface of the membrane for inline and staggered geometries for *Re*=200 at (a) *S/d*=2 and (b) *S/d*=3, *Re* =400 at (c) *S/d*=2 and (d) *S/d*=3, and *Re* =1000 at (e) *S/d*=2 and (f) *S/d*=3. Profiles are calculated for the HFM located at the seventh column and the third column down from the top at the z=*3d* plane.

The local Sh was calculated for all regions in the HFMB, but was not illustrated in this work. It was observed that the local Sh for the first, second, and last HFM columns would differ significantly from the interior HFMs of columns three to eight, which we expected. The first and the second HFM columns are the first to encounter the incoming feed fluid, which explains the increased local Sh for these columns, especially in the leading edge region, because the fluid is more uniformly mixed here. The average Sherwood number, $\overline{Sh}$, for the third to eighth HFM columns is calculated for the inline and staggered geometry at various values of Re and S/d and is shown in Table 1. $\overline{Sh}$ increases with Re, and is consistently larger for the staggered geometry. At large Re, the difference in $\overline{Sh}$ becomes quite large between the staggered and inline geometries – at Re=1000, $\overline{Sh}$ is about two times larger in the staggered geometry compared to the inline geometry. $\overline{Sh}$ is not sensitive to the spacing between HFM in both geometries, as depicted in Table 1. Clearly, the arrangement of HFMs is of crucial importance when designing and optimizing separation modules.

Re	**Average Sherwood Number – $\overline{\mathrm{Sh}}$**			
	S/d=2		***S/d=3***	
	Inline	***Staggered***	***Inline***	***Staggered***
200	**4.91**	**9.88**	**4.67**	**8.62**
400	**6.10**	**14.46**	**6.33**	**12.45**
1000	**14.23**	**25.40**	**13.16**	**21.50**

Table 1. Average Sherwood number of the third to eighth HFM columns in the inline and staggered geometries at various values of Re and S/d.

The friction factor across the HFMB is given in Table 2 for the inline and staggered geometries at various values of Re and S/d, and represent a measure of the energy loss for the system. Energy losses are lower in the inline geometry compared to the staggered geometry for the tabulated Re and S/d combinations. Table 2 indicates that the friction factor is not particularly sensitive to changes in flow rate for the considered range of Re. The inline arrangement facilitates a smaller pressure drop across the HFMB length. The friction factor is significantly higher in the module with a tighter spacing of HFM in both geometry.

Re	Friction Factor – fr			
	S/d=2		*S/d=3*	
	Inline	*Staggered*	*Inline*	*Staggered*
200	**0.039**	**0.079**	**0.013**	**0.057**
400	**0.035**	**0.072**	**0.012**	**0.056**
1000	**0.045**	**0.060**	**0.017**	**0.054**

Table 2. Friction factor across the HFMB length for the inline and staggered geometries at various values of Re and S/d.

The coefficient of performance (*COP*) is introduced to compare modules containing HFM with the inline and staggered arrangements. COP is defined as:

$$COP = \frac{Sh_s/Sh_i}{(fr_s/fr_i)^{1/3}} \tag{24}$$

The *COP* is the parameter employed to measure membrane flux improvement for a fixed pumping power. Here Sh_s and Sh_i are the average Sherwood numbers for all HFMs in the staggered and inline geometries, respectively. fr_s and fr_i are the friction factors for the staggered and inline HFMB geometries, respectively. Table 3 shows the *COP* for various values of Re and S/d, which are all greater than unity and indicate that the efficiency of the staggered geometry outweighs the efficiency of the inline geometry as well as the inefficiency of the staggered geometry. Table 3 indicates that the staggered arrangement of HFMs increases separation module performance compared to the inline arrangement. The staggered module performs better when HFM is tightly spaced. Performance comparison of modules is nearly the same at all flow rates considered.

Re	**Coefficient of Performance – COP**	
	S/d=2	***S/d=3***
200	**1.58**	**1.12**
400	**1.86**	**1.19**
1000	**1.63**	**1.12**

Table 3. Coefficient of performance values for various values of Re and S/d.

Another way to measure the HFM performance is by calculating $\dot{m}$, which is the mass flow rate of CO_2 per unit area diffusing through the membrane surface. $\dot{m}$ is defined as:

$$\dot{m} = \frac{1}{A_m}\left(\frac{\ddot{A}_a}{l}\Delta p_{tot}\right)\int_{A_m} N_{CO2}\, dA_m \qquad (25)$$

where A_m is the membrane surface area. Table 4 tabulates values of mass flow rate of CO_2 per unit area diffusing through the membrane surface for the inline and staggered arrangement for various values of Re and S/d. Table 4 confirms the HFM spacing ratio S/d=2 for the staggered geometry yields the greater mass flow rate. Examination of the average Sherwood number, coefficient of performance, and mass flow rate confirm that HFMs arranged in the staggered geometry facilitate the greatest separation module performance as compared to the inline geometry. Further, these results emphasize the importance of considering HFM arrangement in separation module design and optimization.

Re	**Mass Flow Rate – $\dot{m}$**			
	S/d=2		***S/d=3***	
	Inline	**Staggered**	**Inline**	**Staggered**
200	**0.0203**	**0.0242**	**0.0245**	**0.0241**
400	**0.0219**	**0.0295**	**0.0229**	**0.0289**
1000	**0.0311**	**0.0356**	**0.0310**	**0.0348**

Table 4. CO_2 mass flow rate per unit area across HFM surface for the staggered and inline arrangements at various values of Re and S/d.

3.4. CONCLUSION

Steady-state three-dimensional CFD simulations of carbon dioxide ($\mathrm{CO_2}$) removal from a binary mixture with methane ($\mathrm{CH_4}$) are performed using the steady k-ω SST turbulence model in order to characterize HFM performance. The separation module is arranged in the radial crossflow configuration, where the flow direction is normal to the HFM axes. Two different HFM arrangements within the module are examined, inline and staggered, and three values of Reynolds numbers are probed, $Re = 200, 400,$ and 1000. Membrane performance is assessed based on species mass flux across the HFM surface and the friction factor associated with the HFM arrangement. HFM surfaces are treated as a functional boundary where the mass flux of a species is calculated from the local partial pressure, permeability, and selectivity of the HFM. This work shows that three-dimensional analysis of flow through a HFMB is important because characterization of the velocity, vorticity, and concentration fields indicate the existence of three-dimensional flow structures that cannot be captured through two-dimensional analysis. Suction rate along the HFM surface is also affected by three-dimensional flow structures, chiefly for the inline HFM arrangement, and assumes a minimum value near to where boundary layer detachment occurs from the membrane surface for both HFM arrangements. Increased momentum mixing achieved with the staggered arrangement enhances HFM performance, and is observed through comparison of the x- and y-directions of vorticity that illustrate considerable differences in vortical structure size. Concentration polarization is influenced by the local flow around the HFMs. The staggered HFM arrangement displays a more uniform concentration distribution along the membrane surface, and abets a lesser degree of concentration polarization than the inline geometry. For the inline geometry, significant concentration polarization exists near the forward stagnation point where wake flow tends to be trapped and continuously recirculated. For both HFM arrangements however, high concentration polarization exists in regions of low speed flow, and low concentration polarization exists in regions of high speed flow. As the inlet flow rate increases in both HFM arrangements, concentration polarization is alleviated. Shear rate, suction rate, and vorticity magnitude are highest in regions of high speed flow, and lowest in regions of low speed flow. The averaged Sherwood number increases with the inlet flow rate, but is relatively insensitive to the change in membrane spacing. Sherwood number is high in regions of high speed flow, and low in regions of low speed flow. As the inlet flow rate increases for the inline geometry, Sherwood number assumes a minimum value at the forward stagnation point and near to where boundary layer detachment occurs from the membrane surface. However, for the staggered geometry, the Sherwood number greatly increases in the region of the forward stagnation point with the flow rate. For the larger HFM spacing, the COP is insensitive to flow rate and is near to unity, suggesting similar membrane performance. For the tighter HFM spacing, the COP is relatively insensitive to changes in Reynolds number, but has increased in value, indicating that the staggered HFM arrangement outperforms the inline arrangement for tighter the HFM spacing. Lastly, examination of the mass flow rate of $\mathrm{CO_2}$ across the HFM surface also suggests the staggered HFM arrangement permits for increased species separation.

CHAPTER 4: HYBRID REVERSE OSMOSIS GAS SEPARATION MODULE

4.1. GEOMETRY

Steady state flow simulations are conducted to study a gas separation process in a hybrid reverse osmosis module. The module contains a three-dimensional feed channel bounded by two parallel spiral wound membranes. The feed channel contains hollow fiber membranes with different arrangements and with a fixed spacing. The primary flow is parallel to the spiral wound membranes and perpendicular to the hollow fiber membrane axes. The schematic of the three-dimensional computational domain is shown in Fig. 12. An inline, a staggered and a *45°* net arrangement of HFMs are illustrated in Fig. 12a, b, and c, respectively. The diameter of the membrane is *d*, the spacing between two adjacent hollow fiber membranes measured center-to-center is *S*. The height, thickness, and length of the computational domain are *4d*, *10d*, and *140d*, respectively. The vertical gap between two adjacent hollow fiber membranes is *2d* from center to center. All three arrangements are designed for a fixed value of hollow fiber spacing distance, *S/d = 10*.

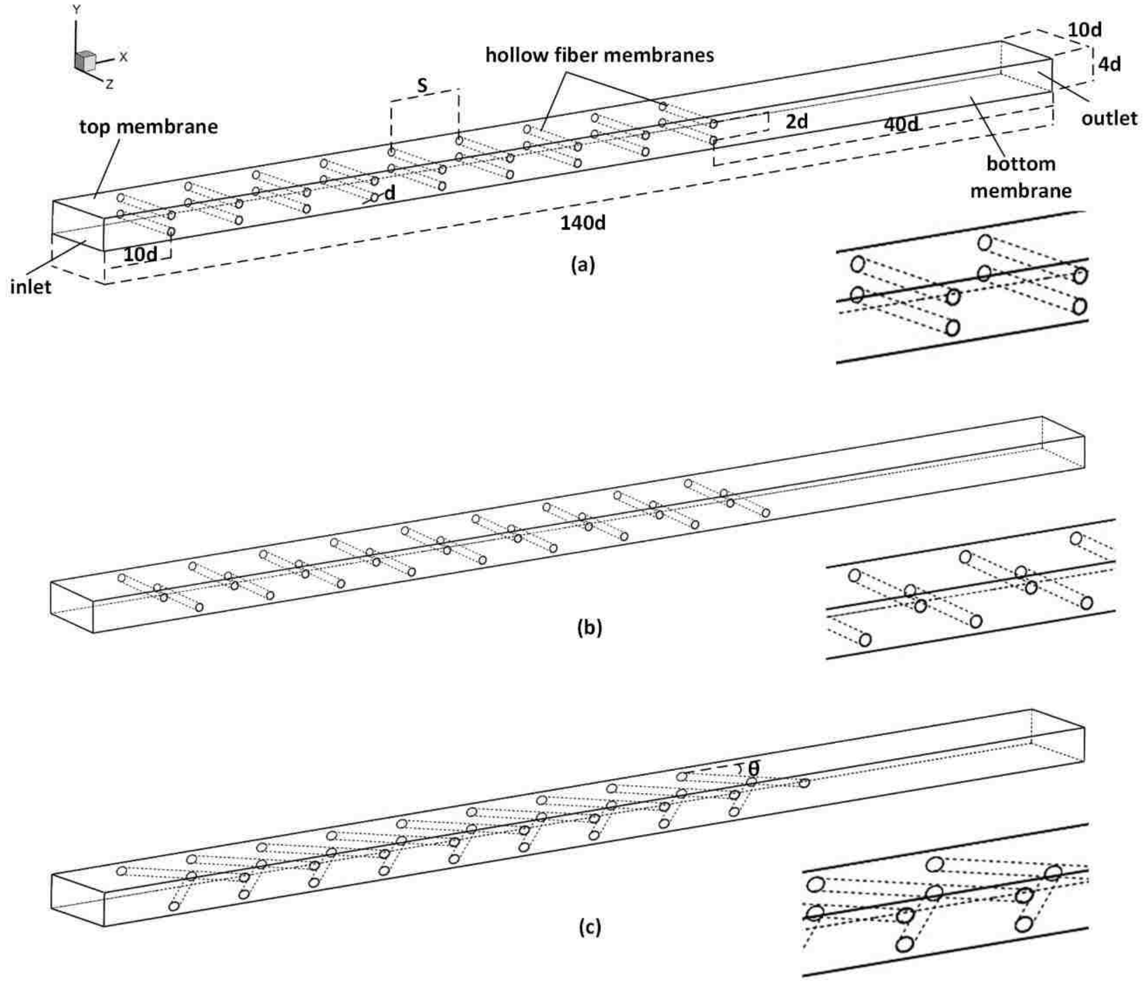

Fig. 12. Schematic of computational flow domain of *S/d=10* for (a) an inline geometry (b) a staggered geometry and (c) a net of HFMs with 45° geometry. Dimensions of the flow domain and HFMB are illustrated.

4.2. MESH STUDY

The numerical simulations are conducted for flow through a three-dimensional hybrid membrane geometry using the commercial software, CFX. A mesh optimization study is performed to ensure a spatial convergence. The grid mesh is refined in regions near membrane surface where high velocity and concentration gradients are expected. A mesh study is employed using three mesh densities in order to assess the spectral convergence of the HFM simulations. The three different mesh sizes selected for mesh convergence are

24, 32, and 50 million (M) mesh elements. Molar fraction of CH_4 and normalized suction rate profiles along HFM cross-sections are shown in Fig. 13a and b, respectively. The profiles are obtained at $x = 60d$ plane for $Re = 1000$ in the inline geometry and $S/d = 10$ using three mesh densities. The plane at $x = 60d$ corresponds to the HFMB cross-section intersecting the sixth HFM column. Fig. 13c illustrates profiles of the stream-wise component of the velocity. It is normalized by the inlet average velocity, and the profiles are obtained at $x = 65d$ plane. The plane $x = 65d$ is situated between the sixth and seventh HFM column. Profiles of the mole fraction, the suction rate, and the stream-wise velocity obtained using 32M and 50M mesh elements are nearly the same as depicted in Fig. 13. Deviations between profiles for 32M and 50M mesh elements are sufficiently small that spectral convergence is achieved for 32M mesh elements. In other words, the numerical solution becomes nearly independent of mesh size as 32M mesh elements are used. Hence simulation results presented in this chapter are acquired utilizing 32M mesh elements.

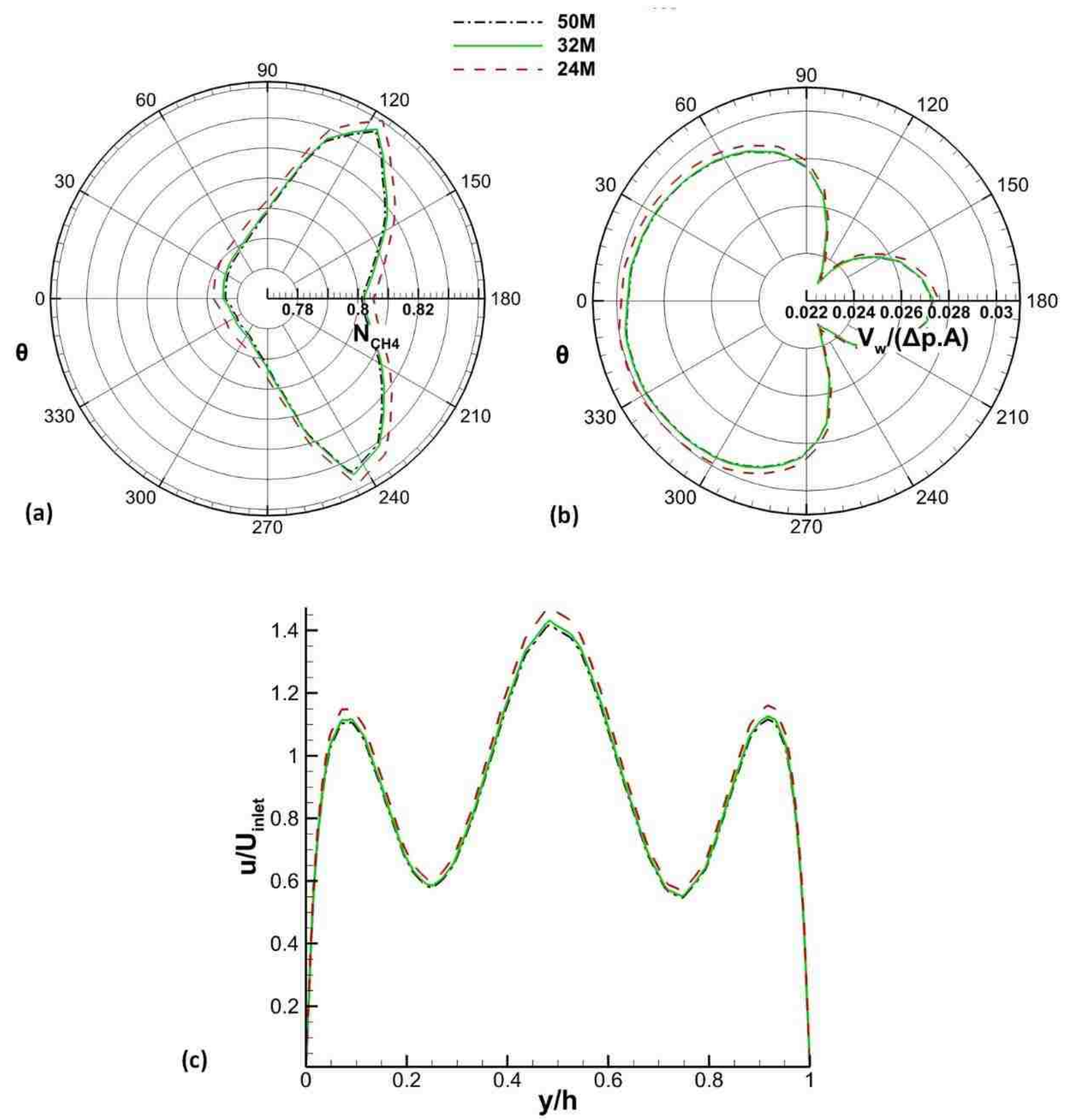

Fig. 13. HFM cross-section profiles at *x=60d* for (a) the molar fraction of CH_4 and (b) the suction rate. Profiles are calculated for the HFM located in the 6th column at the *z=5d* plane. (c) Normalized streamwise velocity component profiles of the HFMB at the *x=65d*. Velocity profiles are normalized by the inlet velocity. Profiles are obtained for varying mesh densities in the inline geometry with *S/d*=10 at *Re*=1000.

4.3. RESULTS

The iso-surfaces of normalized stream-wise velocity component for *Re*= 1000 and *S⁄d*=10 for the inline, the staggered and the net arrangement of HFM are depicted in Fig. 14. The iso-surfaces of $u/U_{inlet}=1$ are depicted. It is shown that the flow structures changes passing first two columns of HFM but becomes periodic after passing the third column of HFM. This indicates that flow becomes spatially periodic and fully developed after passing the third column of HFM. It is also shown that high velocity region is observed in the middle part of the feed channel and in the area around HFMs leading edge and in the intersection region between HFM and bottom membrane surfaces for flows in the inline geometry. Fig. 14b shows that the flow follows a zigzag pattern near the middle region of the channel for the staggered geometry. The presence of high velocity and recirculation regions at different locations throughout the computational domain can be observed in the geometry with the net of HFM, as shown in Fig. 14c. Flow velocity becomes higher away from the inlet in the region behind the backward stagnation point of HFMs surfaces, as depicted in Fig. 14c. The high velocity area extends throughout columns inside the bulk region. It is also noticed that strong three-dimensional effects exist due to the presence of net HFM, this indicates that a higher level of mixing occurs in the net HFMs geometry.

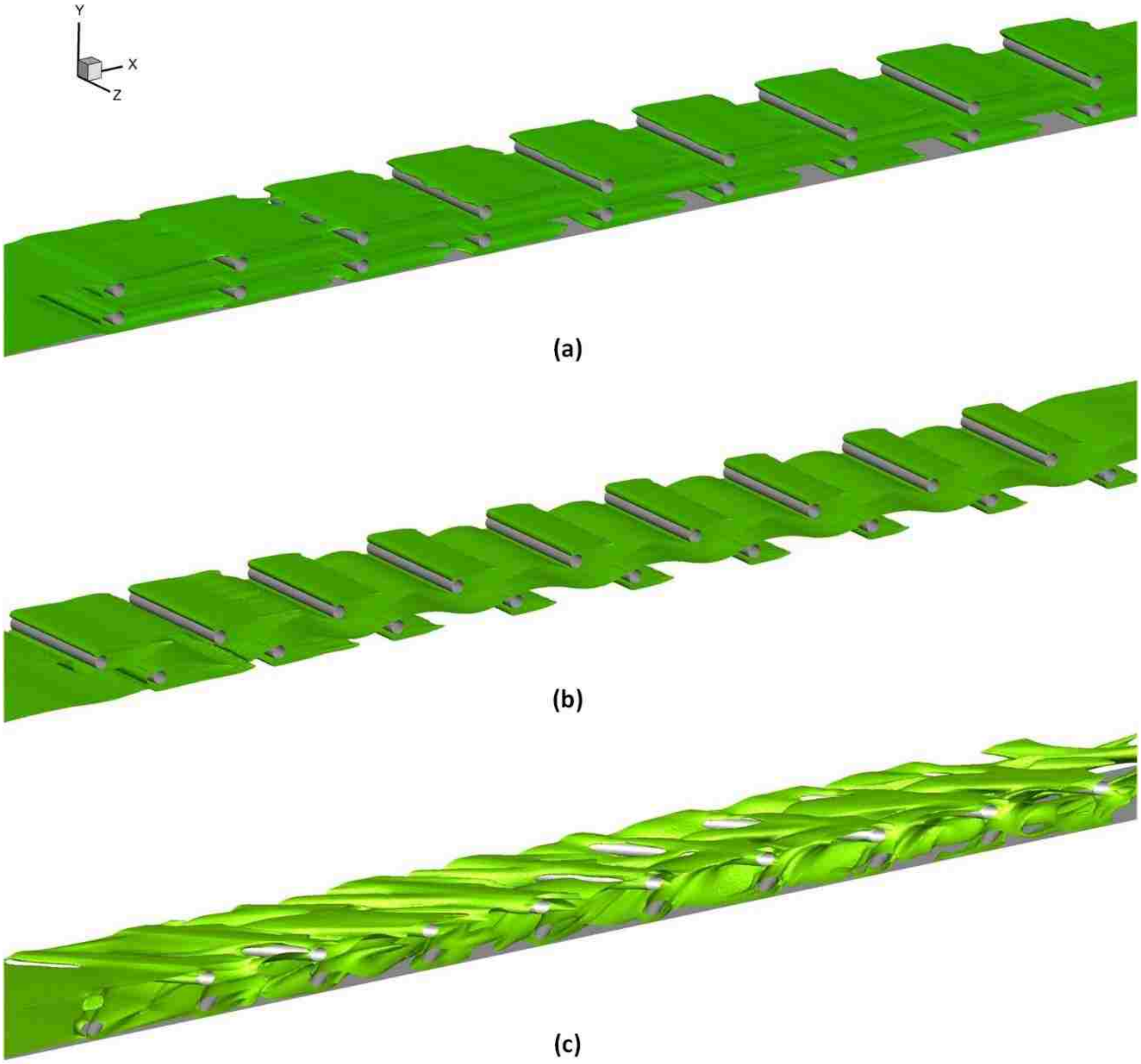

Fig. 14. The iso-surfaces, $u/U_{inlet}=1$, of normalized stream-wise velocity component for *Re*= 1000 at *S/d*=10 for (a) inline geometry (b) staggered geometry and (c) net of HFMs in the 45° arrangement.

The iso-surfaces of the y component of the vorticity in the inline, staggered and net geometry are shown in Fig. 15 for *Re*=1000 and *S/d*=10. Low level of vorticity is observed inside the flow domain for the inline and staggered geometry compared to that in the net geometry. Repeated flow patterns are observed passing the third row of HFM. In the inline and staggered geometry, vortical activities are mostly limited to the region near the vicinity of HFM's. However, in the net type of geometry high level of vortical activities occupy the entire feed channel that implies that the net arrangement of HFMs promotes a significantly higher level of mixing in the entire feed channel; see Fig. 15. It is expected that the presence of the net HFM inside the feed channel improves the membrane performance and can be more suitable for the hybrid gas separation modules.

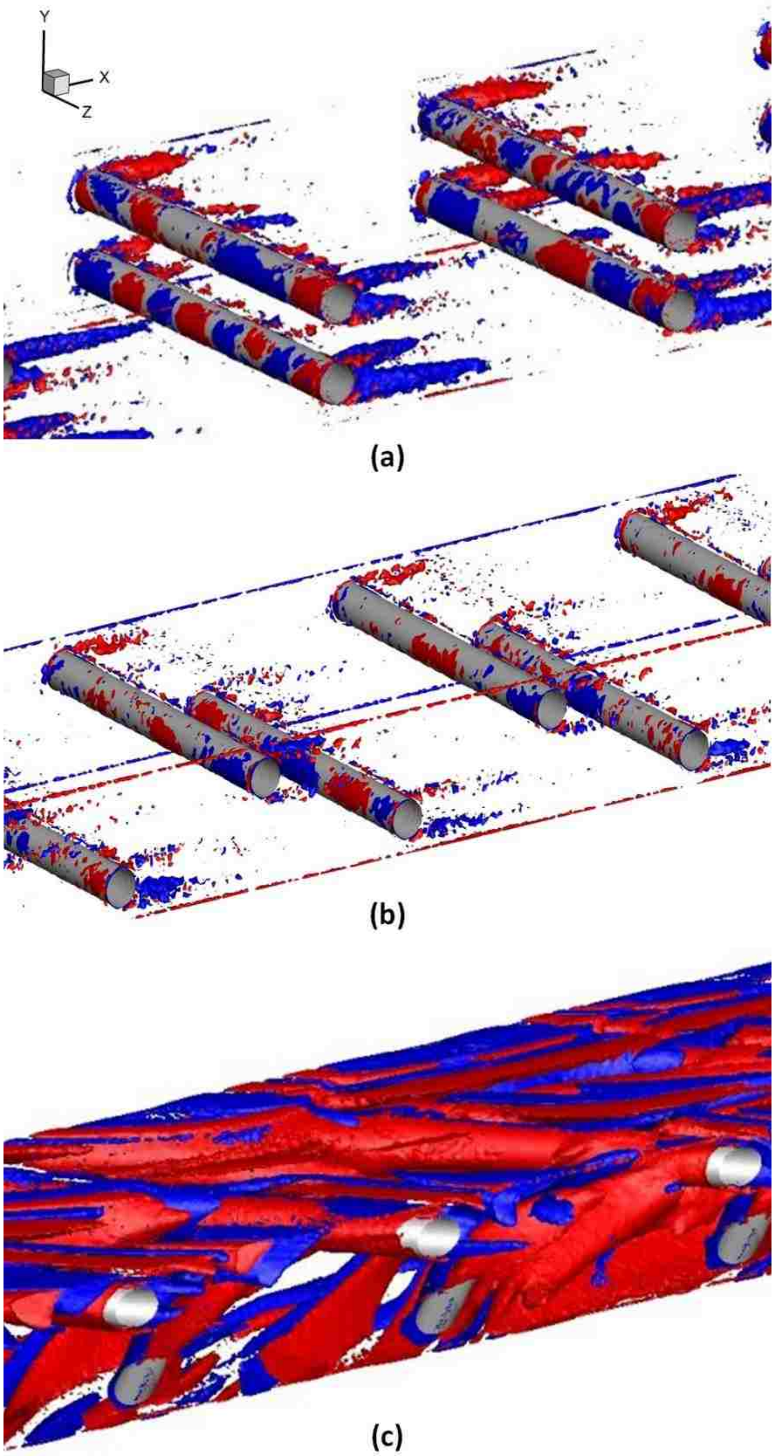

Fig. 15. Iso-surfaces of the y component of the vorticity for *Re*=1000 and *S/d*=10 (a) in the inline, (b) in the staggered: (c) in the net geometry. Vorticity is normalized by *d/U_{inlet}*. The iso-surfaces of -0.21 is indicated in blue and 0.21 is indicated in red. Images are rendered for the HFM located in the 7th and 8th columns.

Fig. 16 and Fig. 17 illustrates iso-surfaces of the Q-criterion (Q=0.02) and mole fraction of CH4 (N_{CH4}=0.76) for Re= 1000 and S/d=10 in the inline, staggered and net geometry. The Q-criterion and the mole fraction iso-surfaces are rendered in the region near the HFM located in the 7th column. There is vortex shedding behind each HFM and the flow separates and the boundary layer detaches from the HFM surface near the backward stagnation point in the inline and staggered geometry, as shown in Fig. 16a, and b. Similar patterns are observed in the iso-surfaces of the mole fraction around each HFM, as illustrated in Fig. 17a, and b. It is abundantly clear that the net arrangement of HFMs shows a profoundly higher level of mixing around HFM and in the bulk flow of feed channel, as shown in Fig. 16c and Fig 17c. This is attributed to the mixing induced by the vortical activities. The vorticity field illustrates that momentum mixing in the feed channel significantly improved by the presence of the net HFM. The presence of high levels of mixing activities and strong three-dimensional effects varies significantly in z-direction implies that the net geometry performs much better along the HFM surface and in the bulk flow compared to the inline and staggered geometry.

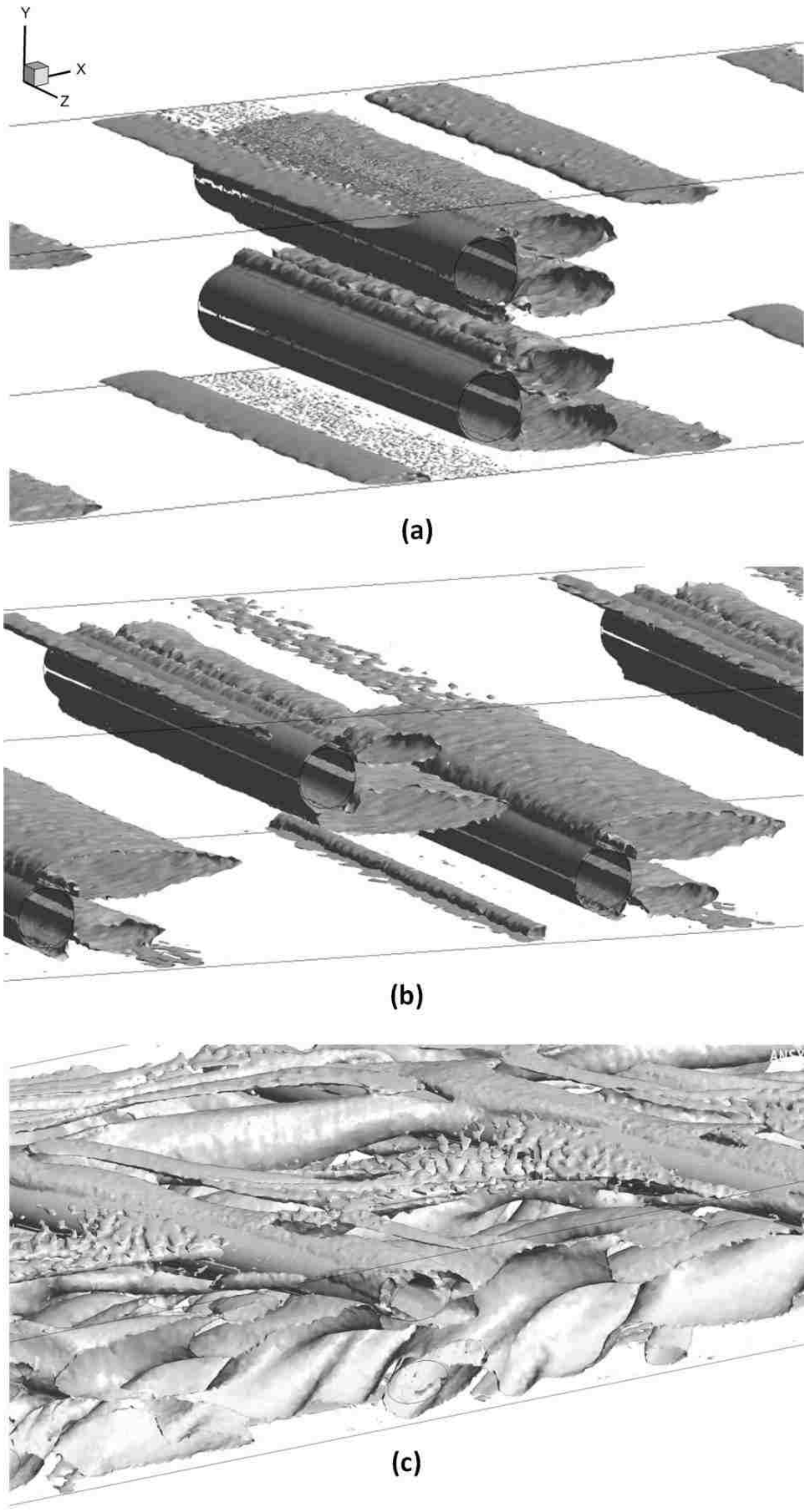

Fig. 16. The *Q*-criterion (*Q*=0.02) for (a) inline (b) staggered and (c) net geometry. Images are rendered for the HFM located in the 7th column at *Re*= 1000 and *S/d*=10.

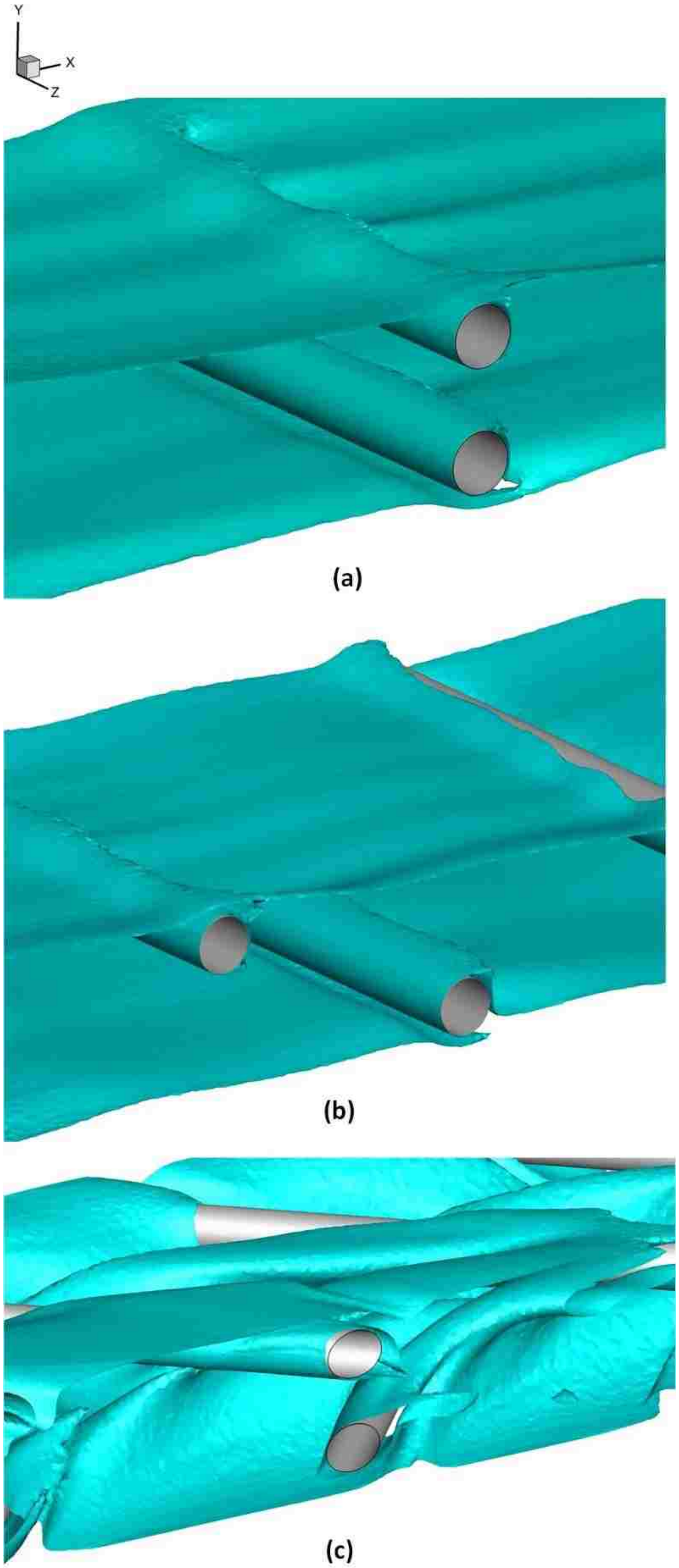

Fig. 17. Iso-surfaces of the mole fraction (N_{CH4}=0.76) for (a) inline (b) staggered and (c) net geometry. Images are rendered for the HFM located in the 7th column at *Re*= 1000 and *S/d*=10.

The contours of the CH_4 mole fraction at $S/d=10$ and $Re=1000$ in the inline, staggered and net geometry of HFMs are illustrated in Fig. 18. The inline geometry shows that the fluid becomes increasingly rich in CH_4 in the bulk region around the narrow space between hollow fiber membrane rows. The staggered geometry shows high concentration in the area near the top and the bottom membrane surface. In the net hollow fiber membranes geometry, the formation of the concentration boundary layer at the membrane surface is influenced by the high velocity flows and the high level of vortical activities near HFMs. The flow structures induced by net HFMs have strong influence on the concentration field, as shown in Fig. 18c. The net geometry shows that the fluid becomes increasingly richer in CH_4 than the inline geometry in the bulk region. The mixing, caused by the net HFM, influences the distribution of the concentration in the wake region. The net hollow fiber membrane helps the mixture to become gradually CH_4 rich away from the inlet and close to the outlet in the net geometry. All geometries exhibit significantly low concentration polarization along HFM surface. This demonstrates that concentration boundary layer disruption induced by HFM in the feed channel in the all geometries successfully mitigates concentration polarization. These results confirm the importance and effective design of the hybrid membrane system to enhance membrane performance.

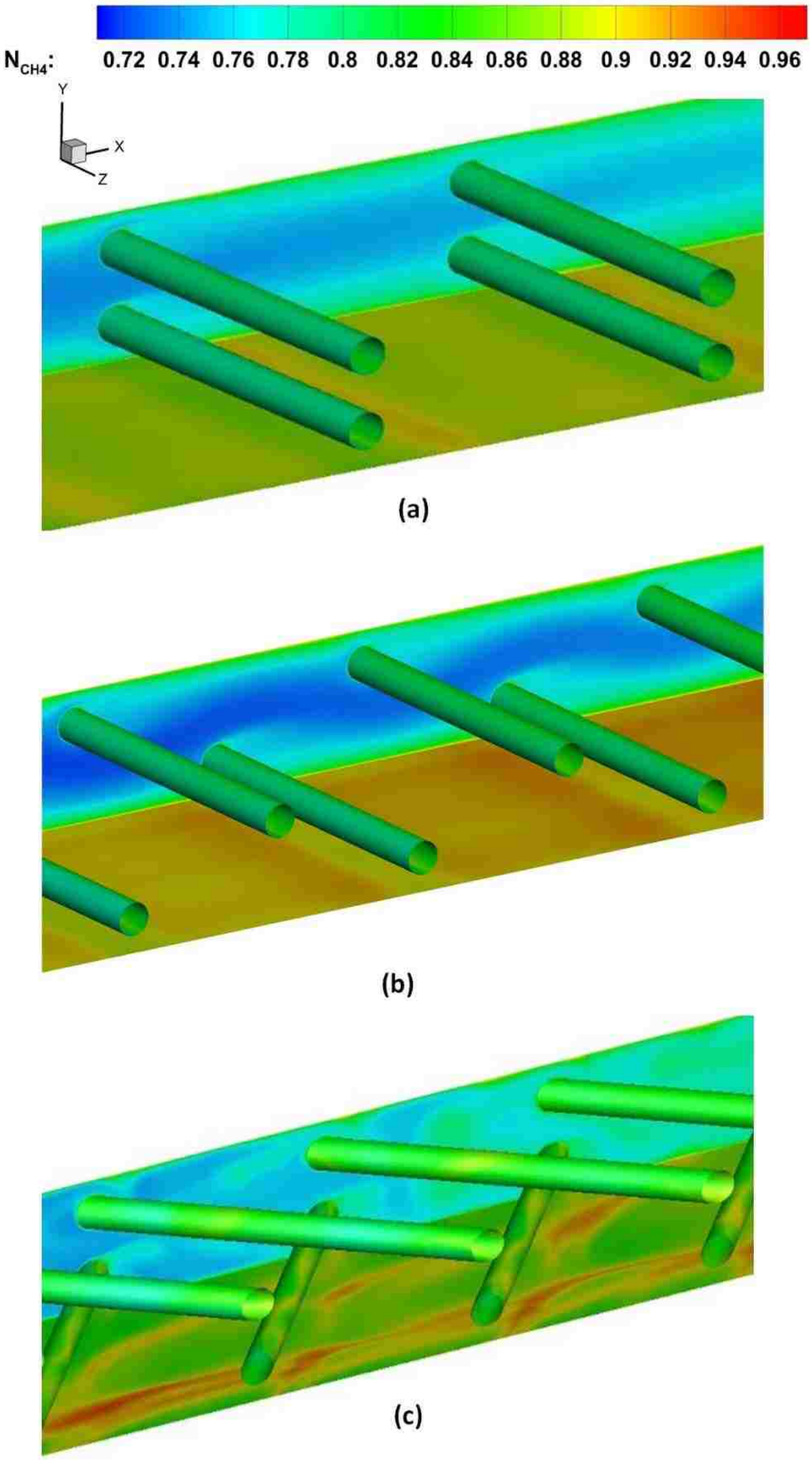

Fig. 18. CH_4 **mole fraction contours at** S/d**=10 and** Re**=1000 in (a) the inline geometry, (b) the staggered, and (c) the net geometry. Images are rendered for the HFM located in the 7th and 8th columns.**

Fig. 19 shows the normalized suction rate at S/d = 10 and Re=1000 for a hybrid module that is containing the inline, staggered, net arrangement of HFMs. The inline geometry has a higher suction rate compared to the staggered geometry through the membrane. The influence of the net arrangement of HFMs on the mass flux across the membrane is more pronounced than both inline and staggered geometry at the higher flow rates. It is also clearly noticed that the influence of net HFM on the mass flux along the membrane is more profound in the regions away from the inlet.

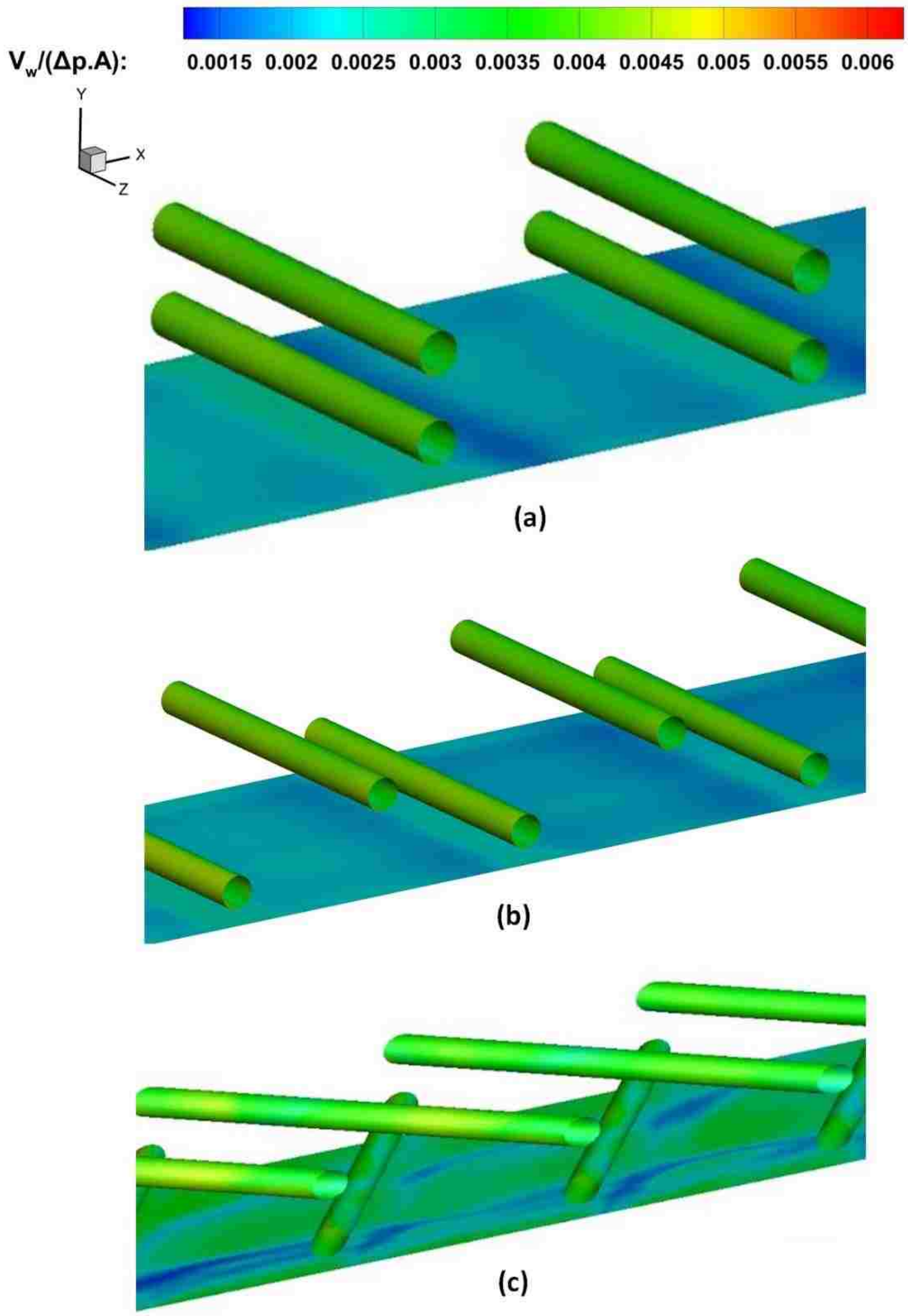

Fig. 19. Normalized suction rate at *S/d=10* and *Re*=1000 in (a) the inline geometry, (b) the staggered, and (c) the net geometry. The suction rate is normalized by *Δp.A*. Images are rendered for the HFM located in the 7th and 8th columns.

Since the feed channel of membrane module consists of only nine hollow fiber membrane columns, the local Sh of the first to the sixth, and last HFM columns would differ from the remaining hollow fiber membranes illustrating that the choice of these columns for Sherwood number prediction would not be good to represent the entire hybrid membrane module. Therefore, we determine the Sherwood number of HFMs at the seventh and eighth columns of the module to determine the mass fux performance of the separation system. Comparisons of the coefficient of performance of different designs of the hybrid hollow fiber and spiral wound membrane module are performed.

Table 5 illustrates the average Sherwood number, $\overline{Sh}$, of HFMs for each arrangement at values of Reynolds number of 400, 700 and 1000 and for *S/d=10*. The average value of the Sherwood number is determined using hollow fiber membranes at the seventh and the eighth column. Table 5 shows also the pressure drop in each geometry. The level of pressure drop is significantly higher compared to both the staggered and the net geometry at all flow rates. The friction factor is nearly the same for all flow rates in each geometry. It is also noted that the similar level of pressure drop in staggered and the net geometry, as listed in Table 5. The Sherwood number increases with increasing Reynolds numbers in each geometry.

Re	**Average Sherwood Number –** $\overline{\text{Sh}}$			**Friction Factor –** fr			**Coefficient of Performance – COP**	
	45 degree	***Inline***	***Staggered***	***45 degree***	***Inline***	***Staggered***	$\frac{Sh_{45}/Sh_i}{(fr_{45}/fr_i)^{1/3}}$	$\frac{Sh_{45}/Sh_s}{(fr_{45}/fr_s)^{1/3}}$
400	16.29	14.96	11.44	0.014	0.044	0.013	1.595	1.443
700	23.50	20.99	16.52	0.013	0.043	0.013	1.668	1.422
1000	30.14	25.95	20.57	0.011	0.042	0.011	1.815	1.465

Table 5. The averaged Sherwood number, the friction factor across the hollow fiber membrane and the coefficient of performance for the different geometries at $S/d = 10$ and various values of Re.

Table 6 shows the average Sherwood number, $\overline{Sh}$, averaged along the surface of the spiral wound membrane in the net, inline and staggered geometry at various values of Re for $S/d = 10$. The Sherwood number increases as Reynolds numbers increase in each geometry. Coefficient of performance is calculated as:

$$COP = \frac{Sh_{45}/Sh_i}{(fr_{45}/fr_i)^{1/3}} \tag{26}$$

and

$$COP = \frac{Sh_{45}/Sh_s}{(fr_{45}/fr_s)^{1/3}} \tag{27}$$

Here Sh_{45}, Sh_i, and $Sh_s$are the average Sherwood numbers for all HFMs in the net , inline and staggered geometries, respectively. fr_{45}, fr_i, and $fr_s$are the friction factors for the net, inline, and staggered HFMB geometry at *S/d=10*, respectively. Coefficient of performance compares the module with net arrangement of HFM against those with the cross flow inline and staggered arrangement of HFM, For all cases considered, the coefficient of performance is greater than unity. That indicates that the mass flux performance of hybrid separation unit is better with the design of the net arrangement of HFMs.

Re	**Average Sherwood Number – $\overline{\text{Sh}}$**			**Friction Factor – fr**			**Coefficient of Performance – COP**	
	45 degree	***Inline***	***Staggered***	***45 degree***	***Inline***	***Staggered***	$\frac{Sh_{45}/Sh_i}{(fr_{45}/fr_i)^{1/3}}$	$\frac{Sh_{45}/Sh_s}{(fr_{45}/fr_s)^{1/3}}$
400	12.16	9.04	9.01	0.014	0.044	0.013	1.970	1.316
700	15.45	13.64	12.28	0.013	0.043	0.013	1.687	1.258
1000	20.28	17.60	16.43	0.011	0.042	0.011	1.800	1.234

Table 6. The average Sherwood number, the average friction factor across the spiral wound membrane and the coefficient of performance for the different geometries at $S/d = 10$ and various values of Re.

Another way to measure the HFM performance is by calculating the mass flow rate of CO_2 per unit area permeating through the membrane surface. Table 7 depicts the values of the mass flow rate of CO_2 per unit area diffusing through the membrane surface for the net, inline, and staggered arrangement for various values of Re and $S/d = 10$. Table 7 confirms the net geometry yields the greater mass flow rate of CO_2. Examination of the average Sherwood number, coefficient of performance, and mass flow rate confirm that HFMs arranged in the net geometry facilitate the greatest separation module performance as compared to the inline and staggered geometry. Further, these results emphasize the importance of considering net hybrid HFM configuration in separation module design and optimization.

Re	**Mass Flow Rate** – $\dot{m}$		
	45 degree	***Inline***	***Staggered***
400	0.0523	0.0506	0.0518
700	0.0654	0.0638	0.0636
1000	0.0744	0.0726	0.0719

Table 7. CO_2 mass flow rate per unit area across membranes surface for the net 45 arrangement, inline, and staggered arrangements at various values of *Re* and *S/d=10*.

The influence of hollow fiber membrane spacing on flow and mass transfer in the feed channels has been investigated for *S/d=2.5*. There is a strong correlation between the normalized stream-wise velocity component, the normalized y vorticity component, the *Q*-criterion (*Q*=0.02), and the mole fraction iso-surfaces (N_{CH4}=0.76), as shown in Fig. 20 and Fig. 21 for *Re*= 1000 and *S/d*=2.5 in the net geometry. It can be noted that the size of recirculation regions is smaller when compared to the *S/d=10*. For tighter spacing *(S/d=2.5*), the effect of three-dimensional structure is less and local enhancement is not as much as the wider spacing *(S/d=10)*.

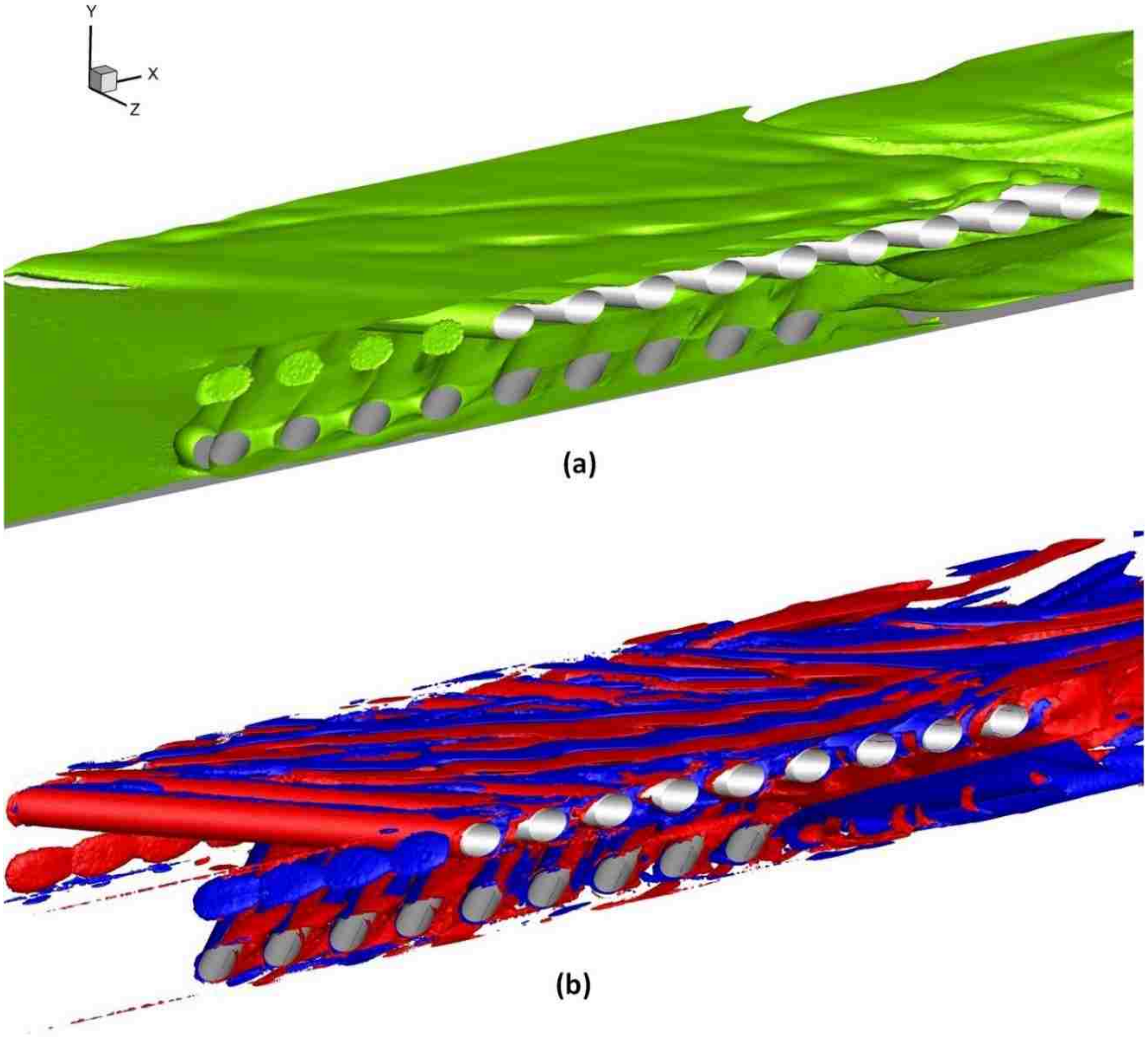

Fig. 20. Images of (a) the iso-surfaces, $u/U_{inlet}=1$, of the normalized stream-wise velocity component, and (b) the iso-surfaces of the y component of the vorticity for Re= 1000 at S/d=2.5 for net of HFMs in the 45° arrangement. Vorticity is normalized by d/U_{inlet}. The iso-surfaces of -0.21 is indicated in blue and 0.21 is indicated in red.

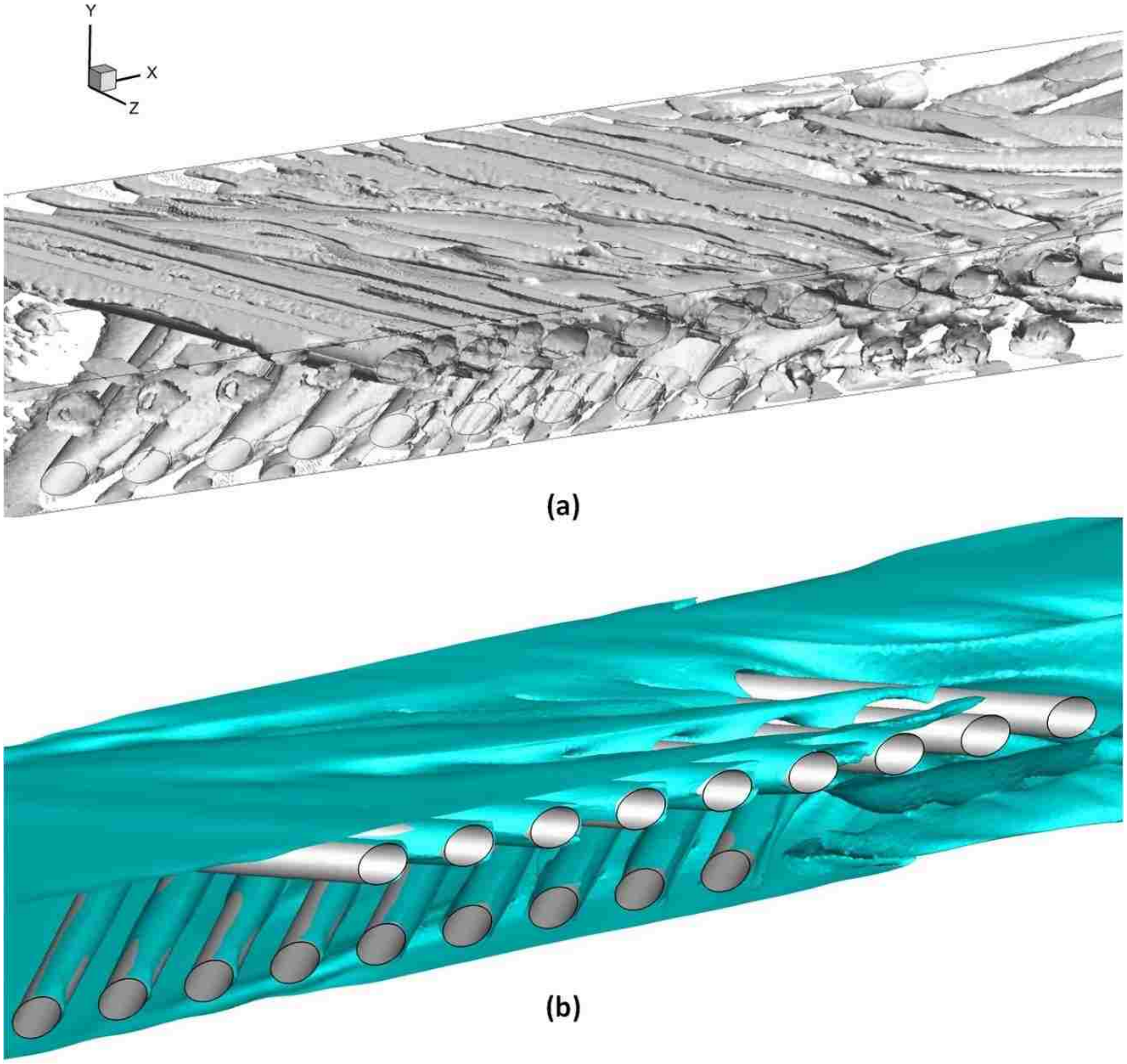

Fig. 21. Images of (a) the *Q*-criterion (*Q*=0.02), and (b) iso-surfaces of the mole fraction (N_{CH4}=0.76) for *Re*= 1000 at *S/d*=2.5 for the net type of HFMs in the 45° arrangement.

The contours of CH_4 mole fraction and the normalized suction rate on the hollow fiber membranes and the bottom spiral wound membrane for *S/d*=2.5 and *Re*=1000 are shown in Fig. 22 and Fig. 23, respectively. It is noticed that the level of concentration enhancement in the bulk region less compared to that in a wider spacing (*S/d=10*) geometry. The comparison of two spacing shows that the mole fraction and the suction rate are higher for spacing (*S/d=10*). Hence, the wider spacing (*S/d=10*) is a more favorable design for the hybrid modules.

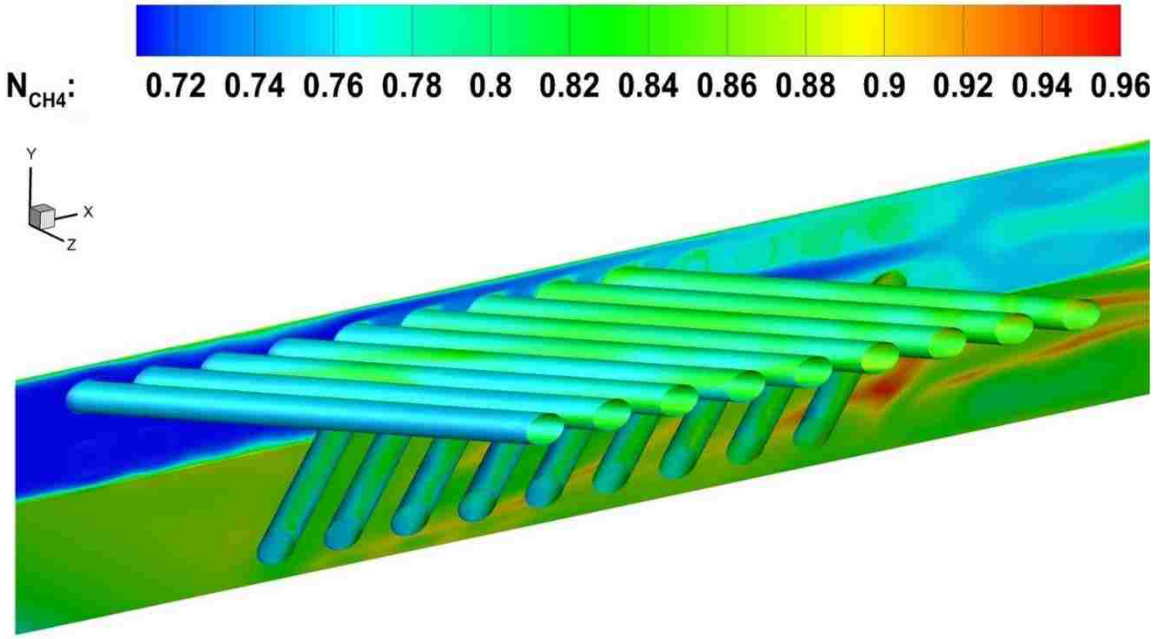

Fig. 22. CH_4 mole fraction concentration contours at *S/d*=2.5 for: *Re*=1000 in the net HFMs.

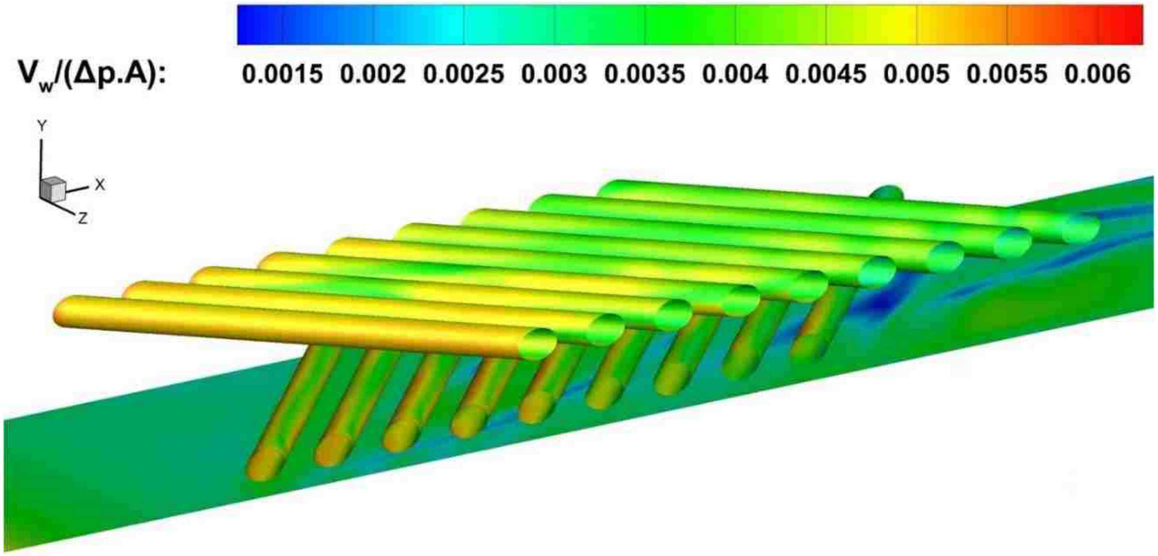

Fig. 23. Normalized suction rate contours at *S/d*=2.5 for *Re*=1000 in the net HFMs. The suction rate is normalized by the pressure difference across the membrane times the permeability, *Δp.A*.

Table 8 shows the averaged Sherwood number, the averaged friction factor across the spiral wound membrane and the coefficient of performance for $S/d = 2.5$ and $Re = 1000$. Coefficient of performance is calculated as:

$$COP = \frac{Sh_{45}/Sh_{45t}}{(fr_{45}/fr_{45t})^{1/3}} \tag{28}$$

Here Sh_{45t} is the average Sherwood numbers and fr_{45t} is the friction factors for the net HFMB geometry at $S/d = 2.5$ (tight spacing). Sh_{45} is the average Sherwood numbers and fr_{45} is the friction factors for the net HFMB geometry at $S/d = 10$. The coefficient of performance is greater than unity which indicate that wider spacing, *S/d*=10, is more effective for the net geometry.

Re	***45 degree***		**Coefficient of Performance – COP**
	Average Sherwood Number – $\overline{\mathrm{Sh}}$	**Friction Factor –** fr	$\frac{Sh_{45}/Sh_{45t}}{(fr_{45}/fr_{45t})^{1/3}}$
1000	17.19	0.018	1.390

Table 8. The average Sherwood number, the average friction factor across the spiral wound membrane and the coefficient of performance for the net 45 arrangement at $S/d = 2.5$ and $Re = 1000$.

Table 9 shows the averaged Sherwood number, the averaged friction factor across the hollow fiber membrane and the coefficient of performance for $S/d = 2.5$ and $Re = 1000$ in the net geometry. The coefficient of performance is greater than unity which indicate that wider spacing *(S/d=10*) is also more effective in a net hollow fiber membrane geometry.

Re	***45 degree***		**Coefficient of Performance – COP**
	Average Sherwood Number – $\overline{\mathrm{Sh}}$	**Friction Factor –** fr	$\frac{Sh_{45}/Sh_{45t}}{(fr_{45}/fr_{45t})^{1/3}}$
1000	26.59	0.018	1.428

Table 9. The average Sherwood number, the average friction factor across the hollow fiber membrane and the coefficient of performance for the net 45 arrangement at $S/d = 2.5$ and $Re = 1000$.

Table 10 illustrates the mass flow rate of CO_2 per unit area permeating through the membrane surface for the net arrangement for $Re = 1000$ and $S/d = 2.5$. Hybrid module with tighter HFM spacing in the net geometry yields a lower mass flow rate than that for *S/d=10*. Furthermore, these outcomes emphasize the necessity of including net hybrid HFM with wider spacing ratio configuration in separation module design.

Re	**Mass Flow Rate** – $\dot{m}$
	45 degree
1000	0.0543

Table 10. CO_2 mass flow rate per unit area across membranes surface for the net 45 arrangement at $Re = 1000$ and *S/d=2.5*.

4.4. CONCLUSION

CFD simulations have been conducted to characterize the effect of arrangement and spacing in hybrid separation module containing hollow fiber and spiral wound membranes. Modules consist of arrays of hollow fiber membranes in a feed channel bounded by two parallel spiral wound membranes. The literature in the area of heat transfer show that the spacers enhance the momentum mixing and heat transfer. This study replaces spacers with hollow fiber membranes in the feed channel. The objectives of utilizing hollow fiber membranes are to enhance momentum mixing in the feed channel and to increase the rate of mass flow of CO_2 passing across the hybrid membrane surface. The feed channel consists of three different arrangements of hollow fiber membranes: an inline, a staggered and a cross-linked membrane (45 degrees) with the spacing S/d of 10 and 2.5. The separation module design studied for the Reynolds number from 400 to 1000 using a k-ω Shear Stress Transport (k-ω SST) turbulence model. The primary flow is parallel flow to the spiral wound membranes and perpendicular to the hollow fiber membrane axes in the feed channel; this study is the first in implementing membrane flux boundary conditions in hybrid membrane geometry to study reverse osmosis process of gas separation. The results show that three-dimensional flows generated by the net hollow fiber membranes have profound effects on the membrane performance. The iso-surfaces of normalized stream-wise velocity component, the y-component of vorticity, the Q-criterion, and mole fraction iso-surfaces clearly illustrate that higher momentum mixing achieved with the net hollow fiber membranes arrangement improves membranes performance. The mixing, caused by the net HFM, influences the distribution of the concentration. The net arrangement helps the mixture becomes CH_4 richer than inline and staggered geometries. Moreover, the net HFM show higher mass flux through the module compared to the inline and staggered geometries. This work illustrates that the hybrid system with a net hollow fiber membrane arrangement could be an effective way of designing gas separation modules. Hybrid separation module outperforms modules with only spiral wound membranes and modules with only hollow fiber membranes.

CHAPTER 5: TWO DIMENSIONAL FLOWS CROSS FLOW ARRANGEMENT- DESALINATION

5.1. GEOMETRY

The schematic of the feed channel containing an array of hollow fiber membranes is shown in Fig. 24 Hollow fiber membranes are arranged with an inline (see Fig. 24a) and with staggered (see Fig. 24b) geometry. Dimensions of the computational domain consisting of the bank of hollow fibers, the inlet, and the outlet are illustrated in Fig. 24. The hydraulic diameter is d, the length of the membrane module is $L = 44d$, and the spacing between two consecutive hollow fiber membrane is S. The inline and staggered arrangement of the hollow fiber banks with the spacing S/d of 1.5 and 2 are considered. The height of the hollow fiber bundle, H, is $4.5d$ for banks with $S/d = 1.5$ and is $6d$ for banks with $S/d = 2$. The distance $8d$ is assigned between the inlet and the bank of hollow fiber membrane. The distance between the outlet and the hollow fiber membrane bank is $24d$ for $S/d = 1.5$ and $30.5d$ for $S/d = 2$. The inlet and outlet region is long enough to assure that the inlet and outlet conditions have minimal effect on the velocity and the concentration field in the bank of the hollow fiber membranes. Steady state simulations are conducted for values of the Reynolds number up to 1000 in both inline and staggered geometry.

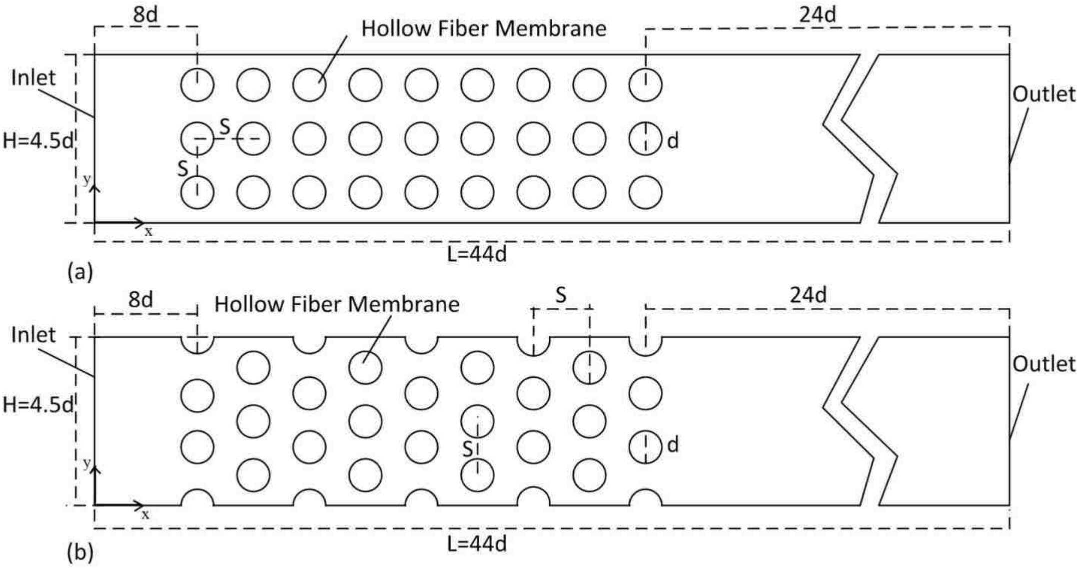

Fig. 24. The schematic of flow domain: (a) the inline geometry and (b) the staggered geometry for $S/d = 1.5$. Dimensions of the inlet region, the outlet region and the bank of the hollow fiber membranes are illustrated.

5.2. MESH STUDY

A mesh optimization study is conducted using three mesh sizes: 4, 6 and 8 million elements for SST model and 1.8, 2.8 and 4 million lattices for LES-LBM model. Profiles of the normalized stream-wise component of velocity, obtained for various meshes, are plotted in Fig. 25. Profiles are acquired at $x/d = 18$ for $Re = 100$ in the staggered geometry with $S/d = 2$. Reynolds number is defined as $Re = U_{in}d/\nu$, where U_{in} is the average fluid velocity at the inlet and d is the hydraulic diameter. Velocity profiles predicted by SST turbulence model using all three meshes are nearly the same; implying that 4 million-element mesh is sufficient to ensure spatial convergence for steady SST simulations. Similarly, time averaged velocity profiles predicted by LES-LBM using 2.8 million and 4 million lattices are nearly the same, as shown in Fig. 25b. This suggests that 2.8 million lattices are sufficient to provide reasonably accurate solution with LES-LBM method. SST results presented in this study are obtained using 4 million elements while

LES-LBM results are obtained using 2.8 million lattices. The time step is selected to be 5.6 x 10^{-7} second to attain temporal convergence for LES-LBM simulations.

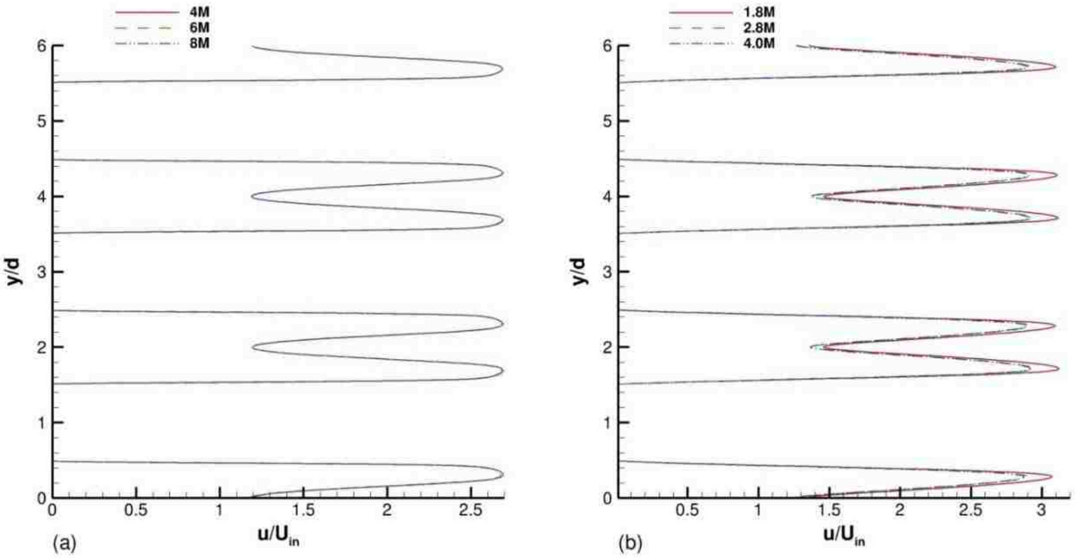

Fig. 25. Profiles of the stream-wise component of the velocity calculated using three mesh size using (a) SST and (b) LES-LBM model in the staggered geometry with $S/d = 2$ at $Re = 1000$.

5.3. TRANSIENT FLOWS

Lattice Boltzmann method (LBM) is relatively new and innovative method that employs kinetic theory to simulate fluid flows [48]. The method is essentially equivalent to a direct numerical solution (DNS). The discretized equations by the lattice Boltzmann method can easily be parallelized; that makes the method to be an effective computational tool. The method is very versatile and it can be used to simulate complex flow systems [49]. The present study employs LBM to study two-dimensional transient flows in a channel containing arrays of impermeable cylinders. The objectives of utilizing lattice Boltzmann method are two folds: (1) to validate the turbulence model employed here and (2) to characterize temporal characteristics of the flow inside the hollow fiber bank.

The commercial software, CFX 14.5, is employed to conduct the numerical simulations. This software implements the finite volume discretization method. The solver that fully couples the velocity and pressure field is applied. The CEL expression language is deployed to implement the boundary conditions at the inlet and along the surface of the membrane.

Results presented in this section are obtained for surfaces that are impermeable so that there is no water permeation through the membrane. It is also important to note that only flow field is simulated in this section to determine the transient characteristics of the flow. Profiles of the stream-wise component of the velocity obtained by LES-LBM and SST turbulence models are depicted in Fig. 26 in the inline and the staggered geometry at $Re = 100$ and 1000. Detailed description of the LES-LBM method is provided in Ref [33]. Velocity profiles normalized by the inlet velocity are attained at $x/d = 14$ in both geometries with S/d of 1.5. Time-averaged velocity profiles predicted by LES-LBM match reasonably well with those predicted by steady SST simulations at $Re = 100$. Slight deviations between these profiles are observed in the high speed regions of both geometries. Deviation between time-averaged and steady profiles increases as Re is increased to 1000, as shown in Fig. 26. The overall spatial characteristics of the time-averaged velocity profiles predicted by transient and steady state simulations are similar. The velocity profiles presented in Fig. 26 clearly indicate that flow field inside the hollow fiber bank is transient in nature, especially at high flow rates.

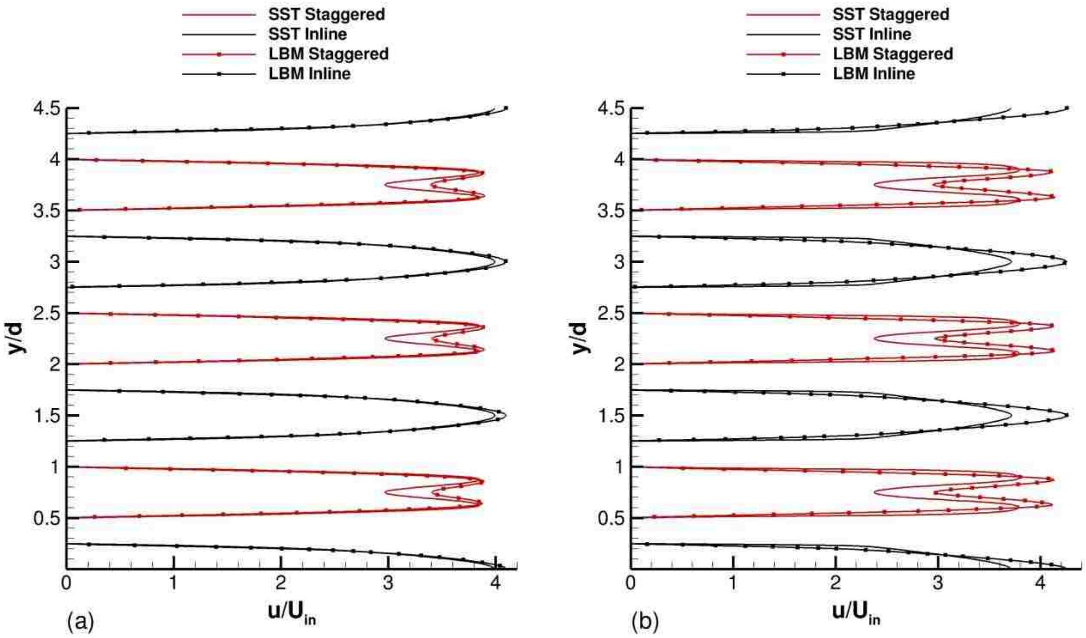

Fig. 26. Profiles of the stream-wise component velocity predicted by steady SST turbulence model and LES-LBM model in the inline and the staggered geometry with $S/d = 1.5$. Profiles are obtained at $x/d = 14$ at (a) $Re = 100$ and at (b) $Re = 1000$.

Contours of the stream-wise component of the velocity in the bank of hollow fiber membranes are shown in Fig. 27 for the inline and the staggered geometry with $S/d = 1.5$ at $Re = 100$ and 1000. Images on the left column denote velocity contours in the inline geometry while images on the right column denotes velocity contours in the staggered geometry. Images at top two rows are contours obtained at $Re = 100$ while images at the bottom two rows are contours obtained at $Re = 1000$. The time-averaged velocity field predicted by LES-LBM is very similar to the steady state velocity field predicted by SST model. As illustrated above by velocity profiles (see Fig. 26) there are minor differences between the transient and steady velocity field in the high speed regions in both geometry. This demonstrates that SST turbulence model characterizes the flow field reasonably well in the hollow fiber bank region. The velocity field in the hollow fiber bank is repeated after each column of hollow fiber membranes after the first column in both geometry. It is noted that there are two distinct flow types in the inline geometry: jet-like flows and wake flows.

Jet-like flows are obtained in the region between rows of hollow fiber membranes and wake flows are obtained in the region behind and front of hollow fiber membranes. In the staggered geometry double layer of jet is observed between cylinders. Jets are interrupted approaching hollow fibers at the successive column. Also seen in the staggered geometry is the distinct flow pattern behind each hollow fiber membrane influenced by flow separations.

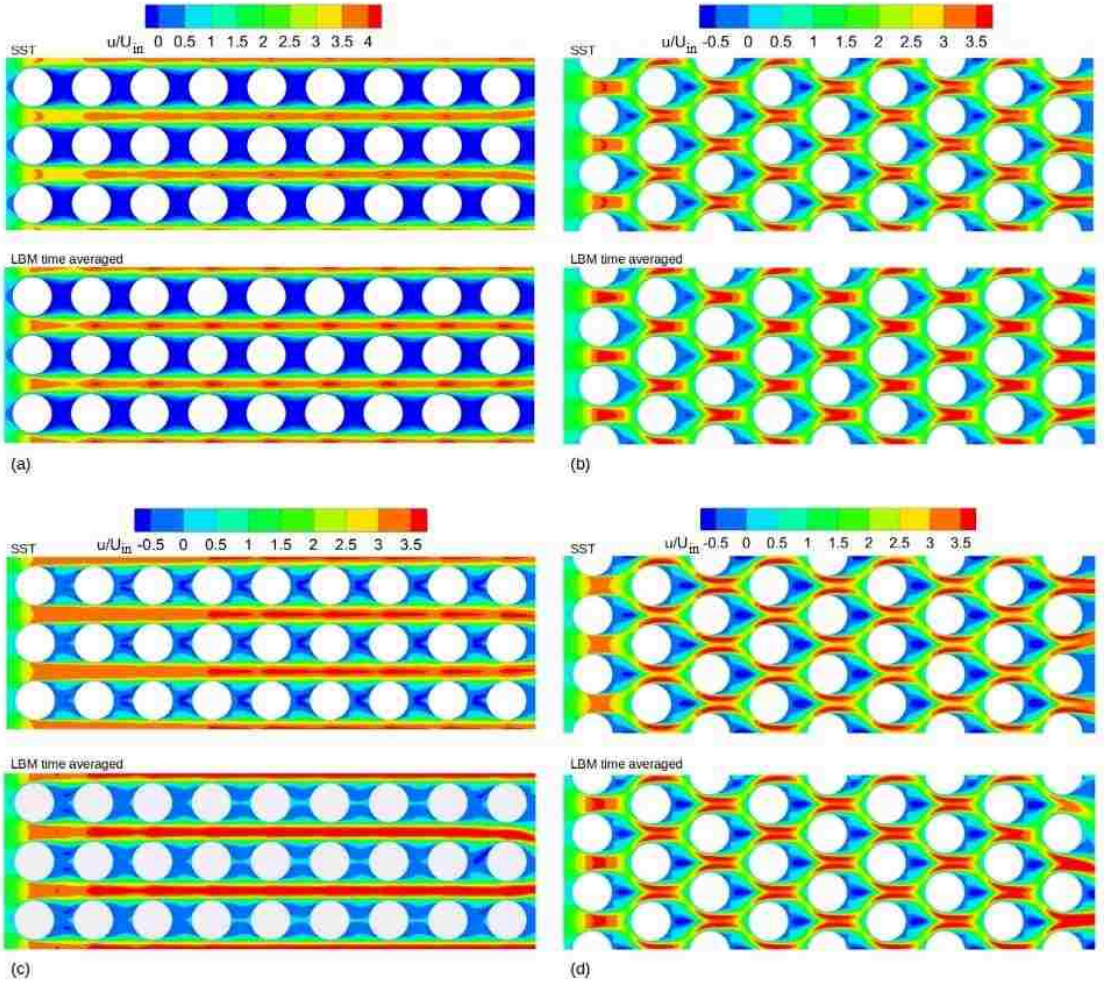

Fig. 27. Contours of the stream-wise component of the velocity predicted by SST and LES-LBM model in the inline geometry (a, c) and in the staggered geometry (b, d). The normalized velocity contours are acquired at $Re = 100$ (a, b) and at $Re = 1000$ (c, d).

Instantaneous drag coefficient is calculated for the hollow fiber membrane located at the 6th column and the middle row for the inline and the staggered geometry with $S/d = 1.5$. The drag coefficient is plotted as a function of time in Fig. 28 for $Re = 100$ and 1000. At $Re = 100$ fluctuations in the drag coefficient is very small in both geometry, as shown in Fig. 28a. On the other hand, at $Re = 1000$ drag coefficient fluctuates with large amplitudes in both geometries, as shown in Fig. 28b. This is a clear indication that the flow inside the tube bank is strongly time dependent. Hence hydrodynamic forces such as drag and lift coefficient, pressure coefficient, wall stress, water permeation, concentration along the surfaces of hollow fiber membranes are expected to depend on time strongly. These properties dictate the performance of the hollow fiber membranes in the desalination module. Drag coefficient predicted by the steady SST simulations is also plotted in Fig. 28. At both feed flow rates the time-averaged value of drag coefficient agrees with the drag coefficient predicted by steady SST simulations. This is another validation of the turbulence model utilized to study membrane performance presented below. Dimensionless time used in Fig. 28 is defined as $\tau = \frac{tU}{d}$.

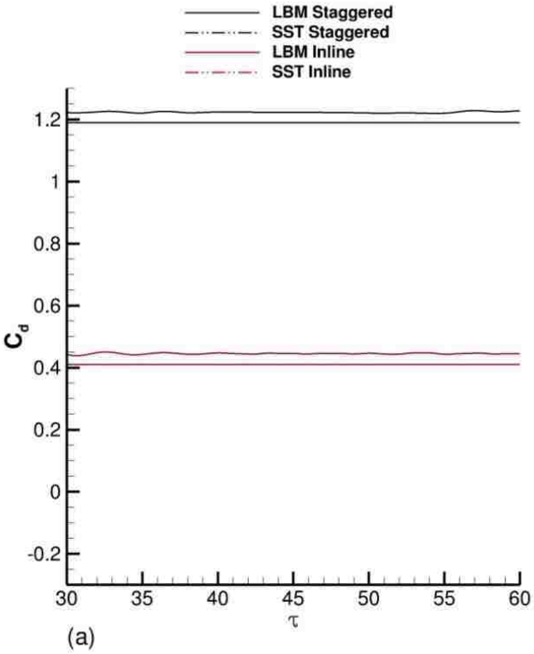

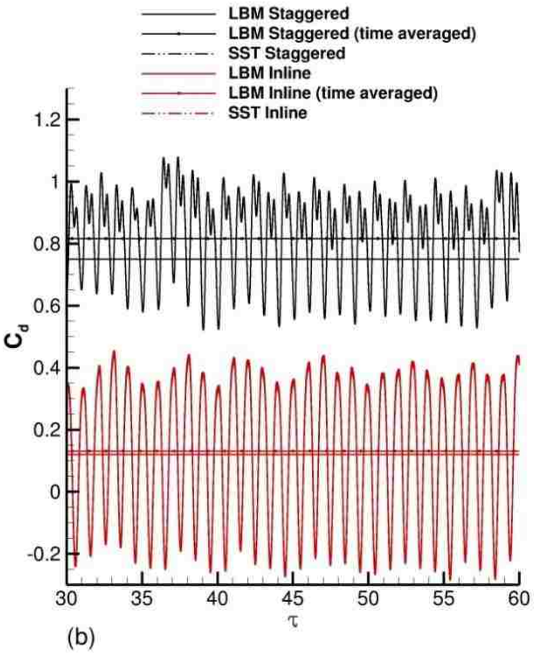

Fig. 28. The drag coefficient predicted by SST and LBM model in the inline and the staggered geometry with $S/d = 2$ at (a) $Re = 100$ and (b) $Re = 1000$. The drag coefficient is calculated for the hollow fiber membrane located on the 6-th column and the middle row.

Instantaneous contours of pressure, stream-wise component of the velocity and y-component of the vorticity are shown in Fig. 29 in the staggered geometry with $S/d = 1.5$ at $Re = 1000$. Contours are shown in two separate instants of a given periodic cycle: at $\tau = 40.41$ when drag coefficient assumes nearly maximum and at $\tau = 40.83$ when drag coefficient assumes nearly minimum. Pressure and flow field show immensely different characteristics at these instants, as shown in Fig. 29. These patterns are repeated in time at each cycle. More importantly flow separation pattern around the hollow fiber membranes varies significantly with time. It is well-documented by the present author and other investigators that characteristics of the concentration polarization are strongly dependent on the separation patterns of the boundary layer [10,12,50]. It is clearly illustrated in Fig. 29 that transient effects are very strong in these flows at high feed flow rates.

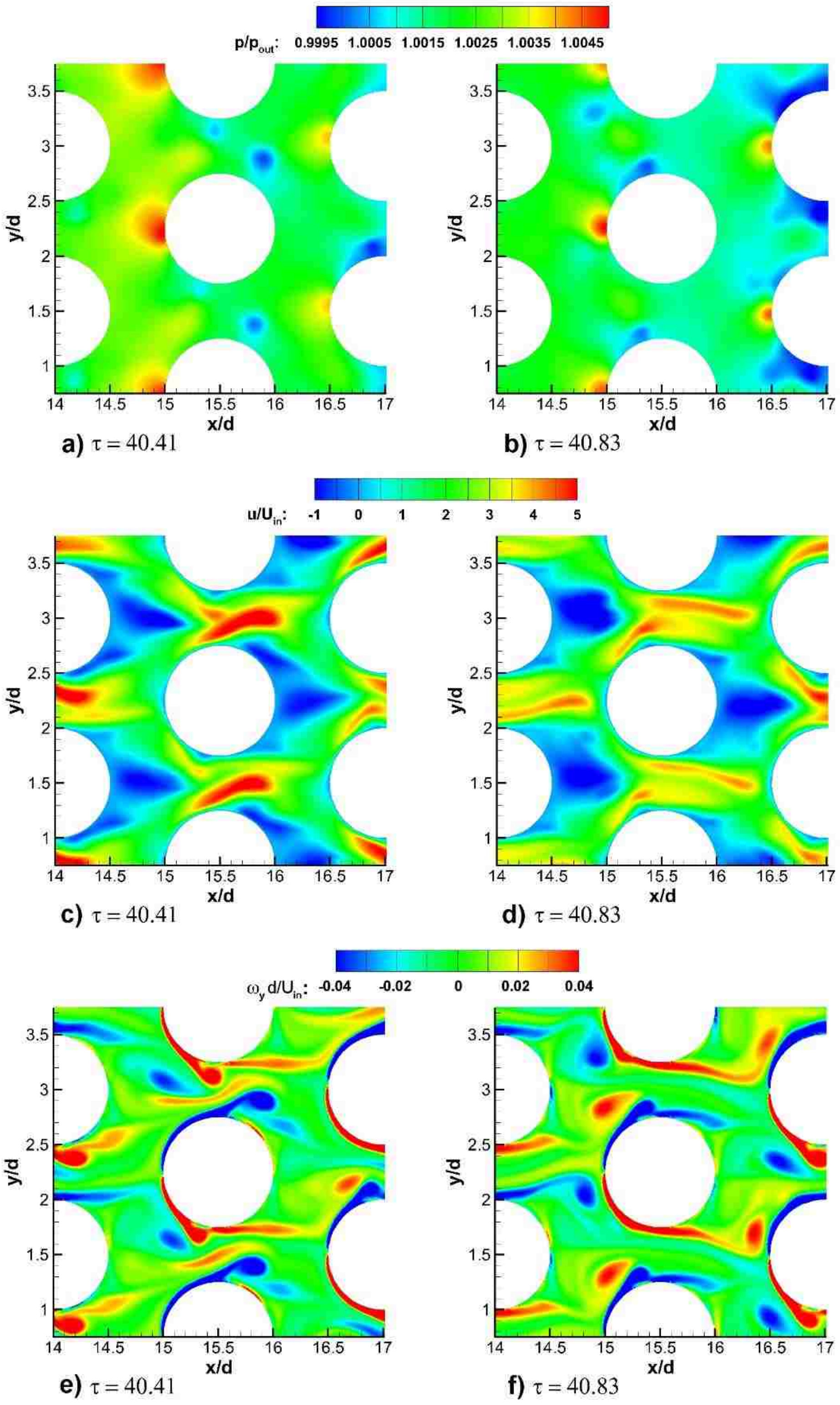

a) $\tau = 40.41$

b) $\tau = 40.83$

c) $\tau = 40.41$

d) $\tau = 40.83$

e) $\tau = 40.41$

f) $\tau = 40.83$

Fig. 29. Instantaneous contours of normalized pressure (a, b), stream-wise component of the velocity (c, d) and y-component of the vorticity (e, f) in the staggered geometry with $S/d = 1.5$ at $Re = 1000$. Images are acquired at $\tau = 40.41$ (a, c, e) and at $\tau = 40.83$ (b, d, f).

5.4. HOLLOW FIBER MEMBRANE PERFORMANCE

Steady-state velocity and concentration field in the hollow fiber bank are simulated using SST turbulence model. The hollow fiber membrane is treated as a functional permeable surface where the rate of water permeates through the membrane is coupled with the local concentration along the surface of the hollow fiber membrane. Simulations are conducted at Re of 100, 200, 300, 500 and 1000 for the inline and the staggered geometry.

Fig. 30 depicts contours of the normalized concentration (C/C_0) at $Re = 100$ and 1000 in the inline and the staggered geometry with $S/d = 1.5$. The distribution of the concentration is very different at these geometries. In the inline geometry near the front stagnation region, there is a high level of concentration polarization while the level of concentration in the region near the forward stagnation point is much lower in the staggered geometry. In the region near the backward stagnation region, however, the level of concentration is higher in both geometries. It is also important to note that the concentration polarization occurs where flow separates and the boundary layer is detached from the surface of the hollow fiber membrane. Fig. 30a and 30c show the contours of the normalized concentration in the whole hollow fiber membrane bank at $Re = 100$ while Fig. 30b and 30d show the enlarged images at around the hollow fiber located at the 6th column and the middle row. Fig. 30e and 30f show contours of the concentration around the same hollow fiber membrane at $Re = 1000$. In each geometry, the concentration polarization is mitigated significantly as the feed flow rate is increased to $Re = 1000$. This is due to the fact that momentum mixing induced by the presence of hollow fiber membrane in the feed channel is enhanced at higher feed flow rates. The level of momentum mixing in the staggered geometry is much higher than that in the inline geometry at all flow rates, as evident from flow images presented above. That in turn results in better polarization mitigation in the staggered geometry compared to the inline geometry at all feed flow rates. It is also important to note that the level of concentration polarization is much smaller in the desalination module containing hollow fiber membrane banks than that in the desalination module containing spiral wound membranes [10,12,50]. The level of concentration polarization and its distribution along the surface of the membrane is very important in the overall performance of the desalination module. It is well-known that concentration polarization over the membrane surfaces influences the performance of the hollow fiber membranes adversely in the desalination process. Better momentum mixing in the hollow fiber bank in the staggered geometry is expected to improve hollow fiber membrane flux performance as well.

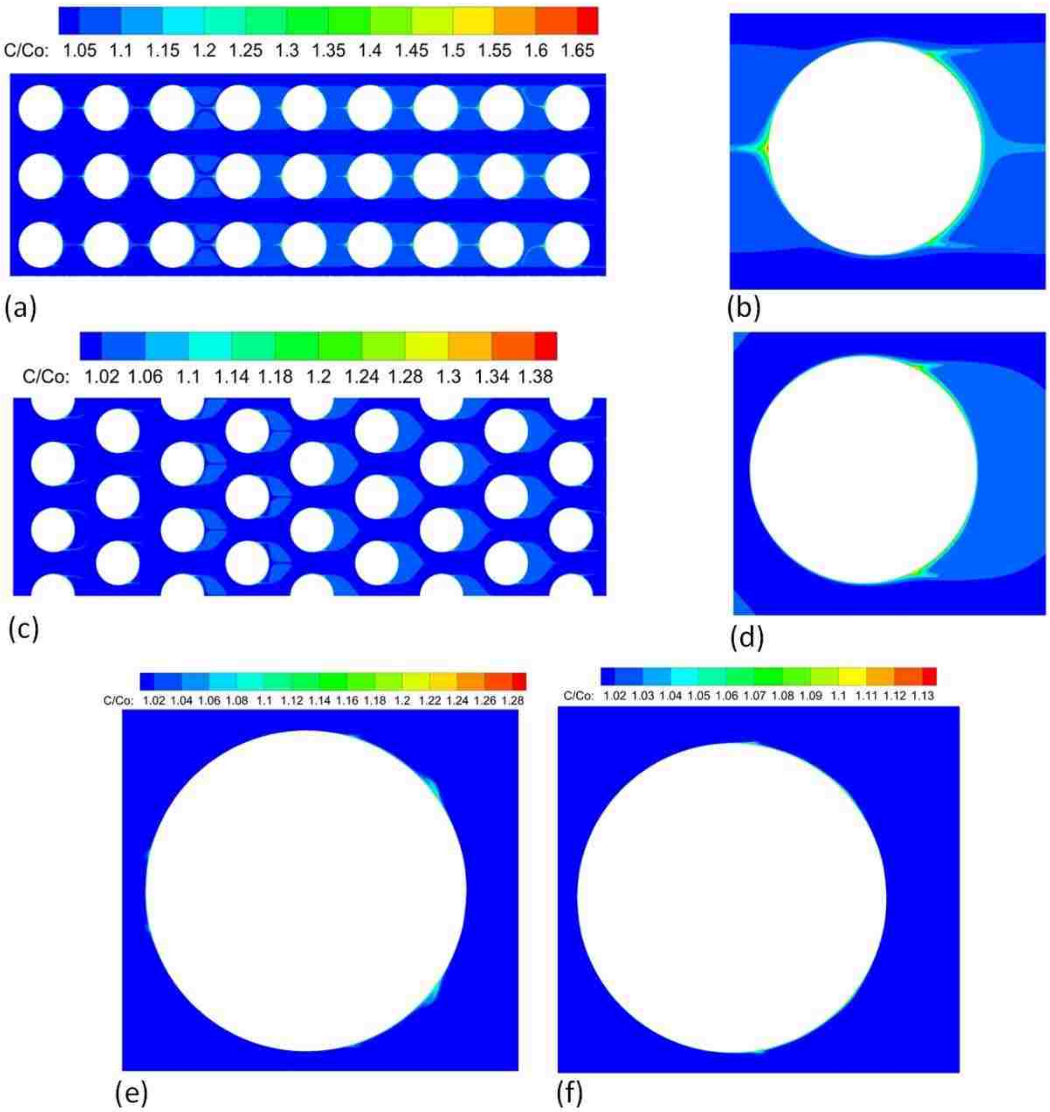

Fig. 30. Contours of the normalized concentration at $Re = 100$ in the inline geometry (a, b) and in the staggered geometry (c, d) with $S/d = 1.5$. Images shown in (e, f) are concentration contours at $Re = 1000$ in the inline and the staggered geometry, respectively. Images shown in (b, d, e and f) are concentration contours around the hollow fiber membrane located at the 6-th column and the middle row.

The normalized permeate water flux along the surface of hollow fiber membranes is calculated for the inline and the staggered geometry and is plotted in Fig. 31 as a function of angle, θ. $\theta = 0$ denotes the forward stagnation point while $\theta = 180$ denotes the backward stagnation point. Fig. 31 shows the profiles of the normalized water flux and normalized concentration along the hollow fiber membrane located at the 8th column and the middle row for $S/d = 1.5$ at $Re = 100$ and 1000. The concentration displayed in Fig. 31 is normalized by the average value of the concentration over the surface of the hollow fiber membrane, $\bar{C}$. In the region near both forward and backward stagnation point the rate of water permeation is higher in the staggered geometry compared to that in the inline geometry at each flow rate. The permeate water flux assumes local minimum where the flow separates and the boundary layer is detached from the membrane surface. Flow separation characteristics differ significantly in these geometries and the locations where boundary layer is detached varies as the feed flow rate is changed. There is a clear transition occurring in the inline geometry as the flow rate is changed. At the low feed flow rate ($Re = 100$) the permeate water flux is the lowest at the forward stagnation point. As the flow rate is increased to $Re = 1000$ the water flux becomes lowest at locations where flow separation occurs, as shown in Fig. 31a and 31b. It should also be noted that the rate of water permeate is increased significantly as the feed flow rate is increased. The concentration profiles show very similar characteristics. At each flow rate the concentration distribution along the surface of the membrane is very different in the inline geometry compared to that in the staggered geometry. It is clear from Fig. 31 that regions where concentration polarization occurs coincide with low flux regions. There is nearly 16% reduction in the concentration polarization as Re is increased from 100 to 1000. It is obvious that the flow characteristics in the hollow fiber membrane bank directly influence the membrane flux performance and the characteristics of the concentration polarization of the separation module. As it is presented above flow field in the hollow fiber bank becomes strongly time dependent and these transient effects are expected to influence the membrane performance. Transient analyses including the mass transport with an accurate membrane flux model should be performed as a future study to investigate hollow fiber membrane performance in these separation modules.

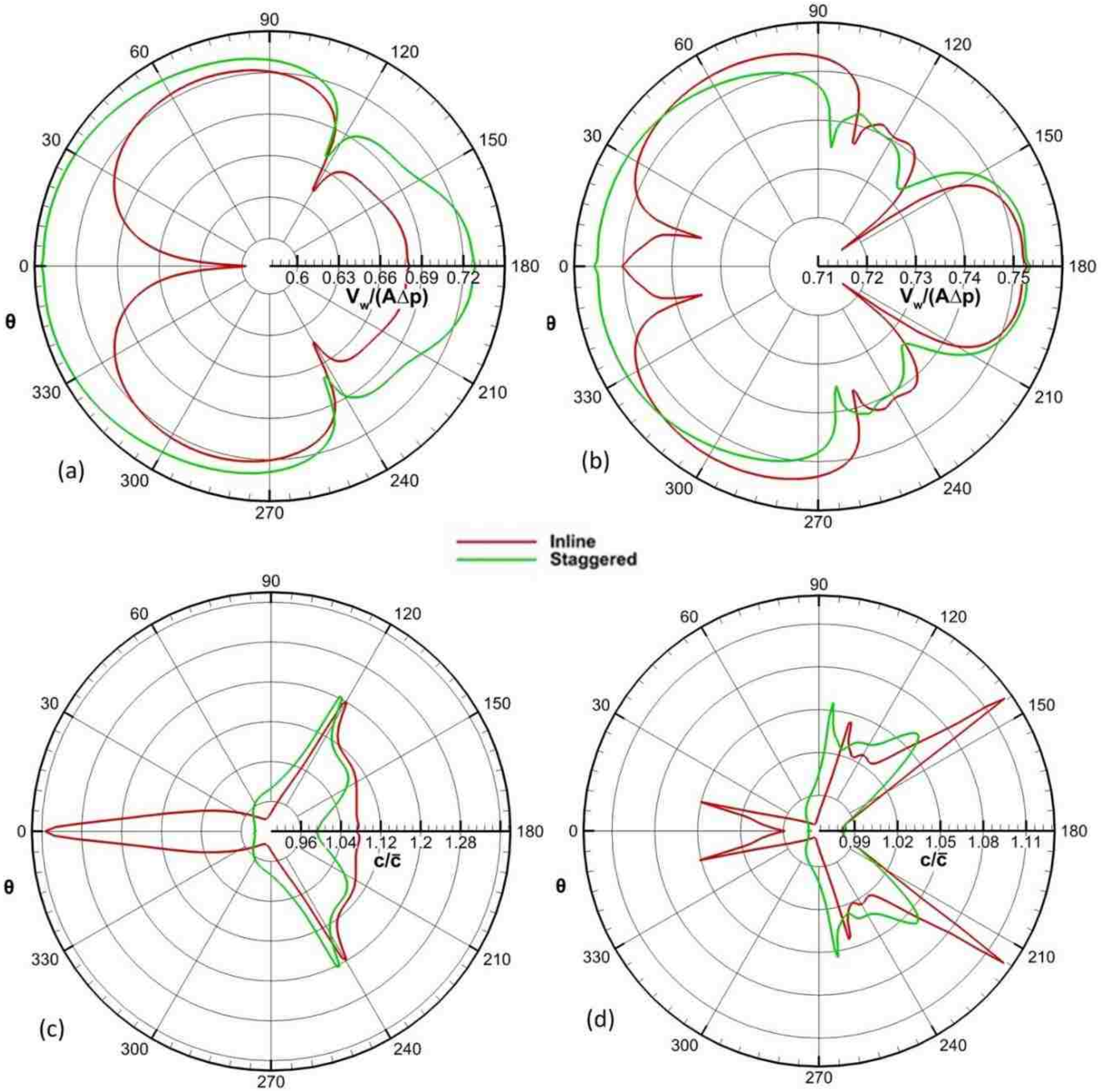

Fig. 31. The normalized water flux profiles along the surface of the membrane in the inline and the staggered geometry at (a) $Re = 100$ and (b) $Re = 1000$. The normalized concentration profiles along the surface of the membrane for the inline and the staggered geometry at (c) $Re = 100$ and (d) $Re = 1000$. Profiles are calculated for the hollow fiber membrane located at the 8th colmun and the middle row.

Fig. 32 and Fig. 33, respectively, illustrate velocity vectors near the hollow fiber membrane located at the 8th column and the middle row at $Re = 100$ and 1000. Flow structures near the forward stagnation region are strikingly different in the inline geometry and in the staggred geometry. High speed flow is observed in the region near the forward stagnation point in the staggered geometry while in the region near the forward stagnation point there is a low recirculating vortex pair in the inline geometry. The intensity of the flow in that region is increased as the feed flow rate is increased and that improves the concentration polarization and increases the permeate water flux. The water flux and concentration polarization are directly tied to flow structures, specifically flow separation patterns, around the hollow fiber membranes.

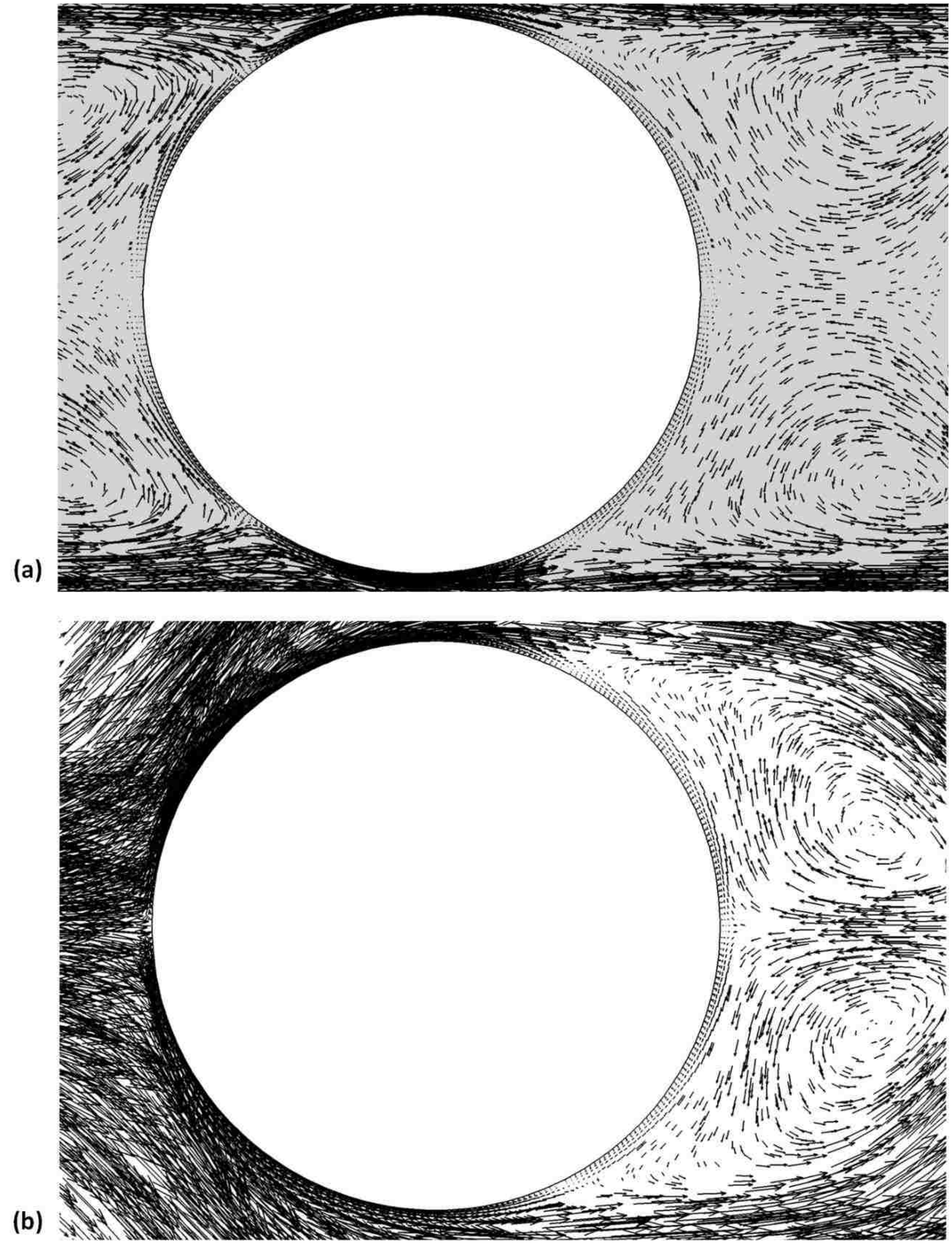

Fig. 32. Velocity vector field near the hollow fiber membrane located at the 8-th column and the middle row at (a, b) $Re = 100$ in the inline geometry (a) and in the staggered geometry (b).

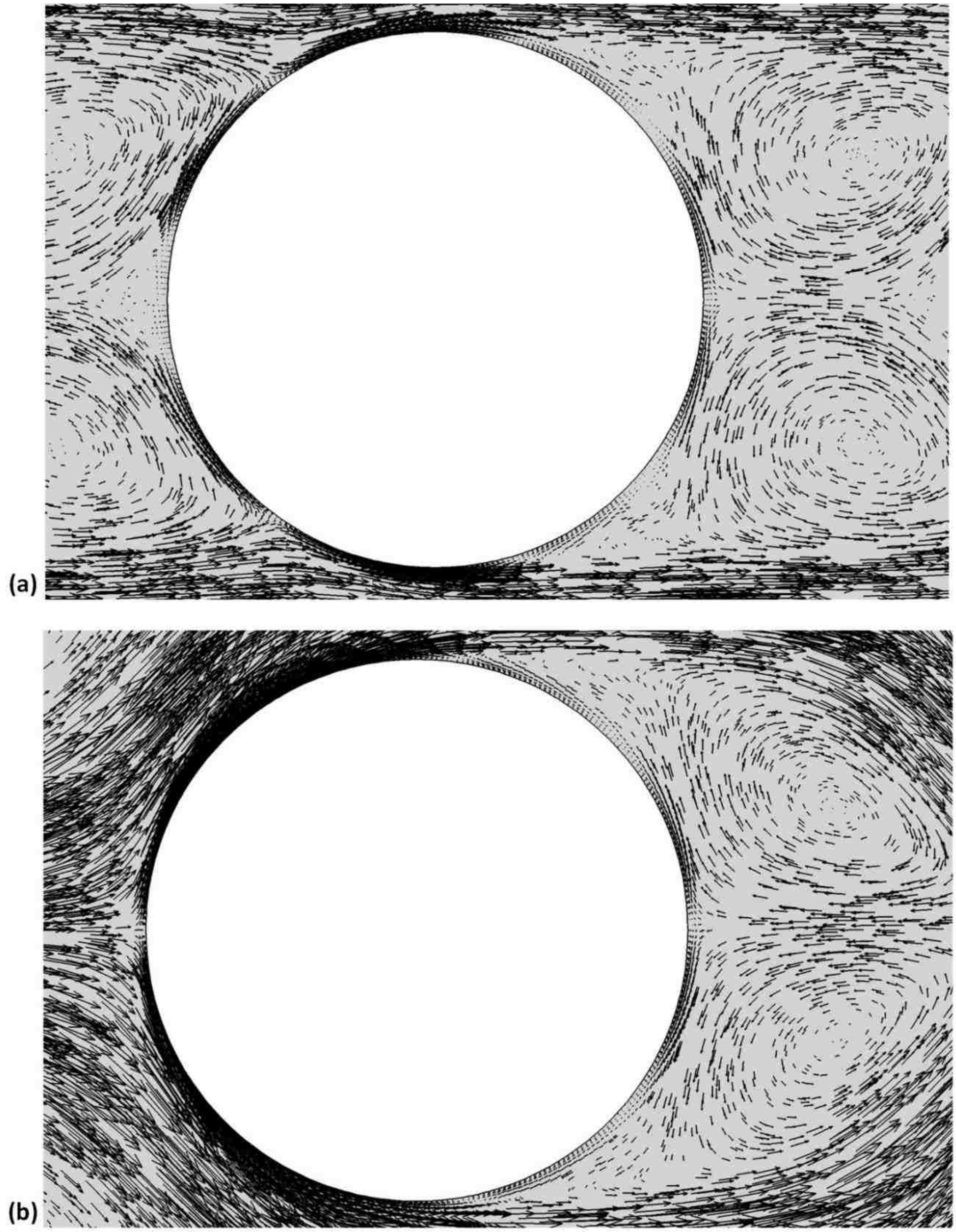

Fig. 33. Velocity vector field near the hollow fiber membrane located at the 8-th column and the middle row at (a, b) $Re = 1000$ in the inline geometry (a) and in the staggered geometry (b).

Local Sherwood number is calculated along the surface of the hollow fiber membranes in the inline and staggered geometry at all feed flow rates considered here. Sherwood number profiles are plotted in Fig. 34 for $S/d = 1.5$ at $Re = 100$ and 1000 as a function of angle (θ) along the surface of hollow fiber membrane located at the 8th column and the middle row. Sherwood number profile in the staggered geometry displays the maximum near the forward stagnation point and the minimum at points where the boundary layer is detached. Overall, Sherwood number is lower in the wake of the hollow fiber membrane in both geometries. Sherwood number increases drastically as the feed flow rate is increased in both geometries. Sherwood number of the staggered geometry is greater than that of the inline geometry at all feed flow rates. The difference in Sherwood number is greater at lower values of the Reynolds number. At $Re = 100$, Sherwood number of the staggered geometry is more than doubled compared to that in the inline geometry, as shown in Fig. 34. Especially, part of the membrane surface near the forward and backward stagnation point in the staggered geometry performs much better than those in the inline geometry. Sherwood number in each geometry is lowest where boundary layer is detached from membrane surface. In the inline geometry surfaces of the hollow fiber membranes subject to high speed flows (jet like flows) perform so much better than surfaces subject to low speed flows (wake flows). On the other hand, front-side surfaces of hollow fiber membranes in the staggered geometry perform better at each feed flow rates. These are the surfaces subject to high speed flows in the staggered geometry. High Sherwood number regions coincide perfectly with low concentration polarization regions at all flow rates in each geometry. Fig. 34 also depicts the normalized wall shear stress as a function of angle (θ). The wall shear stress is normalized by the maximum shear obtained along the surface of the hollow fiber membrane. Low wall shear is observed at or near the forward stagnation and backward stagnation point in both geometries at each flow rate. Overall, at the back side of the hollow fiber the wall shear stress is lower in both geometries. Low shear is also obtained where the boundary layer is detached from the surface of the hollow fiber membrane. These areas are more susceptible to the fouling buildup. Studies by Koutsou et al. [51], Radu et al. [52] and Park et al. [53] show that fouling most likely occurs at low shear regions along the surface of the membrane. It should be mentioned that wall shear is generally higher in regions where high speed flows are observed. This study clearly demonstrates that arrangement of the hollow fiber membranes in the feed channel of desalination modules is vital in design and optimization of these separation modules.

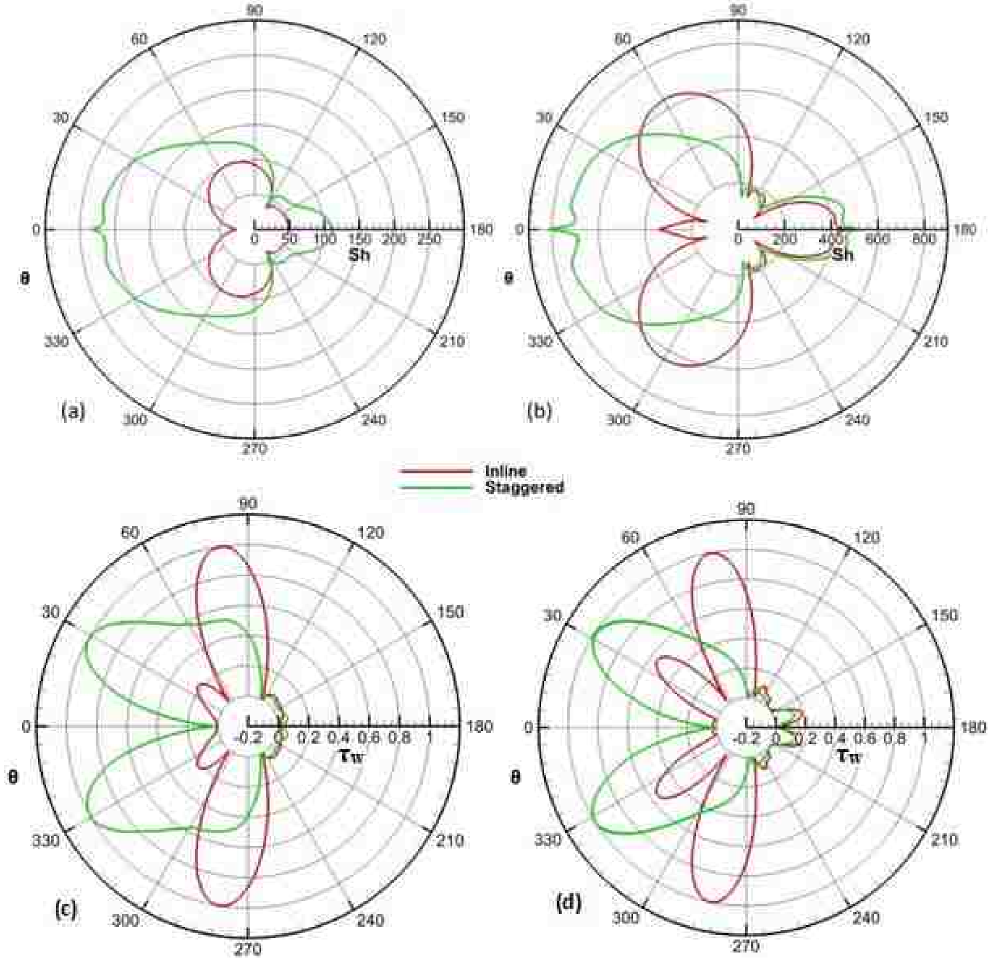

Fig. 34. Sherwood number profiles along the surface of the membrane in the inline and the staggered geometry at (a) $Re = 100$ and (b) $Re = 1000$. The normalized wall shear stress profiles along the surface of the membrane for the inline and the staggered geometry at (c) $Re = 100$ and (d) $Re = 1000$. Profiles are calculated for the hollow fiber membrane located at the 8th colmun and the middle row.

Coefficient of performance (COP) is introduced to compare the hollow fiber membrane flux performance of the separation module with the inline and the staggered geometry. The coefficient of performance is based on the membrane flux performance for the same pumping power and it is defined as $\frac{Sh_s/Sh_i}{(f_s/f_i)^{1/3}}$. Here Sh_s is the average value of the Sherwood number of hollow fiber membranes in the staggered geometry while Sh_i is the average Sherwood number of the inline geometry. f_s is the average friction factor in the staggered geometry and f_i is the friction factor in the inline geometry. Values of the coefficient of performance are listed in Table 11 at various values of Reynolds number in the range of 100 to 1000 for $S/d = 1.5$ and 2. The coefficient of performance is greater than unity at all feed flow rates for both spacing of membranes; indicating that hollow fiber membranes in the staggered geometries perform better than those in the inline geometries. Hollow fiber membrane in the staggered geometry performs even better when the fibers are packed tighter, as indicated by the greater value of COP in Table 11. Performance of the module with the staggered geometry is much better at lower feed flow rates. As the flow rate is increased the coefficient of performance approaches to unity, so both geometry performs similar at higher flow rates. It is also important to note that mitigation of the concentration polarization is better in the staggered geometry at all feed flow rates, especially at higher flow rates. The results presented here agrees well qualitatively with experimental results reported by both Huang et al. and Zhang et al. [28,29] in a similar separation process. The experimental data showed that the flux performance of the module with staggered fibers is better than that of the module with inline fibers. The performance of the staggered modules is much better at lower feed flow rates. It was also reported that staggered module performs much better when hollow fibers are packed tightly.

Re	***COP* (*S/d* = 1.5)**	***CP* (*S/d* = 2)**
100	1.224	1.120
200	1.167	1.118
300	1.139	1.112
500	1.125	1.109
700	1.114	1.007
1000	1.102	1.003

Table 11. The coefficient of performance, COP, is listed as a function of Re for S/d of 1.5 and 2. COP compares performance of hollow fiber membranes in the staggered geometry against hollow fiber membranes in the inline geometry.

5.5. CONCLUSION

Numerical simulations are conducted to characterize flux performance of the membrane, concentration polarization and potential fouling sites for the water desalination process by reverse osmosis hollow fiber membrane using steady k-ω SST turbulence model. Surface of hollow fiber membranes is modeled as a functional boundary where permeate water flux is determined from the local concentration, and the permeability and the selectivity of hollow fiber membranes. Velocity and concentration field are characterized in the bank of hollow fiber membrane in the inline and the staggered geometry. Profiles of the permeate water flux and concentration along the surface of the hollow fiber membranes are presented for a wide range of the Reynolds number. The permeate water flux and Sherwood number increases as the feed flow rate is increased and concentration polarization is alleviated significantly with increasing feed flow rate. Hollow fiber membranes in the staggered geometry performs better than those in the inline geometry, especially at lower flow rates. This conclusion is consistent with the observations made by Huang and Zhang and their co-workers. Large Eddy simulations using lattice Boltzmann method show that flows in the bank of hollow fiber membrane are strongly time dependent. Such transient effects could have profound influence on the membrane flux performance, concentration polarization and fouling. It is worth investigating transient effects in the future studies. Time averaged flow properties predicted by transient LES-LBM simulations agree reasonably well with those predicted by steady SST turbulence model; validating the turbulence model and the numerical methods used to characterize performance of the separation module. It is demonstrated by the present study that the arrangement and the spacing of hollow fiber membranes in the desalination module are essential in the design and optimization of these systems.

CHAPTER 6: SUMMARY

6.1. SUMMARY OF CURRENT RESULTS

The gas separation using reverse osmosis membranes had been studied extensively by several investigators. Enhancing the performace of separation modules and enhancing the selectivity and the permeability of the hollow fiber and spiral wound membrane modules are some of these studies. In present work, the focus is more on improving the membrane performance utilizing momentum mixing and less on these aspects of separation. This is a well-known and well-studied alternative method for enhancing membrane performance.

Computational study is conducted to investigate the flow and mass transport process utilizing hollow fiber (HFM) membrane and spiral wound modules in gas separation and desalination applications. The studies consist of two- and three-dimensional flow computational fluid dynamics (CFD) simulations. The membrane surface is treated as a functional boundary where the mass flux and concentration of each species are coupled. Simulations are conducted using the steady Shear Stress Transport (k-ω SST) turbulence model in order to characterize hollow fiber membrane and spiral wound membrane performance. The separation module is arranged in the radial crossflow configuration, where the flow direction is normal to the HFM axes. In this study, we examined different hollow fiber membrane arrangements within the module at different values of Reynolds numbers.

Hollow fiber membrane modules are among the most common separation devices employed in membrane separation applications. Three-dimensional steady-state computational fluid dynamics simulations are carried out to study flow past hollow fiber membrane banks. The current study investigates the effects of flow behavior on membrane performance during binary mixture separations. Carbon dioxide (CO_2) removal from methane (CH_4) is examined for various arrangements of HFMs in staggered and inline configurations. The most common HFM module arrangement is the axial flow configuration, however, this work focuses on the radial crossflow configuration. The hollow fiber membrane surface is a functional boundary where the suction rate and concentration of each species are coupled, and are functions of the local partial pressures, the permeability, and the selectivity of the HFM. CFD simulations employed the turbulent k-ω Shear Stress Transport (k-ω SST) model to study HFM performance for Reynolds numbers, $200 \leq Re \leq 1000$. The efficiency of the inline and staggered arrangements in the separation module is evaluated by the coefficient of performance and the rate of mass flow per unit area of CO_2 passing across the membrane surface. As a result of numerical simulations, increased momentum mixing achieved with the staggered arrangement enhances HFM performance, and is observed through comparison of the x- and y-directions of vorticity that illustrate considerable differences in vortical structure size. This work demonstrates that the module with staggered arrangements outperforms the module with inline arrangements.

The influence of hollow fiber membrane arrangement on fluid dynamics and mass transfer in feed channels bounded by two parallel spiral wound membranes have been studied. This study is the first in implementing membrane flux boundary conditions in hybrid membrane geometry to study reverse osmosis process of gas separation. The results show that three-dimensional flows generated by the net type of hollow fiber membranes have profound effects on the membrane performance. The net type of hollow fiber membrane with angle $\theta=45°$ induces higher velocity, vorticity, Q-criterion, and mole fraction concentration at the membrane surface when compared to the inline, and staggered arrangements. The momentum mixing generated by the net type of hollow fiber membrane enhances the mass transfer rates. These hybrid membrane systems have higher performance and found to be more effective when compared to the conventional hollow fiber or spiral wound modules.

Reverse osmosis (RO) desalination is a common process to produce fresh water. The process requires high pressure in a feed channel of the separation module. The applied pressure has to be larger than the osmotic pressure of the dissolved salt. The selective hollow fiber membrane passes water and rejects dissolved salt. The rejected salt can accumulate near the surface of the membrane and can result in a concentration polarization. It is well-known that the salt concentration polarization at the RO membrane surface adversely affects the pure water production. It has been documented that the concentration polarization reduction at the membrane surface increases membrane life time [54,55]. It is reported that the concentration polarization and the fouling buildup can be mitigated by the promotion of the momentum mixing in the feed channel in desalination modules [10,12,50]. For design and optimization of these separation modules the membrane flux performance, concentration polarization and fouling-buildup/scaling need to be characterized. There are many studies documented that the momentum mixing in the feed channel help improves the membrane flux performance in both gas separation and desalination modules [10,12,14,15,19,20,50].

Water desalination by reverse osmosis hollow fiber membrane has been widely used to produce fresh water. This work numerically characterizes flux performance of the membrane, concentration polarization and potential fouling sites in the reverse osmosis desalination module containing hollow fiber membranes arranged in an inline and a staggered configuration. Steady k-ω SST turbulence model is utilized to study membrane performance. An accurate membrane flux model, the solution-diffusion model, is employed. Hollow fiber membrane surface is treated as a functional boundary where the rate of water permeation is coupled with local concentration along the membrane surface. The rate of water permeation increases and concentration polarization decreases as the feed flow rate is increased. Hollow fiber membranes in the staggered geometry perform better than those in the inline geometry. It is proven by the present study that desalination modules containing hollow fiber membranes should be designed and optimized by careful consideration of their configurations. It is demonstrated here that flows in the hollow fiber bank become strongly time-dependent at high flow rates and that transient effects could profoundly influence hollow fiber membrane flux performance and characterization of concentration polarization.

6.2. FUTURE WORK

- High fidelity Large Eddy Simulations (LES) should be conducted to study gas separation process in modules considered in this study. These simulations can identify flow structures in the feed channel more accurately. More importantly, transient effects on the membrane performance can be captured with LES simulations. Large eddy simulations conducted by our group for desalination process revealed that transient nature of flows have profound influence on membrane performance. It is worth investigating transient effects in the future studies for gas separation using reverse osmosis membranes. Also, LES technique is more accurate model that can capture three-dimensional flow structures better than k-ω SST turbulence model employed in the current study.

- The current work assumes constant total concentration of the mixture in the feed channel. Hence, in this work the mass transport equation is solved only for one of the speices. With an assumption of constant total concentration the distribution of other species concentration is determined. This assumption should be relaxed for future studies. Since both species can diffuse through the membrane with a different rate the total concentration varies inside the feed channel and this variation could be significant enough that it should not be neglected. Mass transport model should be improved by considering varations of each species for the future work. A better understanding of the influence of varying concentration and pressure could allow us to further enhancment of the membrane module and to better understanding of the membrane performance.
- The current study can be extended by conducting an experimental investigation because there is a lack of experimental investigation studying the influence of momentum mixing on the membrane performance. Experimental measurements with computational predictions can work very well to optimize and design the next generation of gas separation modules.
- It is anticipated that this work would be the basis for further studies and enhancement of the hollow fiber membrane module in desalination and gas separation applications.

REFERENCES

[1] B. Wetenhall, J.M. Race, M.J. Downie, The effect of CO_2 purity on the development of pipeline networks for carbon capture and storage schemes, Int. J. Greenh. Gas Control. 30 (2014) 197–211. doi:10.1016/j.ijggc.2014.09.016.

[2] M.J. Thundyil, W.J. Koros, Mathematical modeling of gas separation permeators - for radial crossflow , countercurrent , and cocurrent hollow fiber membrane modules, J. Memb. Sci. 125 (1997) 275–291.

[3] A. Saeed, R. Vuthaluru, H.B. Vuthaluru, Investigations into the effects of mass transport and flow dynamics of spacer filled membrane modules using CFD, Chem. Eng. Res. Des. 93 (2014) 79–99. doi:10.1016/j.cherd.2014.07.002.

[4] S. Mojab, A. Pollard , J. Pharoah , S. Beale, Unsteady laminar to turbulent flow in a spacer-filled channel, Flow Turbulence Combust (2014) 563–577. doi:10.1007/s10494-013-9514-4.

[5] S.K. Karode, A. Kumar, Flow visualization through spacer filled channels by computational fluid dynamics I. Pressure drop and shear rate calculations for flat sheet geometry, J. Memb. Sci. 193 (2001) 69–84.

[6] C.P. Koutsou, A.J. Karabelas, A novel retentate spacer geometry for improved spiral wound membrane (SWM) module performance, J. Membr. Sci. 488 (2015) 129–142. doi:10.1016/j.memsci.2015.03.064.

[7] M. Shakaib, S. Hasani, M. Mahmood, Study on the effects of spacer geometry in membrane feed channels using three-dimensional computational flow modeling, J. Memb. Sci. 297 (2007) 74–89. doi:10.1016/j.memsci.2007.03.010.

[8] A. Subramani, S. Kim, E.M. V Hoek, Pressure , flow , and concentration profiles in open and spacer-filled membrane channels, J. Memb. Sci. 277 (2006) 7–17. doi:10.1016/j.memsci.2005.10.021.

[9] R. Kaya, G. Deveci, T. Turken, R. Sengur, S. Guclu, Analysis of wall shear stress on the outside-in type hollow fi ber membrane modules by CFD simulation, Desalination 351 (2014) 109–119. doi:10.1016/j.desal.2014.07.033.

[10] A.E. Anqi, N. Alkhamis, A. Oztekin, Numerical simulation of brackish water desalination by a reverse osmosis membrane, Desalination 369 (2015) 156–164. doi:10.1016/j.desal.2015.05.007.

[11] A.E. Anqi, N. Alkhamis, A. Oztekin, Steady three dimensional flow and mass transfer analyses for brackish water desalination by reverse osmosis membranes, Int. J. Heat Mass Transf. 101 (2016) 399–411. doi:10.1016/j.ijheatmasstransfer.2016.05.102.

[12] A.E. Anqi, N. Alkhamis, A. Oztekin, Computational study of desalination by reverse osmosis — Three-dimensional analyses, Desalination 388 (2016) 38–49. doi:10.1016/j.desal.2016.03.017.

[13] M. Usta, A.E. Anqi, A. Oztekin, Reverse osmosis desalination modules containing corrugated membranes - Computational study, Desalination 416 (2017) 129–139. doi:10.1016/j.desal.2017.05.005.

[14] N. Alkhamis, D.E. Oztekin, A.E. Anqi, A. Alsaiari, A. Oztekin, Numerical study of gas separation using a membrane, Int. J. Heat Mass Transf. 80 (2015) 835–843. doi:10.1016/j.ijheatmasstransfer.2014.09.072.

[15] M. Alrehili, M. Usta, N. Alkhamis, A.E. Anqi, A. Oztekin, Gas separation by using spiral wound membrane, ASME-IMECE2015. (2015).

[16] M. Shakaib, S. Hasani, M. Mahmood, CFD modeling for flow and mass transfer in spacer-obstructed membrane feed channels, J. Membr. Sci. 326 (2009) 270–284. doi:10.1016/j.memsci.2008.09.052.

[17] V. Geraldes, V. Semiao, M. Norberta de Pinho, Concentration polarisation and flow structure within nanofiltration spiral-wound modules with ladder-type spacers, Comput. Struct. 82 (2004) 1561–1568. doi:10.1016/j.compstruc.2004.03.052.

[18] S. Ma, L. Song, Numerical study on permeate flux enhancement by spacers in a crossflow reverse osmosis channel, J. Membr. Sci. 284 (2006) 102–109. doi:10.1016/j.memsci.2006.07.022.

[19] M. Alrehili, M. Usta, N. Alkhamis, A.E. Anqi, A. Oztekin, Flows past arrays of hollow fiber membranes – Gas separation, Int. J. Heat Mass Transf. 97 (2016) 400–411. doi:10.1016/j.ijheatmasstransfer.2016.02.022.

[20] N. Alkhamis, A.E. Anqi, A. Oztekin, Computational study of gas separation using a hollow fiber membrane, Int. J. Heat Mass Transf. 89 (2015) 749–759. doi:10.1016/j.ijheatmasstransfer.2015.05.090.

[21] M.G. Marcovecchio, N.J. Scenna, P.A. Aguirre, Improvements of a hollow fiber reverse osmosis desalination model: Analysis of numerical results, Chem. Eng. Res. Des. 88 (2010) 789–802. doi:10.1016/j.cherd.2009.12.003.

[22] R. Ghidossi, J.V. Daurelle, D. Veyret, P. Moulin, Simplified CFD approach of a hollow fiber ultrafiltration system, Chem. Eng. J. 123 (2006) 117–125. doi:10.1016/j.cej.2006.07.007.

[23] P. Sukitpaneenit, T.-S. Chung, High performance thin-film composite forward osmosis hollow fiber membranes with macrovoid-free and highly porous structure for sustainable water production, Environ. Sci. Technol. 46 (2012) 7358–7365. doi:10.1021/es301559z.

[24] S. Chou, R. Wang, L. Shi, Q. She, C. Tang, A.G. Fane, Thin-film composite hollow fiber membranes for pressure retarded osmosis (PRO) process with high power density, J. Membr. Sci. 389 (2012) 25–33. doi:10.1016/j.memsci.2011.10.002.

[25] S.-M. Huang, M. Yang, Y. Yang, X. Yang, Fluid flow and heat transfer across an elliptical hollow fiber membrane tube bank for air humidification, Int. J. Therm. Sci. 73 (2013) 28–37. doi:10.1016/j.ijthermalsci.2013.05.013.

[26] S.-M. Huang, M. Yang, Heat and mass transfer enhancement in a cross-flow elliptical hollow fiber membrane contactor used for liquid desiccant air dehumidification, J. Membr. Sci. 449 (2014) 184–192. doi:10.1016/j.memsci.2013.08.033.

[27] R. Jiang, M. Yang, S. Chen, S.-M. Huang, X. Yang, Fluid flow and heat transfer across an elliptical hollow fiber membrane tube bank with randomly distributed features, Int. J. Heat Mass Transf. 76 (2014) 559–567. doi:10.1016/j.ijheatmasstransfer.2014.05.004.

[28] S.-M. Huang, M. Yang, W.F. Zhong, Y. Xu, Conjugate transport phenomena in a counter flow hollow fiber membrane tube bank: Effects of the fiber-to-fiber interactions, J. Membr. Sci. 442 (2013) 8–17. doi:10.1016/j.memsci.2013.04.024.

[29] L.-Z. Zhang, S.-M. Huang, W.-B. Zhang, Turbulent heat and mass transfer across a hollow fiber membrane bundle considering interactions between neighboring fibers, Int. J. Heat Mass Transf. 64 (2013) 162–172. doi:10.1016/j.ijheatmasstransfer.2013.04.035.

[30] M.M. Teoh, S. Bonyadi, T.S. Chung, Investigation of different hollow fiber module designs for flux enhancement in the membrane distillation process, J. Membr. Sci. 311 (2008) 371–379. doi:10.1016/j.memsci.2007.12.054.

[31] N. Alkhamis, D.E. Oztekin, A. Anqi, A. Alsaiari, A. Oztekin, Gas separation using a membrane, ASME 2013 Int. Mech. Eng. Congr. Expo. Am. Soc. Mech. Eng. (2013) V07AT08A039-V007AT008A039.

[32] T. Katoh, M. Tokumura, H. Yoshikawa, Y. Kawase, Dynamic simulation of multicomponent gas separation by hollow-fiber membrane module : Nonideal mixing flows in permeate and residue sides using the tanks-in-series model, Sep. Purif. Technol. 76 (2011) 362–372. doi:10.1016/j.seppur.2010.11.006.

[33] A.E. Anqi, M. Alrehili, M. Usta, A. Oztekin, Numerical analysis of hollow fi ber membranes for desalination, Desalination 398 (2016) 39–51. doi:10.1016/j.desal.2016.07.019.

[34] A. Mourgues, J. Sanchez, Theoretical analysis of concentration polarization in membrane modules for gas separation with feed inside the hollow-fibers, J. Memb. Sci. 252 (2005) 133–144. doi:10.1016/j.memsci.2004.11.024.

[35] R. Behling, K. Ohlrogge, O. Lu, Concentration polarization in gas permeation, J. Memb. Sci. 146 (1998).

[36] F.R. Menter, Two-equation eddy-viscosity turbulence models for engineering applications, Am. Inst. Aeronaut. Astronaut. J. 32 (1994) 1598–1605. doi:10.2514/3.12149.

[37] W. Changcharoen, S. Eiamsa-ard, Numerical investigation of turbulent heat transfer in channels with detached rib-arrays, Heat Transf.-Asian Res. 40 (2011) 431–447. doi:10.1002/htj.20357.

[38] A. Chaube, P.K. Sahoo, S.C. Solanki, Analysis of heat transfer augmentation and flow characteristics due to rib roughness over absorber plate of a solar air heater, Renewable Energy 31 (2006) 317–331. doi:10.1016/j.renene.2005.01.012.

[39] L. Malaeb, G.M. Ayoub, Reverse osmosis technology for water treatment: State of the art review, Desalination 267 (2011) 1–8. doi:10.1016/j.desal.2010.09.001.

[40] J. Wang, D.S. Dlamini, A.K. Mishra, M.T.M. Pendergast, M.C.Y. Wong, B.B. Mamba, V. Freger, A.R.D. Verliefde, E.M.V. Hoek, A critical review of transport through osmotic membranes, J. Membr. Sci. 454 (2014) 516–537. doi:10.1016/j.memsci.2013.12.034.

[41] J. Geens, K. Boussu, C. Vandecasteele, B. Van der Bruggen, Modelling of solute transport in non-aqueous nanofiltration, J. Membr. Sci. 281 (2006) 139–148. doi:10.1016/j.memsci.2006.03.028.

[42] O. Kedem, A. Katchalsky, Thermodynamic analysis of the permeability of biological membranes to non-electrolytes, Biochim. Biophys. Acta. 27 (1958) 229–246. doi:10.1016/0006-3002(58)90330-5.

[43] M. Kargol, A. Kargol, Investigation of reverse osmosis on the basis of the Kedem–Katchalsky equations and mechanistic transport equations, Desalination 190 (2006) 267–276. doi:10.1016/j.desal.2005.09.007.

[44] P. Sukitpaneenit, T.-S. Chung, L.Y. Jiang, Modified pore-flow model for pervaporation mass transport in PVDF hollow fiber membranes for ethanol–water separation, J. Membr. Sci. 362 (2010) 393–406. doi:10.1016/j.memsci.2010.06.062.

[45] A. Yaroshchuk, E. Staude, Charged membranes for low pressure reverse osmosis properties and applications, Desalination 86 (1992) 115–133. doi:10.1016/0011-9164(92)80029-9.

[46] A.R. Hassan, N. Ali, N. Abdull, A.F. Ismail, A theoretical approach on membrane characterization: the deduction of fine structural details of asymmetric nanofiltration membranes, Desalination 206 (2007) 107–126. doi:10.1016/j.desal.2006.06.008.

[47] J.G. Wijmans, R.W. Baker, The solution-diffusion model: a review, J. Membr. Sci. 107 (1995) 1–21. doi:10.1016/0376-7388(95)00102-I.

[48] Y. H. Qian and D. D’Humières and P. Lallemand, Lattice BGK Models for Navier-Stokes Equation, EPL (Europhysics Lett. 17 (1992) 479.

[49] S. Chen, G.D. Doolen, Lattice Boltzmann Method for Fluid Flows, Annu. Rev. Fluid Mech. 30 (1998) 329–364. doi:10.1146/annurev.fluid.30.1.329.

[50] A.E. Anqi, N. Alkhamis, M. Alrehili, A. Oztekin, Numerical study of brackish water desalination using reverse osmosis, Proc. IDA World Congr. Desalination Water Reuse San Diego 2015. (2015). doi:10.13140/RG.2.1.4452.6565.

[51] C.P. Koutsou, S.G. Yiantsios, A.J. Karabelas, Membrane module performance optimization using CFD simulation of flow through narrow channels with spacers, in: Proc. IDA World Congr. Desalination Water Reuse, 2007: pp. 21–26.

[52] A.I. Radu, M.S.H. van Steen, J.S. Vrouwenvelder, M.C.M. van Loosdrecht, C. Picioreanu, Spacer geometry and particle deposition in spiral wound membrane feed channels, Water Res. 64 (2014) 160–176. doi:http://dx.doi.org/10.1016/j.watres.2014.06.040.

[53] H.-G. Park, S.-G. Cho, K.-J. Kim, Y.-N. Kwon, Effect of feed spacer thickness on the fouling behavior in reverse osmosis process — A pilot scale study, Desalination 379 (2016) 155–163. doi:10.1016/j.desal.2015.11.011.

[54] S.S. Sablani, M.F.A. Goosen, R. Al-Belushi, M. Wilf, Concentration polarization in ultrafiltration and reverse osmosis: a critical review, Desalination 141 (2001) 269–289. doi:10.1016/S0011-9164(01)85005-0.

[55] C. Fritzmann, J. Löwenberg, T. Wintgens, T. Melin, State-of-the-art of reverse osmosis desalination, Desalination 216 (2007) 1–76. doi:10.1016/j.desal.2006.12.009.

VITA

Mohammed Alrehili was born on Dec. 9th ,1984. In Medina, Saudi Arabia. In 2003, Mohammed decided to study mechanical engineering at King Abdulaziz University. He graduated with a Bachelor of Science Degree in Mechanical Engineering in 2007 and right after joined The Saudi Basic Industries Corporation (SABIC) company, Hadeed Branch. He worked there as a fire system engineer for a period of three and half years. In 2011, Mohammed joined the mechanical engineering department at Tabuk University where he worked as a teaching assistant. As a part of his work contract, he has a full scholarship to pursue a graduate level degree. He joined the mechanical engineering department graduate program at Lehigh University in the summer of 2013. He was received his Master of Science Degree in August 2015. Mohammed will award the degree of Doctor of Philosophy in mechanical engineering from Lehigh University in 2017. He is author and co-author of many journal articles and conference papers.